Post Transition Metals Doped Bismuth Oxyhalides for Photocatalysts Applications using Computational and Experimental Approaches

Tadesse Lemma Wakjira

A Dissertation Submitted to the Department of Applied Physics
College of Applied Natural Sciences

Presented in a Partial Fulfillment of the Requirements for the Degree of Doctor of Philosophy in Applied Physics (Specialization in Material Physics)

Office of Graduate Studies
Adama Science and Technology University

December 31, 2024
Adama, Ethiopia

Post Transition Metals Doped Bismuth Oxyhalides for Photocatalysts Applications using Computational and Experimental Approaches

PhD Candidate:
Tadesse Lemma Wakjira

Supervisor: Prof. Abebe Belay (PhD)
Co-supervisor: Gashaw Beyene (PhD)
Co-supervisor: Kumneger Tadele (PhD)

A Dissertation Submitted to the Department of Applied Physics Program
College of Applied Natural Sciences

Presented in a Partial Fulfillment of the Requirements for the Degree of
Doctor of Philosophy in Applied Physics (Specialization in Material Physics

Office of Graduate Studies
Adama Science and Technology University

December 31, 2024
Adama, Ethiopia

Declaration

I declare that this dissertation entitled "**Post Transition Metals Doped Bismuth Oxyhalides for Photocatalysts Applications using Computational and Experimental Approaches**" is my own work and has not been submitted to any university for a similar purpose. The references used in this dissertation are duly recognized by proper citations.

Name of candidate	Signature	Date

Recommendation of Supervisors

I, the major advisor/supervisor of this dissertation, hereby certify that I have closely advised/supervised the student while developing this dissertation and read the final dissertation entitled "**Post Transition Metals Doped Bismuth Oxyhalides for Photocatalysts Applications using Computational and Experimental Approaches**" prepared under my guidance by **Tadesse Lemma Wakjira**. Therefore, I recommend the submission of the dissertation to the department for further approval.

Name of Major Supervisor:	Signature	Date
Name of Co-supervisor	Signature	Date
Name of Co-supervisor	Signature	Date

Approval Page

I/we hereby certify that the recommendation and suggestion given by the dissertation review committee are appropriately incorporated into the final dissertation entitled "**Post Transition Metals Doped Bismuth Oxyhalides for Photocatalysts Applications using Computational and Experimental Approaches**" prepared under my/our guidance by **Tadesse Lemma Wakjira** submitted in the partial fulfillment of the requirements of the degree of Doctor of Philosophy in **Applied Physics (Specialization in Material Physics)**.

Name of Major Supervisor:	Signature	Date
Name of Co-supervisor	Signature	Date
Name of Co-supervisor	Signature	Date

Approval of Board of Examiners

We, the undersigned, members of the Board of Examiners of the dissertation open defense by **Tadesse Lemma Wakjira** have read and evaluated the dissertation entitled "Post Transition Metals Doped Bismuth Oxyhalides for Photocatalysts Applications using Computational and Experimental Approaches" and examined the candidate during open defense. This is therefore to certify that the dissertation is accepted for the partial fulfillment of the requirement of the degree of Doctor of Philosophy in **Applied Physics (Specialization in Material Physics)**.

Chairperson	Signature	Date
Internal Examiner 1	Signature	Date
Internal Examiner 2	Signature	Date
External Examiner 1	Signature	Date
External Examiner 2	Signature	Date

Final approval and acceptance of the dissertation is contingent upon submission of its final copy to the Office of Postgraduate Studies (OPGS) through the Department Graduate Council (DGC) and College Graduate Committee (CGC).

Department Head	Signature	Date
College Dean	Signature	Date
Office of Postgraduate Studies, Dean	Signature	Date

DEDICATIONS

This dissertation is dedicated to the cherished memory of my father Lemma Wakjira and my sister Askela Lemma, who, unfortunately, passed away before they could witness the culmination of my academic journey and the realization of my doctoral aspirations. Their unwavering love, support, and sacrifices throughout my life have been the foundation upon which I have built my education and personal development.

My father, Lemma Wakjira, embodied the true essence of dedication and perseverance. His commitment to his family's welfare and his belief in the value of education instilled in me a strong work ethic and a drive to pursue my goals relentlessly. He often shared stories of the challenges he faced and how he overcame them, teaching me the importance of resilience in the pursuit of knowledge and success.

Similarly, my sister, Askela Lemma, was a source of inspiration and strength. She nurtured my curiosity and encouraged me to explore my interests. Her kindness and wisdom guided me through life's hurdles and motivated me to dream big. Her faith in my abilities helped shape my identity as a student and a researcher.

Although they are no longer with me physically, their legacy and values continue to inspire my work and character. This dissertation stands as a testament to their influence in my life and my unwavering commitment to honor their memory through hard work and dedication to my field of study. I am profoundly grateful for the love and support they provided, which has been instrumental in my academic achievements.

BIOGRAPHICAL SKETCH

The candidate was born from his family **Sisay Senbeta and Lemma Wakjira** in May 1989 in Bale Gasgar Woreda, located in the East Arsi Zone, approximately 170 km from Adama, Ethiopia. His educational journey commenced at **Aymiro Dindin Primary School**, where he completed his primary education from 1997 to 2002. He pursued his secondary education at **Aymiro Bale Secondary School** from 2003 to 2006 and subsequently attended **Amign Gasgar Secondary and Preparatory School** from 2007 to 2008, where he laid the groundwork for his future academic endeavors.

Upon completing his preparatory education, he joined Haramaya University in 2009. His dedication and hard work culminated in earning a **Bachelor of Science** (BSc) degree in Applied Physics in 2012. After graduation, he was employed as a graduate assistant at **Haramaya University,** where he began his academic career. Following two years of service in this role, the researcher furthered his education by enrolling in the postgraduate program in 2014/15 to pursue a **Master of Science (MSc)** degree in Physics. Upon the successful completion of his MSc studies, he served as Head of the Physics Department at Haramaya University, for three and a half years. This position allowed him to contribute to the academic community and gain valuable leadership experience.

In 2021/22, he joined **Adama Science and Technology University** to pursue his PhD studies. Over the last three years, he dedicated himself to rigorous research, honing his expertise in his field. Now, he is prepared to present his PhD dissertation work, marking a significant milestone in his academic journey and his commitment to advancing knowledge in the discipline of physics.

ACKNOWLEDGMENTS

First and foremost, I extend my deepest thanks to the **Almighty God** for granting me health and strength during this demanding period of my life. Your blessings have been a source of motivation and resilience.

Next, I wish to convey my sincere appreciation to my supervisor, **Prof. Abebe Belay.** His invaluable guidance, unwavering support, and insightful feedback have been instrumental in shaping my research direction and enhancing the quality of my work. Prof. Abebe's expertise and encouragement fostered an environment in which I could grow both personally and academically. I am also profoundly grateful to my co-supervisors, D**r. Gashaw Beyene,** and **Dr. Kumneger Tadele.** Their encouragement and profound expertise significantly contributed to my research and provided me with critical perspectives that enriched my understanding of the subject matter. My thanks also go to **Dr. Ephriem Tadesse** staff of Haramaya University Department of Chemistry for his computational guidance.

I would like to acknowledge all **PhD candidates** in Applied Physics at Adama Science and Technology University for their collaborative spirit throughout this journey. The support and interactions with them made this experience not only more enjoyable but also intellectually enriching. Their friendship and input have greatly added to my academic and personal growth. Furthermore, my thanks also go to Mr. Leulseged Bekele and Mr. Guta, for their support during laboratory work.

My special thanks go to my mother, brothers, and sisters for their unwavering love and encouragement. My heartfelt appreciation also goes to my wife (**Geze Jote**) and children (**Kenbon, Hawinet, and Nafilet**), your patience and understanding have provided me with immense strength during the challenging moments of this process. Your sacrifices and belief in my abilities have been invaluable.

Lastly, I would like to extend my gratitude to **Adama Science and Technology University** and **Haramaya University** for their support, resources, and facilities in my academic pursuits. Additionally, I appreciate the Ministry of Education particularly (Mrs. **Lensa Abera**) for her support by providing HPC account for Computational work. Thank you all for being part of this remarkable journey.

Contents

List of Figures

List of Tables

Acronyms and Abbreviations

BBSs	Bismuth Based Semiconductors
BiOX	Bismuth Oxyhalides
COSMO	Conductor like screening Model
DFT	Density Functional Theory
DMol3	Density Functional Theory Molecular 3
DOS (PDOS, TDOS)	Density of State (Partial (Total) density of State)
FTIR	Fourier Transform Infrared
GGA	General Gradient Approximation
HOMO	Highest Occupied Molecular Orbital
JDOS	Joint Density of the state
LA(LO)	Longitudinal acoustic (Optical)
LDA	Local Density Approximation
LUMO	Lowest Unoccupied Molecular Orbital
MB	Methylene Blue
MCDS	Monte Carlo Dynamics Simulations
MO	Methyl Orange
MR	Methyl Red
NAO	Natural Atomic Orbital
NBO	Natural Bonding Orbital
NSCF	Non- Self Consistent Field
PBE	Perdew-Burke-Ernzerhof
PL	Photoluminescence
PW91	Perdew and Wang's 1991
SEM (TEM)	Scanning (Transmission) Electron Microscopy
TA (TO)	Transverse Acoustic (Transverse Optical)
UV-Vis	Ultraviolet-Visible
XRD	X-ray diffraction

Abstract

Bismuth oxyhalides (BiOX) are layered materials with unique physicochemical and optical properties. This study investigates the characteristics of BiOX (X= F, Cl, Br, I) crystals using first-principles calculations. The effect of post transition metals (In, Sn, Tl) doping and co-doping with Br atom on the electronic and optical properties of BiOCl was analyzed using the density functional theory (DFT) method. The molecular interaction of different dyes with water and adsorption behaviors on [001] BiOCl surface were investigated via DFT and Monte Carlo dynamics simulations (MCDS). The electronic properties analysis shows BiOX has a different energy band gap which varies with the halogen atom, BiOF has a wide band gap, and BiOI has a narrow band gap. Phonon dispersion studies confirmed the geometric stability of optimized BiOX structures, while thermodynamic evaluations revealed that BiOX exhibits hard material characteristics at higher temperatures but softer characteristics at lower temperatures. The electronic band structure indicates that doping introduces additional extrinsic electronic states within the energy band gap. Partial density of states (PDOS) analysis confirms that the extrinsic band within the forbidden energy gap arises from the dopants. Consequently, doping with post transition metals and co-doping with bromine have enhanced the electronic and optical properties of the BiOCl crystal. The molecular interaction analysis of dye interactions with water revealed a stable electronic structure in an aqueous medium. Based on the assessed energy gaps, methylene blue (MB) proves to be a stronger electron donor compared to methyl orange (MO) and methyl red (MR). Conversely, MO exhibits a greater electron-accepting capacity. The electrophilicity index result shows that MB interacts more with BiOCl crystals than MO and MR dye. The 2D-reduced density gradient graph and 3D isosurfaces of the non-covalent interaction analysis confirm repulsive, attractive, and weak interactions. The molecular electrostatic potential map analysis of the dyes revealed regions of varying potential values indicating both nucleophilic and electrophilic sites. MCDS results shows MO has a higher adsorption energy of -89.34 kcal/mol than MB and MR. Similarly, the experimental results show that the synthesized samples have a nanosheet with a layered structure. The absorption intensity of the Sn-doped samples exhibited a redshift and relatively had a higher excitation lifetime compared to pristine BiOCl. Furthermore, the electronic band gaps obtained from the computational and experimental results are consistent with each other. In conclusion, this study will help to create more effective and customized adsorbent materials for dye removal applications, advancing environmental remediation technologies.

1

INTRODUCTION

1.1 Background of the Study

The rapid advancements in urbanization, industrialization, and healthcare have significantly contributed to environmental pollution, presenting a considerable challenge to sustainable development (Bhat and Sundaram, 2015). Among the various forms of pollution, water pollution has escalated into a critical issue, with dyes such as methylene blue (MB), methyl orange (MO), methyl red (MR) and antibiotics being major contributors (Aneyo et al., 2016). These substances are extensively utilized in industries such as textiles, paints, and plastics (Zheng et al., 2023; Yang et al., 2023b). Dyes can affect the physical and chemical properties of water, including oxygen levels and pH, which are vital for aquatic life (Rauf and Hisaindee, 2013). Therefore, the presence of these dyes in the environment has raised concerns about their potential harmful effects on human health and the ecosystem (Khattab et al., 2020; Islam et al., 2023). Addressing the environmental pollution caused by the discharge of dye-containing effluents has become a pressing concern. Thus, interest in developing effective methods for removing dyes from wastewater is increasing. Photocatalysis has emerged as a promising technology capable of addressing these environmental challenges by utilizing solar energy to convert pollutants into harmless by-products under mild conditions (Zhao et al., 2023).

Recently, various types of nanostructured materials such as semiconductors, non-noble plasmonic metal (Sayed et al., 2022), metal oxides(Mubeen et al., 2023; Wang et al., 2023), polymers (Xie et al., 2023b; Zhang et al., 2023), composites (Tharuman et al., 2023; Zahraei et al., 2023), etc., have been used for photocatalytic applications due to their unique properties at the nanoscale (Mubeen et al., 2023; Tharuman et al., 2023; Wang et al., 2023; Sayed et al., 2022). In particular, semiconductor-based photocatalysts, TiO_2, ZnO, Fe_2O_3, BiOX, C_3N_4 etc., have attracted significant attention for their ability to effectively degrade pollutants and mineralize them into non-toxic products(Hazaraimi et al., 2022). These photocatalysts facilitate the purification of air and water by degrading organic pollutants through photo-assisted processes leveraging solar energy. However, traditional metal oxide semiconductors face several limitations, including wide band gaps, high recombination rates of photoinduced

charge carriers, and chemical instability (Zhang et al., 2020).

Recently, bismuth-based semiconductor (BBSs) photocatalysts are a new emerging research topic in the nanoscience and nanotechnology arena. Compared to metal oxide photocatalysts, BBSs has better photocatalytic efficiency owing to the Bi 6s and O 2p hybrid orbitals in the valence band (facilitate the separation of photogenerated carriers), and absorbs broad visible light radiation (Wang et al., 2020). Moreover, bismuth metal is benign to the environment (Wang et al., 2019), inexpensive and easily manufactured, and has been found to have plasmon resonance effect properties (Chen et al., 2022). BiOX is a V-VI-VII ternary semiconductor material that crystallizes in a tetragonal PbFCl-type structure. Its crystal structure consists of $[Bi_2O_2]$ blocks interleaved with double halogen slabs. The structure is two-dimensional, characterized by strong covalent Bi-O and Bi-X bonds, with halogen atoms (X-X) connected by weak van der Waals forces. The distinct layered structure of BiOX facilitates the separation of photo-generated electron-hole pairs, a critical requirement for effective photocatalysis. The electronic structure, optical, phonon, and thermodynamic properties of BiOX materials are interconnected and play vital roles in their photocatalytic activity. For example, Zhang et al. (2013) synthesized hierarchical BiOX (X=Cl, Br, I) nanoplate microspheres via a solvothermal process for methyl orange degradation. Lee et al. (2018) reported the fabrication of hierarchical BiOX (X= Cl, Br, I) crystals for hydrogen production through water splitting, achieving significant hydrogen production rates with BiOI crystals. Furthermore, Li et al. (2015a) employed microwave irradiation to synthesize BiOX (X = Cl, Br, I) crystals, which displayed superior photocatalytic activities compared to commercial TiO_2. Jia et al. (2021) developed BiOCl using a simple hydrolysis method for ciprofloxacin degradation.

From a computational standpoint, understanding the properties and behaviors of BiOX crystals involves utilizing various theoretical and computational techniques. DFT is commonly employed to investigate these materials' electronic structure, stability, and band gap properties. By simulating the crystal structure and performing energy calculations, researchers can predict how variations in composition and structure affect the material's performance. So far, several researchers have investigated the properties of BiOX crystals. For example, Zhang et al. (2006) and Huang and Zhu (2008) explored the electronic structure, photocatalytic activity, and properties of BiOX crystals. Zhou et al. (2019) and Barhoumi and Said (2021) further investigated the electronic band structure and energy band gap of BiOX crystals using methods like GW and BSE, with calculated band gaps closely aligning with experimental data.

This study employs a dual approach that combines computational calculations with experimental work. The computational methods were used for detailed predictions of the electronic, optical, vibrational, and thermodynamic properties of BiOX and doped BiOCl crystals. On the other hand, the experimental approach was utilized to synthesize and characterize using methods that yield empirical data on material properties, such as spectroscopy, mi-

croscopy, and X-ray diffraction (XRD). Furthermore, computational approaches were used to analyze the effects of doping on the charge distribution, band structure, optical, and stability of both pure and post transition metal doped BiOCl photocatalysts. This theoretical calculation with the experimental results provides a comprehensive understanding of the properties of BiOX for photocatalytic application.

1.2 Statement of the Problem

BiOX has attracted significant attention due to its remarkable photocatalytic efficiencies and unique structural features. Its layered structure facilitates the separation of photo-generated electron-hole pairs, which is essential for effective photocatalysis. Moreover, multiple halogen constituents enable the tuning of electronic and optical properties, thereby enhancing light absorption and photocatalytic activity. Previous studies have shown that BiOCl exhibits remarkable photocatalytic activity, particularly for the degradation of organic pollutants and the production of hydrogen from water splitting.

However, several researchers reported that BiOCl still faces challenges such as a fast charge recombination rate and a weak visible-light response, which limit its application in photocatalysis. To solve this challenges several studies have reported that metal doping, including Nb, W, Sn, In, Al, Zn, Co, Ti, Ni, Mo, Cd, and Fe, has been used to modify the energy band width of BiOCl (Nussbaum et al., 2014a; Liu et al., 2022a; Mokhtari and Tahmasebi, 2021; Attri et al., 2023). Similarly, non-metal elements, such as sulfur (S), bromine (Br), boron (B), nitrogen (N), and carbon (C), have been used to adjust the band gap of BiOCl and improve its photocatalytic activity (Chen et al., 2015; Zhang et al., 2022; Yao et al., 2021; Meng and Zhang, 2016).

Achieving high visible light absorption and preventing fast recombination simultaneously is another challenge in the doping method. To overcome this challenge, researchers have explored co-doping of metal and nonmetal, because it takes advantage of synergetic effects (Yang et al., 2023a; Xie et al., 2023a). Metal elements in co-doping can be used to modify the CB edge, whereas non-metal doping modifies the VB edge. While there is a wealth of literature on BiOCl, there remains a significant gap regarding the exploration of its electronic and optical properties in the context of post-transition doping and Br-co-doping. Additionally, there has been no prior work on the molecular interactions of different dyes in water and their adsorption behavior on the surface of BiOCl crystals. Investigating these areas could lead to new insights and enhancements in its photocatalytic performance.

To address these gaps, post-transition elements such as indium (In), tin (Sn), and thallium (Tl) were used as dopants, along with Br, to enhance the electronic and optical characteristics of BiOCl crystals. Furthermore, the molecular interactions and adsorption behavior of various dyes on the BiOCl surface were also investigated.

1.3 Objectives of the Study

1.3.1 General Objective

The general objective of this research is to study post-transition metals doped bismuth oxyhalides for photocatalyst applications using computational and experimental approaches.

1.3.2 Specific Objectives

The specific objectives of this study are:

- to determine the structural, optical, Raman, phonon, and thermodynamic properties of pure BiOX using DFT methods.
- to analyze the effect of post-transition metal doping and co-doping on electronic and optical properties of BiOCl crystal.
- to identify the molecular surface interactions and adsorption behavior of various dyes on BiOCl surfaces using DFT and MCDS methods.
- to analyze the structural, morphological and optical properties of pure BiOCl and Sn-doped BiOCl nanopasheets using different characterization techniques.

1.4 The scope of the study

This study employs DFT to investigate the structural, optical, Raman, phonon, and thermodynamic properties of pure bismuth oxyhalides (BiOX). The primary objective is to establish a foundational understanding of the intrinsic characteristics of BiOX, which are crucial for assessing its potential applications. Following this analysis, the effects of post-transition metal doping and Br co-doping on the electronic and optical properties of BiOCl are explored. This investigation specifically examines the alterations in the material's electronic structure and light absorption capabilities induced by doping, which are critical factors for enhancing photocatalytic performance.

The experimental phase encompasses the synthesis of pure BiOCl and Sn-doped BiOCl nanosheets. An analysis of the structural, morphological, and optical properties of the synthesized samples is conducted and compared with the theoretical findings. Furthermore, the study investigates the molecular interactions and adsorption behavior of various dyes on the surface of BiOCl, utilizing DFT calculations and Molecular Dynamics Simulations (MCDS). This multifaceted approach aims to deepen the understanding of BiOCl's potential in photocatalytic applications, particularly in the degradation of dyes.

1.5 Significance of the Study

This research explores BiOX using both theoretical and experimental approaches, emphasizing several important features. It establishes a foundational understanding of BiOX properties, including structural, optical, and thermodynamic characteristics via DFT, which is

essential for its applications in optoelectronics and photocatalysis. The research explores the effects of post-transition metal doping on the electronic structure and light absorption of bismuth oxychloride (BiOCl), enhancing its photocatalytic performance for environmental remediation. By synthesizing and analyzing pure and Sn-doped BiOCl nanosheets, the study bridges theoretical predictions with experimental, validating DFT methods and elucidating the influence of dopants. Additionally, it investigates molecular interactions and dye adsorption behaviors critical for optimizing dye degradation processes, thus contributing to the field of sustainable materials science and paving the way for efficient technologies in energy and water purification. The findings of this research support the development of economically viable and scientifically advanced materials for photocatalytic applications. Furthermore, the study lays a solid basis for further research in photocatalysis and related fields, allowing scientists to explore novel approaches to enhancing photocatalytic stability and efficiency by comprehending post-transition doping effects.

1.6 Document Organization

This dissertation is structured into five chapters, each focusing on a distinct aspect of the research regarding the properties and applications of bismuth oxyhalides and related materials. Chapter 1 provide an essential background on bismuth oxyhalides, their relevance in photocatalysis, research gaps, and the motivations for the study, while outlining the research objectives. Chapter 2 presents a comprehensive literature review related to bismuth oxyhalide materials, including basic density functional theory, properties of BiOX, the synthesis methods and photocatalytic applications. Chapter 3 details the materials and methods used, which divided into two sections: Computational Methods, which discusses the theoretical approaches, such as DFT, and Experimental Methods, which outlines the synthesis and characterization techniques employed. Chapter 4 showcases the results from both computational and experimental analyses, offering insights into the electronic, optical, and structural properties of the materials studied, and discusses their implications for photocatalytic applications. Finally, Chapter 5 summarizes the conclusion of key findings, highlights their significance, and proposes recommendations for future research directions.

2

REVIEW OF RELATED LITERATURE

2.1 Bismuth Oxyhalides Materials

BiOX is a group of layered semiconductor materials that have garnered interest due to their unique structural characteristics and promising photocatalytic properties. Research on BiOX dates back several decades, but significant advancements have been made since the early 2000s (Gujar et al., 2005; Wakjira et al., 2024). Early studies primarily focused on their synthesis and fundamental properties, with a particular emphasis on understanding their structural and electronic characteristics. In the late 2000s and early 2010s, researchers began exploring the photocatalytic capabilities of bismuth oxyhalides, particularly for environmental applications such as pollutant degradation and water purification (Zhang et al., 2006). Investigations highlighted the effectiveness of BiOX materials in degrading organic contaminants under UV light. The interest in these materials continued to grow as the demand for efficient and sustainable technologies increased, particularly in light of global environmental challenges.

Despite advancements, pristine BiOX photocatalysts exhibit certain limitations. A primary drawback is their photocatalytic efficiency, which is intrinsically linked to their stability (Baaloudj et al., 2022; Wang et al., 2019). Recently, band gap engineering through elemental doping has been an effective technique for enhancing photocatalytic activity as it regulates the optoelectronic properties and dynamics of the materials (Liu and Peng, 2020). In photocatalysts, doping is one of the primary objectives to trap photoexcited charge carriers and to promote their separation. There are two distinct types of elemental doping: metal and non-metal doping. Metal doping can impact the electronic structure of photocatalysts in two ways. Firstly, it introduces defects in the crystal, which increases the absorption properties of the photocatalyst and enhances the lifespan of the photogenerated charge carrier. Secondly, it generates a surface plasmon resonance (SPR) effect on a Bi-based semiconductor surface. The presence of SPR can robust the spectral response of semiconductor photocatalysts and enhance its quantum yield Chen et al. (2020). Noble metals such as Ag, Ni, Au, Pt, Pd, V, and others have been reported to be used to modify the electronic band structure of Bi-based semiconductor photocatalysts. These metals absorb photo-induced electrons on

the surface of semiconductor materials and enhance the lifespan of photogenerated charge carriers, thereby boosting photocatalytic reactions.

Doping materials with post-transition metal ions can introduce lattice defects in a semiconductor or change the crystallinity, inhibiting the recombination of electron-hole pairs and prolonging the life of the carriers (Zulkiflee et al., 2023a). The variable valence states and 3d orbits of post-transition metals have a great impact on the photoelectrochemical properties of semiconductors, and doping with certain metal ions can also extend the light absorption region. The metal ions incorporate into the crystal lattice, producing impurity levels in the forbidden band of a semiconductor. The red shift is attributed to the transition between the impurity levels to the CB or VB. Usually, highly efficient doped photocatalysts depend largely on tuning by doping with transition metal ions, which should satisfy two criteria: (1) The dopant can capture the electron and hole and further enable effective local separation. (2) The trapped electron and hole can be released and migrate to the interface (Belousov et al., 2023).

The introduction of non-metal dopants creates additional extrinsic electronic states within the energy bandgap. Two primary hypotheses have been suggested to explain this phenomenon: (i) the maximum of the valence band (VB) is elevated due to the hybridization of the valence orbitals of the non-metal elements, and/or (ii) the formation of localized states originating from the valence orbitals of the non-metals. The first scenario could result in a band-to-band absorption edge, allowing electrons in the newly formed VB to transition into the conduction band (CB). In contrast, the second scenario would preserve the original absorption edge while potentially introducing minor absorption features, such as shoulder or tail peaks (AlMohamadi et al., 2024). This leads to improved optical properties of pure BiOX photocatalyst. Furthermore, it enhances charge transmission, which promotes the effective separation of electron-hole pairs and hinders the recombination of photoinduced charge carriers. Liang et al. (2019) successfully conducted a simple hydrothermal synthesis to prepare a dual-doped Bi_2WO_6, decorated with metallic bismuth (Bi) and nonmetallic carbon (c) atoms. The synthesized material was instigated with different characterization techniques. The results showed that the co-decorated C / Bi Bi_2WO_6, exhibited significantly higher photocatalytic activity than the undoped Bi_2WO_6, when decomposing various industrial pollutants under visible light. The synergistic effects of SPR and C doping are attributed to the increased photocatalytic activities (Qian et al., 2016).

Another alternative in band gap engineering is the deposition of cocatalysts on the surface of BiOX, as it enhances charge carrier separation and improves the efficiency of specific reactions. Co-catalysts, such as noble metals (e.g., Pt, Au) or co-catalysts like NiO or CoO_x, can serve as active sites for charge transfer and promote specific reaction pathways. The appropriate choice and deposition of co-catalysts can accelerate the kinetics of photocatalytic reactions, leading to enhanced efficiency. The key advantages of doping on photocatalysts are i) enhancing visible light absorption, ii) efficient charge carrier separation, improving

catalytic activity, iv) extended lifespan and stability and v) impart selectivity and tunability to photocatalysts, enabling control over the types of reactions they can catalyze (Feng et al., 2021).

The photocatalytic performance of a semiconductor is contingent upon the semiconductor's band edge potentials and the adsorbed species' redox potential. From a thermodynamic perspective, for effective photocatalytic reactions, the equilibrium potential of the acceptor species must be lower (more positive) than that of the conduction band (CB), while the equilibrium potential of the donor species should be higher (more negative) than that of the valence band (VB). The redox potentials of the VB and CB are critical in influencing photocatalytic activity. Generally, a more positive maximum in the VB indicates a stronger oxidizing capability of the holes, while a more negative minimum in the CB signifies a stronger reducing potential of the electrons. From a kinetic standpoint, a greater degree of delocalization in the VB or CB can enhance the migration efficiency of charge carriers, thereby facilitating photocatalytic oxidation and reduction reactions (AlMohamadi et al., 2024).

2.2 Crystal Structure and Properties of BiOX

2.2.1 Structural and Electronic Properties

BiOX are p-type semiconductors, meaning the energetic arrangement of their conduction and valence bands means favor reduction processes over oxidation. Pristine BiOX are layered materials with an open crystal structure, exhibiting properties such as easy modification and formation of heterogeneous structures with other materials, chemical stability and the ability to absorb UV and visible light. The crystal structure consists of alternating layers of bismuth oxide and halides, contributing to their photocatalytic effectiveness. The anisotropic nature of BiOX facilitates charge separation and migration, enhancing their photocatalytic performance.

The bismuth (Bi) atoms and halogen (X) atoms form a lattice where the bonding characteristics lead to distinct regions of positive and negative charge density (Castillo-Cabrera et al., 2022). These materials crystallize in a tetragonal matlockite structure, characterized by the P4/nmm space group. The layered structure of BiOX is composed of [X–Bi–O–Bi–X] slabs held together by weak van der Waals interactions as shown in Fig. 2.1. Within each [X–Bi–O–Bi–X] slab, bismuth (Bi) atoms are coordinated to four oxygen (O) atoms and four halogen (X) atoms. This arrangement leads to strong intralayer covalent bonding, while the interlayer van der Waals forces contribute to the material's layered structure. The combination of strong intralayer bonding and weak interlayer interactions gives rise to anisotropic properties in BiOX materials. This anisotropy is observed in their structural, electrical, optical, and mechanical properties, making them promising candidates for various applications (Bhachu et al., 2016).

The band structure and density of states are fundamental concepts in solid-state physics,

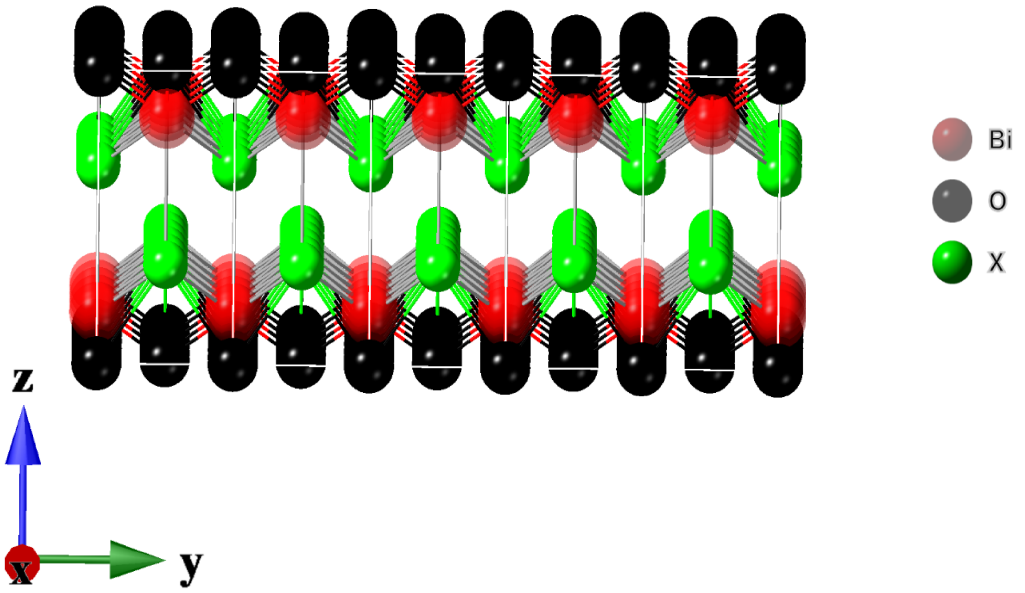

Figure 2.1: Crystal structures of BiOX

providing a comprehensive description of the electronic structure of materials. The band structure arises from the interaction of atomic orbitals in a periodic lattice. When atoms come together to form a solid, their atomic orbitals overlap and hybridize, forming bands of allowed energy levels. These bands are separated by forbidden energy gaps, where no electronic states exist. The highest occupied band at absolute zero temperature is called the valence band. It contains the electrons responsible for bonding within the solid. The lowest unoccupied band is called the conduction band. Electrons in this band are free to move and contribute to electrical conductivity. The energy difference between the valence and conduction bands is known as the band gap (E_g) (Arumugam et al., 2021). The size and nature of the band gap determine how a material interacts with light and electricity, influencing its conductivity and optical properties. In most cases, the electron momentum at the valence band's top and the conduction band's bottom do not exist at the same k-point. A direct band gap occurs when the maximum energy level of the valence band and the minimum energy level of the conduction band are aligned in momentum space as shown in Fig. 2.2 (a). This alignment allows electrons to transition directly between these bands without the need for a change in momentum. In contrast, an indirect band gap occurs when the maximum of the valence band and the minimum of the conduction band are located at different momentum values as shown in Fig. 2.2 (b). As a result, an electron transitioning from the valence band to the conduction band must also change its momentum, typically involving the interaction with a phonon (a quantized mode of vibration in a crystal lattice).

The electronic density of states (DOS) is a property on how many electronic states exist per volume per energy. It provides information on the distribution of electronic states

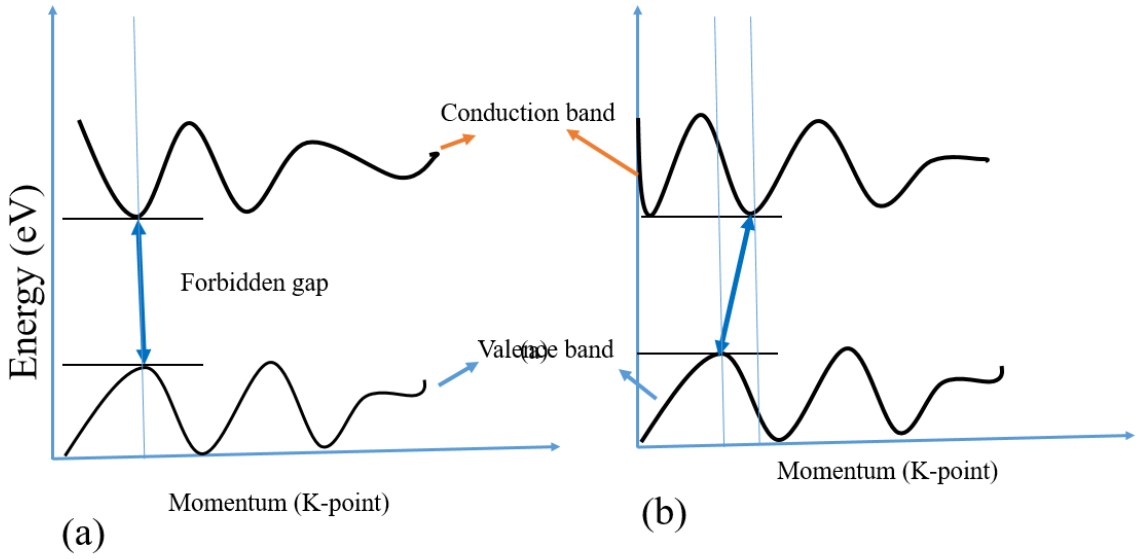

Figure 2.2: Schematic diagram of electronic band structure (a) direct band gap and (b) indirect band gap.

within the energy bands. The DOS exhibits sharp peaks and valleys, known as Van Hove singularities, corresponding to critical points in the band structure where the energy gradient vanishes. The DOS is directly related to the band structure. Peaks in the DOS correspond to regions of high density of states in the band structure, while valleys indicate regions with low density of states. The DOS near the Fermi level determines the material's conductivity.

2.2.2 Optical Properties

The interaction of light with matter results in a variety of phenomena, including transmission, reflection, and scattering. At the microscopic level, light, or more precisely, photons, interacts with electrons within the material. These interactions give rise to the material's optical properties, which can be broadly categorized into absorption, emission, and scattering. In semiconductors, optical absorption (or emission) is particularly sensitive to the energy of the incident photon. Absorption occurs when the photon energy exceeds the semiconductor's band gap, promoting an electron from the valence band to the conduction band.

The dielectric function Eq. (2.1) describes the response of a material to an external applied field and is related to the material's ability to polarize and store electrical energy (Kumar et al., 2009).

$$\epsilon(\omega) = \epsilon_1(\omega) + i\epsilon_2(\omega) \tag{2.1}$$

where $\epsilon(\omega)$ is the linear response of electrons and optical transitions to photons expressed as a function of the angular frequency. The real part is related to the electronic polarizability of the crystal and is denoted by $\epsilon_1(\omega)$, while the imaginary part, which corresponds to the energy absorbance, is represented by $\epsilon_2(\omega)$. The imaginary part is computed from the momentum matrix between the occupied and unoccupied wave functions in the first Brillouin

zone using Eq. (2.2) (Okoye, 2004). The Kramer-Kronig relation Eq. (2.3) can be used to determine the real component of the dielectric function from the imaginary component for all positive frequencies Wu and Wu (2016).

$$\epsilon_2 = \frac{\pi e^2}{\epsilon_o V} \frac{1}{q^2} \left[\psi_k^c e^{-iq.r} \psi_{k'}^{\nu}\right]^2 \tag{2.2}$$

where e is the charge on an electron, ϵ_o is the permittivity of free space, V is the volume of the unit cell, and q is the momentum transfer and k is wave number with k' = k+q.

$$\epsilon_1(\omega) = 1 + \frac{2}{\pi} p \int_0^{\infty} \frac{\omega' \epsilon_2(\omega')}{\omega'^2 - \omega^2} d\omega' \tag{2.3}$$

Where p denotes the Cauchy principal value, ω' is the angular optical frequency variable, $\epsilon_1(\omega)$ is related to the absorption coefficient and $\epsilon_2(\omega')$ is related to the refractive index. The dielectric constant (ϵ) is related to the ratio of the speed of light in a vacuum (c) to the speed of light in a medium (v) through $\epsilon = N^2$. The optical properties of a medium are directly linked to its dielectric constant using Eq. (2.4).

$$N = \sqrt{\epsilon} = n + ik \tag{2.4}$$

The refractive index (n) and the extinction coefficient (K) are typically not measured directly in optical experiments. Instead, the absorption coefficient (σ) and the reflectivity (R) are the measurable quantities (Beal and Liang, 1976). Once the dielectric function is known, the absorption coefficient and reflectivity can be calculated using Eq. (2.5) and (2.6), respectively.

$$\sigma = \frac{2K\omega}{c} \tag{2.5}$$

$$R = \frac{(n-1)^2 + K^2}{(n+1)^2 + K^2} \tag{2.6}$$

where n and K are calculated using Eq. (2.7).

$$n^2 = \frac{1}{2}([\epsilon_1^2 + \epsilon_2^2]^{\frac{1}{2}} + \epsilon_1); K^2 = \frac{1}{2}([\epsilon_1^2 + \epsilon_2^2]^{\frac{1}{2}} - \epsilon_1) \tag{2.7}$$

The imaginary part of the inverse dielectric tensor is proportional to the electron energy loss spectrum (EELS) as expressed in Eq. (2.8).

$$EELS = Im[\frac{-1}{\epsilon(\omega)}] \tag{2.8}$$

The real values of the dielectric permittivity, or equivalently, the complex dielectric function at imaginary frequencies, denoted as $\epsilon(i\omega)$, were determined using the Kramers-Kronig relations, as expressed in Eq. (2.9). This approach allows for the extraction of the frequency-

dependent dielectric response from the material's optical properties.

$$\epsilon(i\omega) = 1 + \frac{2}{\pi} p \int_0^\infty \frac{\omega' \epsilon_2(\omega')}{\omega'^2 + \omega^2} d\omega' \tag{2.9}$$

The joint density of states (JDOS) is a crucial concept in solid-state physics and materials science, particularly in the study of the electronic properties of materials. It describes the number of available electronic states at a given energy level for two interacting particles, such as electrons in a solid. The JDOS is defined as the density of states for two particles (often electrons) in a system, considering their energy levels. It quantifies how many pairs of states (e.g., an electron in the conduction band and a hole in the valence band) are available for a given energy. Mathematically, it can be expressed as (Cabrera et al., 2016):

$$g(E_1, E_2) = \frac{d^2 N}{dE_1 dE_2} \tag{2.10}$$

where E_1 and E_2 are the energies of the two particles, and N is the number of states. The absorption spectrum of a material can be understood by analyzing the JDOS. A prominent peak in the JDOS indicates a high density of available transitions at a specific energy difference, $E_f - E_i$. This energy difference corresponds to the energy of photons absorbed by the material. Consequently, a large peak in the JDOS directly translates to a peak in the absorption spectrum, signifying a high probability of photon absorption at that energy.

Non-resonant Raman spectroscopy is a valuable technique for probing molecular vibrations, lattice dynamics, and low-energy excitations in materials. Unlike resonant Raman spectroscopy, which relies on aligning incident laser frequencies with the electronic transitions of materials, non-resonant Raman spectroscopy operates independently of these transitions, with Raman scattering resulting from the inelastic scattering of light by molecules. Under non-resonant conditions, the incident photon energy does not match any electronic transitions, allowing the Raman signal to arise exclusively from the material's vibrational modes without electronic state enhancement (Boutahir et al., 2020). Key aspects of this method include the interaction of photons with molecular vibrations, which induces a temporary excited state and results in the emission of photons with energy corresponding to the vibrational levels. The emitted light can be classified into Stokes and anti-Stokes components, and the analysis of the Raman spectrum provides a distinct "fingerprint" of the molecular composition, offering insights into functional groups, molecular symmetry, and interactions within complex mixtures. This technique's capacity to characterize materials without requiring resonance makes it an effective analytical tool for understanding various material properties and behaviors.

2.2.3 Lattice Oscillations

Phonons, are quantized lattice vibrations of atoms in a crystal lattice. The relationship between the phonon frequency (ω) and wavevector (q) is known as the phonon dispersion relation, which provides a comprehensive picture of the vibrational modes within the solid. Their understanding is crucial for predicting and controlling the thermal, mechanical, and optical properties of solids, leading to advancements in various fields, including materials science, condensed matter physics, and nanoscience (Jessen and Deutsch, 1996). A crystal lattice with N atoms per unit cell exhibits 3N phonon modes, representing collective atomic vibrations. These modes are categorized as acoustic and optical phonons. Acoustic phonons (3 modes) have low frequencies, approaching zero at the Brillouin zone center, and represent long-wavelength vibrations where neighboring atoms move in unison. They are further classified as longitudinal (LA) or transverse (TA) based on the oscillation direction relative to wave propagation. Optical phonons (3N-3 modes) have higher frequencies and involve out-of-phase atomic motion. They are similarly classified as longitudinal (LO) or transverse (TO) based on the oscillation direction. The specific mode type can be identified by analyzing atomic displacements at the Brillouin zone center.

The phonon angular frequencies (ω_q) are determined by solving the simultaneous equation of motion for each q as

$$\sum_j D_{i_\alpha,j_\beta}(q)u_{j\beta}(q) = \omega_q^2 u_{i_\alpha}(q)\ (i_\alpha = 1,\ldots,3N), \tag{2.11}$$

where N is the number of atoms in the unit cell and $\alpha(\beta)$ corresponds to x, y, z components of oscillation. $u_{i\alpha}(u_{j_\beta})$ is a phonon eigenvector (or the amplitude of the phonon) of the $i^{th}(j^{th})$ atom. Summation on j_β is taken for neighbor atoms from a given i^{th} atom up to several nearest neighbors. $D_{i_\alpha,j_\beta}(q)$ is called the dynamical matrix, which is defined by

$$D_{i_\alpha,j_\beta}(q)u_{j_\beta}(q) = \frac{1}{\sqrt{M_i M_j}} F_{i_\alpha,j_\beta}(q) \tag{2.12}$$

where $M_i(M_j)$ is mass of the $i^{th}(j^{th})$ atom. F_{i_α,j_β} is second derivative of the total energy E_{tot} with respect to the displacements $(u_{i_\alpha}, u_{j_\beta})$ of atomic positions, which is called the inter-atomic force constant (IFC), which is given

$$F_{i_\alpha,j_\beta}(q) = \frac{\partial^2 E_{tot}}{\partial u_{i_\alpha}(q)\partial u_{j_\beta}(q)} \tag{2.13}$$

2.2.4 Thermodynamic Properties

The thermodynamic properties of BiOX crystals, including enthalpy, entropy, Gibbs free energy, and heat capacity, provide essential insights into their stability, phase behavior, and

overall performance in various applications. The statistical thermodynamic expressions used to determine the thermodynamic properties of the BiOX crystals in reciprocal space are listed in Eq. (2.14)-(2.18). Eq. 2.14 can be used to relate the system's internal energy to its temperature.

$$E(T) = E_T + E_{zp} + \int \frac{h\omega}{e^{\frac{\hbar\omega}{KT}} - 1} F(\omega) d\omega \tag{2.14}$$

where E_T is the total electronic energy at 0 K, E_{zp} is the zero-point vibrational energy, h is Planck's constant, k is the Boltzmann constant, and $F(\omega)$ is the vibrational density of states. The zero-point vibrational energy of the BiOX crystal was calculated using Eq. (2.15),

$$E_{zp} = \int F(\omega) h\omega d\omega \tag{2.15}$$

The vibrational contribution to the free energy, F, is given by:

$$F(T) = E_T + E_{zp} + KT \int F(\omega) ln \left[1 - exp(-\frac{\hbar\omega}{KT}) d\omega\right] \tag{2.16}$$

The vibrational contribution to the entropy, S, can be obtained using:

$$S(T) = K \left[\int \frac{\frac{\hbar\omega}{KT}}{exp(\frac{\hbar\omega}{KT}) - 1} F(\omega) d\omega - ln \left[1 - exp(-\frac{\hbar\omega}{KT}) d\omega\right]\right] \tag{2.17}$$

The expression in Eq 2.17 typically includes two main terms, each representing different contributions to the overall entropy. The first terms represents the thermal energy contribution of the phonons to the entropy density. As temperature increases, this term becomes significant because it accounts for the average energy per mode that contributes to disorder in the system. The second terms represents the contribution to entropy from the phonon modes at a given frequency. This term reflects how the number of available phonon states increases with temperature, leading to higher entropy as more states become thermally accessible. At higher temperatures, more phonons can be excited, resulting in greater disorder and thus higher entropy. Furthermore, the lattice contribution to heat capacity (Cv) can be calculated using Eq. (2.18)

$$C_V = K \int \frac{(\frac{\hbar\omega}{KT})^2 e^{\frac{\hbar\omega}{KT}}}{\left[(\frac{\hbar\omega}{KT})^2 - 1\right]^2} F(\omega) d\omega \tag{2.18}$$

The temperature dependence of the heat capacity is given by the Debye model Eq. (2.19):

$$C = \frac{12\pi^2 N K_B}{5\theta_D^3} T^3 \tag{2.19}$$

2.3 An overview of Density Functional Theory

The main objective of computational material science is to predict and control material properties through an understanding of atomic, molecular, crystalline, and microscopic structures. The complex interactions between electrons and nuclei determine the properties of the materials. The materials are held together by a finely balanced repulsive and attractive Coulomb interaction between the nuclei and electrons (Engel, 2011). Electrons are treated as wave functions in quantum mechanics instead of classical particles. Hence, the Schrödinger equation is used to describe the interactions between electrons and nuclei. A system of electrons and nuclei is described by the Schrödinger Eq. (2.20)

$$\hat{H}\psi = E\psi \tag{2.20}$$

where $\hat{H}$ is the Hamiltonian operator of the system given as Eq. 2.21, E is the total energy of the electrons and nuclei, and ψ is the wavefunction of the system (Kohn and Sham, 1996).

$$H = T_n + V_n + T_e + V_e + V_{en} \tag{2.21}$$

where, T_n is the kinetic energy of nuclei, T_e is the kinetic energy of electron, V_n Coulomb repulsion between a pair of nuclei, V_e Coulomb repulsion between a pair of electrons and V_{en} Coulomb attraction between electrons and nuclei. Hence, the more complete description of the Schrodinger equation is expressed as Eq. (2.22)

$$\left[\frac{\hbar^2}{2m}\sum_{i=1}^{N}\nabla^2 + V(r_i) + \sum_{i=1}^{N}\sum_{j<i}U(r_i, r_j)\right]\psi = E\psi \tag{2.22}$$

Fortunately, in most practical purposes, the potential field is not a function of time (t), or even if it is a function of time, it changes relatively slowly compared to the dynamics we are interested in. However, the nuclei are much heavier than the electrons. Moreover, the average speed of the nuclei is much smaller than that of the electrons. Therefore, we can assume that the electrons will follow the nuclear motions without any delay, and we can decouple the electronic and nuclear motions to the first approximation, which is known as the Born-Oppenheimer approximation. Hence, Eq. (2.20) is rewritten as Eq. (2.23).

$$\psi(r, t) = \psi(r)f(t) \tag{2.23}$$

That reduces our task to solving only time-independent Schrödinger equation:

$$\left[\frac{-\hbar^2}{2m}\nabla^2 + V(r)\right]\psi = \epsilon\psi \tag{2.24}$$

However, the Schrödinger equation can only be analytically solved for systems with a

single electron. The real physical system consists of a large number of atoms. Because of the intricacy of the Coulomb interactions, the Schrödinger equation can only be solved with some approximations for any system containing more than two electrons. To overcome this problem, many researchers have been developing methods of approximation since the late 1920s. The most successful method in the computational realm is the density-functional theory (DFT). The DFT is a quantum-mechanical theory of approximation in which the Coulomb interaction between electrons is expressed by a functional of the electron density (Engel, 2011). It calculates the ground-state electronic state of materials. Hence, it allow the prediction and calculation of material behavior at the ground state on the basis of quantum mechanical considerations. The electronic structure is evaluated using a potential acting on the system's electrons. This DFT potential is constructed as the sum of external potentials V_{ext} , which is determined solely by the structure and elemental composition of the system, and an effective potential V_{eff}, which represents the electron-electron, electron-phonon, and nuclei-electron interaction (Kohn and Sham, 1996).

The nuclei within the material are nearly immobile, and X-ray crystallography allows for the precise determination of their locations. To determine the electronic energy band, we can therefore fix the locations of the nuclei in real space with zero kinetic energy. At that point, Vn turns into an external potential or just a constant. In such case, the problem that we have to solve becomes a purely electronic one and Eq. 2.21 becomes, (2.25)

$$H = T_e + V_e + V_{en} \tag{2.25}$$

The Schrödinger equation becomes coupled many-body equation.

$$\left[\frac{-\hbar^2}{2m}\sum_{i=1}^{N}\nabla^2 + \sum_{i=1}^{N}V(r,t) + \sum_{i=1}^{N}\sum_{j<i}U(r_i,r_j)\right]\psi(r_1,r_2,...,r_N) = E\psi(r_1,r_2,...,r_N) \tag{2.26}$$

With today's available computing power, it is far from feasible to solve the actual electronic wave function of a condensed matter system, where N is of the order of 10^{23}.

2.3.1 Hartree-Fock Theory

Hartee method assumes for an n-electron system, each electron is independent and interacts with each other in an average way. Hence, the self-consistence field method is used to solve the equation of wave. And the total energy is the sum of all the energy of the electron. However, the Hartee method does not include two basic principles of quantum mechanics: the antisymmetry principle and Pauli's exclusion principles. Furthermore, it does not consider the exchange and correlation energies due to the n-electron nature of real system (Engel, 2011). Fock improves the Hartee methods by considering the n-electron system wavefunction as a combination of non-interacting one-electron wave functions which are expressed in the form of Slater determinant. Hatree-Fock theory is fundamental to many subsequent

theories of electronic structure. The generalized Slater determinant form of the N-electron system is

$$\psi = \frac{1}{\sqrt{N!}} \begin{vmatrix} \chi_1(r_1) & \chi_2(r_2) & \cdots & \chi_N(r_1) \\ \chi_1(r_2) & \chi_2(r_2) & \cdots & \chi_N(r_2) \\ \vdots & \vdots & \vdots & \ddots \\ \chi_1(r_N) & \chi_N(r_N) & \cdots & \chi_N(r_N) \end{vmatrix} \tag{2.27}$$

where the prefactor $\frac{1}{\sqrt{N!}}$ is a normalization constant and $\chi_i(r_i)$ are electron orbital states. The above antisymmetrized product can describe electrons that move independently of each other while they experience an average (mean-field) Coulomb force (Kohn and Sham, 1996).

2.3.2 Hohenberg-Kohn Theorem

The foundation of DFT rests upon two seminal publications: the work of Hohenberg and Kohn and the subsequent paper by Kohn and Sham (Epstein and Rosenthal, 1976). The initial formulation, presented in the Hohenberg-Kohn paper, is known as the Hohenberg-Kohn theorem. This theorem established the fundamental principle that the ground state electron density of a system uniquely determines its Hamiltonian, thus providing a framework for describing the system's properties based on its electron density. The second paper, by Kohn and Sham, introduced a practical method for applying the Hohenberg-Kohn theorem. This method, referred to as the Kohn-Sham equations (discussed in section 2.3.3), employs an effective potential to approximate the true electron interaction, allowing for the calculation of the ground state electron density and subsequently, other electronic properties of the system (Kohn and Sham, 1996). According to their theorems, the Hamiltonian is completely determined by the external potential $V_{ext}(r)$ for an N-electron system. Therefore, both the number of electrons and the external potential determine all electronic properties of the ground state energy. However, it is reasonable because the external potential is determined by the nucleus structure.

- **Theorem-I:** The external potential energy is a unique functional of the ground state electron density $n_0(r)$.
- **Theorem-II:** The ground state energy of the system is obtained via minimization of the energy functional with respect to the electron density, which is equivalent to ground state electron density (Salami and Shokri, 2021).

2.3.3 The Kohn-Sham Equations

As discussed in section 2.2.2 the Hohenberg-Kohn theorem, which guarantees to give the ground-state energy. Despite the theoretical elegance of the Hohenberg-Kohn theorem, it lacked an analytical solutions for determining the exact form of functional F[n(r)] given by Eq. (2.28), which relates the electron density to the system's energy. Kohn and Sham

(1965) addressed this challenge by introducing an explicit form for F[n(r)] and constructing a Schrödinger-like equation known as Kohn-Sham equation Eq. (2.29) based on this functional (Kohn and Sham, 1996). This equation, amenable to solution using the Self-Consistent Field (SCF) method, facilitated the implementation of DFT calculations within computer codes, making it a powerful tool for practical applications in quantum chemistry and condensed matter physics.

$$F(n) = T_o(n) + \frac{e^2}{2}\int \frac{n(r)n(r')}{|r-r'|}drdr' + E_{xc}(n) \tag{2.28}$$

The first term is the kinetic energy, the second is classical electrostatic self-interaction of the electron charge-density distribution, and the third is exchange-correlation energy in Eq.

$$\left[\frac{\hbar^2}{2m} + V(r) + V_H(r) + V_{XC}(r)\right]\psi_i = E\psi_i \tag{2.29}$$

Where E_i is the orbital energy of the corresponding Kohn-Sham orbital ψ_i, $V_H(r)$ is Hartee potential, V_{XC} is the exchange-correlation potential.

2.4 Basic Parameters in DFT Calculations

2.4.1 Total Energy and Self-Consistent Field

In quantum mechanics, the single-particle Schrödinger equation describes the behavior of a quantum particle in a potential. In the context of many-body systems, such as those encountered in DFT, the situation becomes more complex due to electron-electron interactions. The difficulty arises because V_H depends on the electron density, which in turn is determined by the wave functions obtained from solving the single-particle Schrödinger equation. This leads to a circular dependency: To calculate V_H one must first assume a form for Solve Schrödinger Equation: With this guess, the single-particle Schrödinger equation can be solved. From the wave functions ψ_i one computes a new density. This new density is then used to recalculate V_H, leading to a new V_{eff}, and the process repeats. The iterative process must converge to a self-consistent solution where the input density and the output density remain unchanged.

The total energy of a system is expressed as a functional of the charge density as

$$E(\rho) = T_s[\rho(r)] + J[\rho(r)] + \int \nu_{ext}(r)\rho(r)dr + E_{xc}[\rho(r)] \tag{2.30}$$

Where the first term in Eq. (2.30) is the kinetic energy of the non-interacting system, the second term is the classical Coulomb repulsion energy, the third term is the interaction of the external potential acting on the electrons, and the last term is the exchange and correlational energy and expressed as

$$E_{xc}[\rho(r)] = (V_{ee}[\rho(r)] - J[\rho(r)]) + (T[\rho(r)] - T_s[\rho(r)]) \tag{2.31}$$

Where $T[\rho(r)]$ is the kinetic energy of the interacting system and $V_{ee}[\rho(r)]$ is the non classical interaction between electrons.

The electron density is constructed from a set of one-electron wavefunctions called Kohn-Sham orbitals. These orbitals are solutions to a fictitious non-interacting system that has the same electron density as the real interacting system. The total electron density is calculated as the sum of the squares of the Kohn-Sham orbitals: The electron density is the main variable in DFT calculation. Therefore, the electron density for an N-particle system is given as

$$\rho(r) = \sum |\psi_i|^2 \tag{2.32}$$

Where ψ_i is the i^{th} Kohn-Sham orbital. Thus, it is necessary to determine the charge density by solving Kohn-Sham equations self consistently. Solving the electron density from the Kohn-Sham equation begins with a guess and continues iteratively until it converges. The flowchart of iteration is shown in Fig. 2.3.

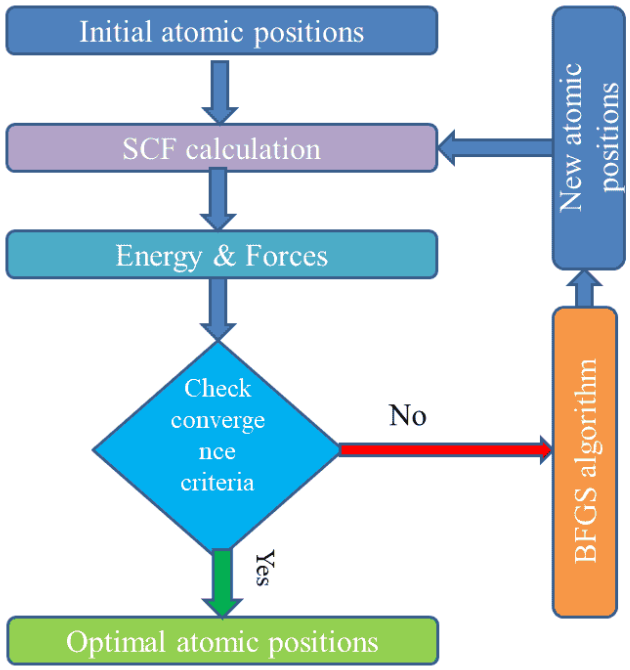

Figure 2.3: The flowchart of optimization of atomic positions

A simple method to damp charge oscillations during the iterative process is to use a linear combination of input and output densities as the input charge density to the next iteration using a mixing algorithm

$$\rho(r)^{new} = \alpha\rho(r)^{i} + (1-\alpha)\rho(r)^{new} \qquad 0 < \alpha < 1 \tag{2.33}$$

Electron density can be expressed in terms of a basis set. However, Gaussian and plane waves

are the most efficient for the description of the orbitals. A Gaussian basis set is localized at each atom to expand the Kohn-Sham orbitals and a plane wave basis set is not localized at each atom to describe the electron density.

2.4.2 Cut-off Energy and Pseudopotential

The size of the Hamiltonian matrix, N, is determined by the number of reciprocal lattice vectors G. As N increases, the accuracy of the calculation improves, but this also leads to an increase in the computer's memory size and computational time. Therefore, it's important to find an optimal N by plotting the total energy and computational time against N. In first-principles calculations, we typically don't compare N for different calculations, but instead use a cut-off energy in atomic units as a reference point which is expressed as

$$E_{Cutt-off} = \frac{\hbar^2}{2m} G_{max}^2 \tag{2.34}$$

where G_{max} is the largest reciprocal lattice vector. We use the cut-off energy because the values of N depend on the size of the unit cell (Garrity et al., 2014).

The pseudopotential selection for each atom also influences the choice of cut-off energy. For heavy elements, the solid-state properties are mainly determined by the valence electrons in the highest occupied orbitals, and the inner-core electrons in the 1s, 2s, and 2p atomic orbitals are less significant. The valence electrons located near the highest occupied orbitals primarily contribute to the properties, as they experience screened Coulomb potentials by core electrons, excluding the core region of the atom. A pseudopotential is a potential in which the core region of an atom is artificially smoothed out near r = 0, reducing the need for many G (or N) to obtain V_G with the same numerical accuracy. The pseudopotential is expressed as a function of the distance from the center of the atom (r) and the electron density based on the density-functional theory.

The three commonly used types of pseudopotentials are norm-conserving pseudopotentials, ultrasoft pseudopotentials, and projector-augmented wave (PAW) methods, each with unique characteristics and applications. Norm-conserving pseudopotentials are designed to ensure that the norm of the pseudowavefunctions matches that of the all-electron wavefunctions. This requirement enhances the accuracy and transferability of the pseudopotentials across different systems. Additionally, an important condition is imposed: the energy derivative of the logarithmic derivative of the pseudofunctions must correspond to that of the all-electron wavefunctions. This strict norm conservation ensures that the core regions are accurately represented while simplifying the valence electron interactions.

Ultrasoft pseudopotentials, on the other hand, relax the norm-conservation constraint, which allows for the incorporation of multiple potentials for each angular momentum channel. This flexibility results in softer potentials that enable the alignment of all-electron eigenvalues over a wider energy range. One of the significant advantages of ultrasoft pseudopoten-

tials is the larger core radius that can be achieved compared to norm-conserving pseudopotentials of similar accuracy, enabling calculations that reduce computational costs without compromising results.

The PAW method represents a more sophisticated framework for handling atomic potentials. In this approach, the atomic potential is divided into two distinct regions: the core region and the valence region. In the core region, wavefunctions are treated explicitly as all-electron wavefunctions, while in the valence region, a simpler pseudopotential is employed. The PAW method uses projectors to reconstruct the all-electron wavefunctions from the simpler pseudopotential wavefunctions, achieving both accuracy and computational efficiency.

2.4.3 K-point for Brillouin Zone Integration

To calculate the periodic system's first principle electronic structure, we must perform the numerical integration in the wave-number space, specifically the integration in the Brillouin zone (Kratzer and Neugebauer, 2019).

$$\int f(k_x, k_y, k_z) dk_x dk_y dk_z \tag{2.35}$$

The integral is replaced by the summation of the discrete sample points:

$$\sum w_i f(k_x^i, k_y^i, k_z^i) \tag{2.36}$$

where the summation is taken over the sampling points (k_x^i, k_y^i, k_z^i) with weight w_i. A quantum mechanical quantity f(k) on one k-point may have a physical property related to that on another k-point f(R.k) by the symmetry operation R; these two quantities have the same value because of the periodic structure. To obtain information about the other sampling k-points, it is practical to compute the quantum mechanical quantity only in the representatives of the sampling k-points. These representatives ought to be taken in the irreducible Brillouin zone, which is the smallest segment of the integral's range and where sampling point weights may vary (Setyawan and Curtarolo, 2010).

The wave-number vector is given by the coefficients (k_1, k_2, k_3) on the reciprocal lattice vectors (G_1, G_2, G_3), which are expressed as $K = k_1 \cdot G_1 + k_2 \cdot G_2 + k_3 \cdot G3$. The uniform k-points in the whole Brillouin zone are generated by using

$$k_1^{(i,j,l)} = \frac{(i-1)+s_1}{N_1};\ k_2^{(i,j,l)} = \frac{(j-1)+s_1}{N_2};\ k_3^{(i,j,l)} = \frac{(l-1)+s_1}{N_3} \tag{2.37}$$

where N_1, N_2, and N_3 are the numbers of divisions along each reciprocal vector and (s_1, s_2, s_3) are the shift of the origin (Kratzer and Neugebauer, 2019).

2.5 Exchange-Correlation Functional

In DFT, the most important energetic contributions are accounted for the kinetic energy of the non-interacting system and electrostatic interactions of the electrons with their charge density and with the nuclear cores. The exchange-correlation energy accounts for the remaining electronic energy not included in the non-interacting kinetic and electrostatic terms. Currently, there is no analytical solution to solve the Kohn-Sham equations. Therefore, to solve this puzzle in the DFT calculation, we use different approximation methods such as the semilocal exchange correlation functional, the local density approximation (LDA), generalized gradient approximations (GGA), or hybrid.

A LDA is an approximation for the exchange-correlation energy (E_{xc}), which depends solely on the value of the electronic density at each point in space. A local density approximation for the exchange-correlation energy is written as

$$E_{XC}^{LDA} = \int d^3r E'_{XC}(\rho_o)|_{\rho_o \to \rho(r)} \tag{2.38}$$

where $E'_{XC}(\rho_o)$ is the exchange-correlation energy in a homogeneous electron gas with the density $\rho_o = \rho(r)$. The LDA is exact in the limit of high density or a slowly varying charge-density distribution. Hence, for weakly correlated materials, such as semiconductors and simple metals, the LDA accurately describes structural and vibrational properties (Lewin et al., 2019). The electron density is not distributed uniformly in real crystals. Hence, LDA approximation cannot predict the exact exchange energy in the real crystal. This problem can be solved by considering the gradient of the electron density.

The GGA greatly improves the calculation results of the energy related to electrons and exchange. In GGA, the exchange-correlation energy is the functional of two variables, i.e, electron density and electron-density gradient which is given below. The most commonly used GGA functions include PW91 and Perdew–Burke Ernzerhof (PBE) (Perdew, 1991).

$$E_{XC} = E_{XC}[\rho(r), \nabla\rho(r)] \tag{2.39}$$

Hybrid functionals represent a significant advancement in DFT, combining the strengths of both Hartree-Fock (HF) theory and pure DFT functionals. By incorporating a portion of exact exchange from HF theory into the DFT exchange-correlation functional the hybrid functional has demonstrated remarkable accuracy for a wide range of systems and properties. Generally, the accuracy of DFT method depends on different parameters such as the choice of the exchange correlation functional, pseudopotentials, initial spin states, energy cutoffs, and k-point grid. Furthermore, numerical convergence must often be monitored and tuned through the choice of matrix diagonalization schemes, charge mixing strategies, and k-space integration methods (Arbuznikov, 2007).

2.6 Molecular Dynamics Simulation

The potential energy surface (PES) of a small molecule is a multidimensional landscape that represents the energy of the molecule as a function of its atomic positions. Understanding this surface is crucial for predicting molecular behavior, reactivity, and stability (Cao et al., 2021). The lowest point on the PES, representing the most stable configuration of the molecule. Identifying this point is essential for understanding the molecule's equilibrium state. The PES can have numerous local minima due to variations in bond lengths, angles, and torsional angles. This complexity arises from the interplay of various types of molecular interactions like van der Waals forces, hydrogen bonding, and electrostatic interactions (Ngambia et al., 2019). There are different methods for finding the global minimum like Monte Carlo Algorithms and molecular dynamics. The Monte Carlo method is a probabilistic method that involve randomly sampling configurations of the system. By using a defined temperature, Monte Carlo algorithms can help escape local minima, allowing for exploration of the PES. Techniques such as simulated annealing can be employed, where the system is gradually cooled to promote convergence to the global minimum (Hammersley, 2013).

Several quantum chemical descriptors can be used to analyze the chemical reactivity of molecules on the surface of a crystal. One very important electronic properties of the molecule is its HOMO and LUMO energy. The energy gap between the HOMO and LUMO for each dye was calculated as (Khnifiraa et al., 2020)

$$\Delta E_{gap} = E_{LUMO} - E_{HOMO} \tag{2.40}$$

Another molecular quantum chemical descriptor that determines the chemical reactivity of dyes on the surface of semiconductor crystals is electronegativity (χ), which is defined as (Cao et al., 2021),

$$\chi = \frac{IE + EA}{2} \tag{2.41}$$

where IE is the ionization energy and EA is the electron affinity. This parameter reflects the tendency of an atom to attract electrons in a bond. The IE is approximated from the E_{HOMO} value as $IE = -E_{HOMO}$, whereas the EA is obtained from the E_{LUMO} value as $EA = -E_{LUMO}$. The global hardness and softness of molecules are significant parameters influencing their stability and reactivity during the adsorption process. The global hardness (η) is defined as

$$\eta = \frac{\Delta E_{gap}}{2} \tag{2.42}$$

The global electrophilicity index serves as a valuable descriptor in predicting the behavior of molecules during adsorption processes, influencing their reactivity and interaction with

surfaces and other species in a chemical environment (Jupp et al., 2018). It is defined as

$$\omega = \frac{\mu^2}{2\eta} \tag{2.43}$$

where μ is the electrochemical potential of the molecule defined as $\mu = -\eta$. According to 2^{nd}-order perturbation theory, the stabilization due to delocalization of an electron pair from the donor orbital (i) to the acceptor orbital (j) is calculated as

$$E(2) = q_i \frac{F(i,j)^2}{(E_j - E_i)} \tag{2.44}$$

where q_i is the donor orbital occupancy, E_i, E_j are diagonal elements (orbital energies) and F(i, j) is the off-diagonal NBO Fock matrix element (Demircioğlu et al., 2015).

The total energy of configuration m is calculated according to the following sum,

$$E_m = E_m^{AA} + E_m^{AS} + U_m^A \tag{2.45}$$

where E_m^{AA} represents the intermolecular energy among the molecules of dyes, E_m^{AS} signifies the interaction energy between the dye molecules and the BiOX surface and where U_m^A indicates the total intramolecular energy of the dye molecules. Importantly, the intramolecular energy of the dye structures was not included in the calculations, as these structures were held constant throughout the simulation. Consequently, this energy contribution remains constant and effectively cancels out since only the differences in energy are significant for the adsorption locator calculations. The total intramolecular energy is calculated as the sum of the intramolecular energies of all adsorbates across all the components:

$$U_A^m = \sum U_{intra} \tag{2.46}$$

where N denotes the set of adsorbate loadings of all the components in configuration m. The adsorption energy is calculated as

$$E_{ads} = E_{sys} - (E_{surf} + E_{dye}) \tag{2.47}$$

where E_{sys} is the total energy of the dye-surface system, E_{surf} is the energy of the clean surface and E_{dye} is the energy of the isolated dye molecule (Carrasco et al., 2013).

2.7 Synthesis Methods of BiOX Nanomaterials

There are two general approaches to synthesize nanomaterials for various applications, that is, top-down and bottom-up (Yi et al., 2023). Mechanical, electrical and thermal forces are used in the top-down approach to crushing bulk materials into microparticles or nanoparticles. Due to the chemical reactions and attractive forces small molecules and atoms are

assembled in bottom-up processes. Specifically, the BBSc photocatalysts can be synthesized through physical, chemical, and biological (green) methods. In contrast to physical synthesis methods, chemical synthesis methods are profoundly dependent upon chemical solvents, while green synthesis methods are characterized by non-toxic chemicals and substrates (Bhat and Sundaram, 2015).

The performance of catalysts depends on various parameters such as morphological characteristics such as particle shape, size, and surface area, electronic structures, catalyst dose, pH and pollutant concentration, and temperature (Kumar and Pandey, 2017). Therefore, synthesis methods may have a significant contribution to enhancing the noninherent parameters of the photocatalytic materials, such as morphology and surface properties. To date, the BiOX photocatalyst has received special research attention in the catalysis field owing to its strong redox reaction capacity (Li et al., 2022). The photocatalytic activity of BiOX photocatalysts mainly depends on their size, morphology, specific surface area and crystalline structure. Over the past two decades, various species of BiOX with different morphology such as nanobelts, nanowires, nanosheets, nanoplates, nanotubes, nanoparticles, nanoflowers, hollow structures, and hierarchical nanostructures have been reported (Meena et al., 2021). Hence, there are several techniques to fabricate nanostructures of BiOX and their nanocomposite for various applications. A few of them are hydrothermal, solvothermal, hydrolysis, precipitation method, two-phase method, ultrasonic/ microwave-assisted method and physical method.

2.7.1 Chemical Precipitation Method

Chemical precipitation is one of the most promising methods to prepare the nano-catalysts. Because it allows the complete precipitation of the metal ions. Furthermore, nanoparticles of higher surface areas are commonly prepared by using this method. In a chemical precipitation method, an alkali solution containing halide sources is slowly dropped into the Bi-containing precursors under continuous stirring and BiOX precipitate is formed. The benefits of this approach include its convenient synthesis, cheapness, and low energy usage. However, its drawbacks include particle aggregation, impurities, and uncontrolled morphology (Dutta et al., 2022). Recently, nanoparticles of BiOCl were synthesized using the co-precipitation method for the photodegradation of methylene blue (Puttaraju et al., 2022).

2.7.2 Solvothermal/Hydrothermal Method

The hydrothermal/solvothermal method is a soft chemical method using different solvents in which pressure is generated to promote chemical reactions, increasing the reactivity and precursors solubility (Bai et al., 2023). The main difference between the two methods are organic solvents used. Thus, in a typical hydrothermal or solvothermal method, the precursors of the Bi source and the halogen source or ionic liquids are dissolved in solvents and transferred into the autoclave. Under a condition of high temperature and high pressure,

various BiOX nanostructures are synthesized. It is the most widely reported method for the synthesis of bismuth based photocatalysts. Hydrothermal synthesis promotes the formation of well-crystallized BBSs photocatalysts and allows for the precise control of the size, shape, and morphology. The high-pressure and high-temperature conditions in hydrothermal reactions lead to the controlled growth of nanoparticles, resulting in improved crystallinity and reduced defects in the material (Wei et al., 2021).

2.7.3 Thermal Decomposition Method

Calcination is a thermal treatment process applied to solid materials to bring about a thermal decomposition, phase transition, or removal of a volatile fraction. Modified BiOX-based photo-catalysts can be produced via heat treatment of pure BiOX materials. Hence, it is a useful method for the production of bismuth-rich bismuth oxyhalide semiconductors as heating removes unstable halogen atoms in the crystal structure. For example, Huang et al. synthesized $Bi_4O_5I_2$, Bi_5O_7I, and $Bi_4O_5I_2$-Bi_5O_7I composites using BiOI as the precursor (Huang et al., 2017).

2.7.4 Green Synthesis Method

In the field of nanomaterials preparation, green synthesis is a rapidly emerging technology. As a reducing and stabilizing agent, plants, bacteria, fungi, and algae are used. As a result, the green method of nanomaterials is an eco-friendly, biocompatible, cheap, and non-toxic method. Recently, a green synthesis method was used to synthesize Z-scheme heterojunction photocatalysts. For example, the Z-scheme heterojunction of CdSe/BiOCl photocatalysts was synthesized through the green synthesis method for organic dye degradation (Shi et al., 2020). Similarly, Li *et al.* used the green synthesis method to prepare heterostructured ternary Cd/CdS/BiOCl photocatalysts for the removal of persistent organic contaminants in wastewater (Li et al., 2015b).

2.8 Characterization Techniques

2.8.1 X-Ray Diffraction

X-ray diffraction (XRD) spectroscopy is used to study crystal structure and size, phase identification, and lattice parameters. The crystal size D_s of the powder will be calculated according to the Dubye Scherrer Eq. 2.48.

$$D_s = \frac{0.9\lambda}{\beta cos\theta} \tag{2.48}$$

Where λ is the x-ray wavelength, β is the peak width of the diffraction line at half of the maximum intensity and θ is the Bragg angle. For a tetragonal structure, the lattice constants are denoted as a and c, where a is the in-plane lattice constant and c is the out-of-plane lattice constant (Stanjek and Häusler, 2004). Thus, from the X-ray diffraction result, the

lattice parameters are determined using Bragg's Law;

$$n\lambda = 2d_{hkl}\sin\theta \tag{2.49}$$

where d_{hkl} is the interplanar spacing, θ is the angle of diffraction, and λ is the wavelength of the X-ray. For a tetragonal system, d_{hkl} for the (hkl) planes can be calculated using Eq. 2.50:

$$\frac{1}{d_{hkl}^2} = \frac{h^2 + k^2}{a^2} + \frac{l^2}{c^2} \tag{2.50}$$

where h, k, and l are Miller indices.

2.8.2 Microscopy Techniques

Microscopy is a vital tool in material science and nanotechnology, allowing researchers to visualize and analyze materials at micro and nanoscale levels. Scanning electron microscopy (SEM) and transmission electron microscopy (TEM) are two widely used techniques to study the morphology, structure and distribution of particles. SEM utilizes a focused beam of electrons that scans the surface of a specimen. As the electron beam interacts with the sample, it generates various signals, including secondary electrons, backscattered electrons, and characteristic X-rays, which are collected to form high-resolution images of the surface topography (Hafner, 2007). SEM can be coupled with Energy Dispersive X-ray Spectroscopy (EDS) to provide elemental analysis, enabling the identification of the composition of materials directly from the images.

TEM involves transmitting a high-energy electron beam through an ultra-thin specimen. As the electrons pass through the material, they interact with its atoms, producing images based on variations in electron density. TEM provides atomic-resolution images and information regarding the internal structure of the material. TEM is particularly useful for analyzing the structure of nanoparticles, revealing details about size, shape, and crystallinity (Zuo and Spence, 2017).

2.8.3 Spectroscopy Techniques

Spectroscopic techniques are essential tools in the characterization of material properties, providing valuable insights into the electronic structure, vibrational modes, and chemical composition of materials. UV-Vis spectroscopy measures the absorption of ultraviolet and visible light by a material, providing information about its electronic transitions. When light of specific wavelengths is incident on a sample, electrons in the ground state can absorb energy and transition to excited states. UV-Vis spectroscopy is commonly employed to determine the band gap of semiconductor materials. By analyzing the edge of the absorption spectrum, one can identify the energy needed for electronic transitions, offering insights into the material's conductivity and optoelectronic properties. The optical band gap of prepared samples is usually evaluated from the UV-Vis spectra. In ultraviolet-visible light (UV-vis)

spectroscopy, light absorption is measured as a function of wavelength. The wavelength (λ) of the absorption edge is converted to energy (E) using the Eq. 2.51:

$$E = \frac{hc}{\lambda} \tag{2.51}$$

where h is Planck's constant (6.626×10^{-34} Js), c is the speed of light (3.00×10^{8} m/s), and λ is the wavelength in meters. The energy band gap of a given material can be precisely calculated using the Tauc method as given in Eq. 2.52.

$$(\alpha h\upsilon)^{1/n} = A(h\upsilon - E_g) \tag{2.52}$$

where α is the absorption coefficient and calculated from the absorbance A using the Beer-Lambert law $A = \alpha \cdot l$ where l is the path length in centimeters. A Tauc plot is generated by plotting $(h\nu)^n$ versus $h\nu$, where $h\nu$ is the photon energy and n depends on the type of transition (1/2 for direct transitions, 2 for indirect transitions) (Andrade et al., 2024).

Photoluminescence (PL) spectroscopy involves the emission of light from a material after it has absorbed photons and transitioned to an excited state. The emitted light is characteristic of the material and can reveal information on electronic and optical properties (Aoki, 2002). Emission peaks in PL spectra often correspond to specific electronic transitions associated with these defects, allowing for the identification and characterization of their impact on material properties.

Fourier Transform Infrared (FTIR) Spectroscopy measures the absorption of infrared radiation by a material, which causes molecular vibrations and rotations. The resulting spectrum provides information on functional groups and molecular interactions within a material. FTIR is widely used to characterize the presence of specific functional groups in organic and inorganic compounds. The absorption bands in an FTIR spectrum correspond to vibrational modes of chemical bonds, allowing for comprehensive chemical analysis (Berthomieu and Hienerwadel, 2009).

2.9 Photocatalytic Application of BiOX

The first applications of BiOX in photocatalysis were reported in the 1990s. Researchers began investigating BiOCl, BiOBr, and BiOI for their ability to degrade organic pollutants under UV light (Li et al., 2014). BiOX materials are actively being researched for their applications in wastewater treatment, air purification, and the production of hydrogen through photocatalytic water splitting. Their effectiveness in degrading dyes and other contaminants underscores their practical utility in environmental remediation (Zulkiflee et al., 2023a).

2.9.1 Organic Pollutants Degradation

The rapid industrialization of the 21^{st} century has resulted in significant environmental challenges, particularly concerning water quality. The introduction of various toxic sub-

stances—synthetic chemicals, heavy metals, fertilizers, and organic dyes has led to widespread water contamination. This pollution not only threatens aquatic ecosystems but also poses serious health risks to humans and terrestrial life (Thakur and Kumar, 2022). Organic dyes are extensively used across industries such as textiles, plastics, and paper production to impart color. These dyes often contain complex synthetic compounds that are resistant to degradation, making them persistent pollutants in aquatic environments. The release of these dyes, along with other organic pollutants like pesticides and pharmaceuticals, from manufacturing and domestic waste, contributes significantly to the degradation of water quality (Arumugam et al., 2021).

The presence of organic pollutants not only disrupts aquatic ecosystems but also compromises the safety of drinking water, impacting public health and biodiversity. One promising approach for addressing water pollution is photocatalytic degradation, which utilizes advanced catalysts to break down organic dyes and other pollutants under light irradiation. This method has gained traction due to its potential for efficient degradation of contaminants without the need for extensive chemical treatments. Recent advancements in photocatalysts, particularly BiOX materials, have shown enhanced charge transfer and separation capabilities, making them effective in facilitating the degradation of organic dyes (Foo et al., 2022; Zhang et al., 2023; Song et al., 2022).

Bismuth oxyhalides (BiOX, where X = Cl, Br, I) are emerging as promising materials for photocatalytic applications due to their unique properties and effectiveness in degrading pollutants and facilitating chemical reactions under light irradiation. BiOX photocatalysts harness light energy to generate reactive species that can oxidize and mineralize complex organic molecules into benign byproducts, thereby contributing to environmental sustainability. Their effectiveness in various pH environments and operational conditions positions them as viable candidates for industrial wastewater treatment applications (Bhat and Sundaram, 2015; Baaloudj et al., 2022). The basic photocatalysis mechanisms involve photon absorption, charge separation, and redox reaction. When BiOX is exposed to light, it absorbs photons, which excites electrons from the valence band to the conduction band, creating electron-hole pairs. The unique layered structure of BiOX facilitates the separation of these charge carriers. The internal electric field generated by the layered structure helps prevent the recombination of electrons and holes, which is critical for maintaining high photocatalytic activity. The photogenerated electrons migrate to the catalyst surface, where they participate in reduction reactions, while holes engage in oxidation reactions with water molecules.

2.9.2 Hydrogen Production

Developing hydrogen energy has increasingly come to the forefront as it is a clean, safe, and sustainable source of energy. Recently, BiOX has gained considerable attention as a photocatalyst for generating hydrogen through water splitting (Liao et al., 2022). This process is crucial for developing sustainable energy sources, and BiOX materials offer unique ad-

vantages due to their structural and electronic properties. Lee et al. synthesized hierarchical BiOX (X = Cl, Br, I) microspheres using a microwave-assisted solvothermal method with bismuth(III) nitrate pentahydrate as the precursor, employing ethylene glycol and ethanol as solvents. The resulting photocatalysts were evaluated for their photocatalytic hydrogen evolution capabilities via water splitting under visible light irradiation. Among the synthesized BiOX materials, BiOI exhibited the highest hydrogen production rate, achieving 1316.9 μmol $h^{-1}g^{-1}$ over 360 minutes (Lee et al., 2018). This superior performance can be attributed to several key factors: (I) BiOI demonstrated the lowest PL intensity among the BiOX series, which indicates a more effective separation of photogenerated charge carriers (electrons and holes). Enhanced charge separation is critical for minimizing recombination losses, thereby improving photocatalytic efficiency. (II) BiOI possesses a sufficiently high overpotential at its conduction band, facilitating the reduction of protons (H^+) to molecular hydrogen (H_2). This characteristic is essential for achieving an efficient conversion during the photocatalytic reaction.

2.9.3 Carbon Dioxide Reduction

BiOX are emerging as promising photocatalysts for the reduction of carbon dioxide (CO_2) into useful fuels and chemicals. This process is crucial for mitigating climate change and developing sustainable energy sources. The unique layered structure of BiOX facilitates efficient charge separation and migration. The electrons can migrate to the surface to participate in reduction reactions, while holes can contribute to oxidation processes. The adsorbed CO_2 molecules on the surface of BiOX are activated through interactions with photogenerated electrons and holes, leading to various reduction products. CO_2 can be reduced to CO through a one-electron transfer process. Further reduction can lead to the formation of hydrocarbons like methane (CH_4) through multiple electron transfer steps. Intermediate species can also be converted into alcohols like methanol (CH_3OH), which are valuable as fuel (Ren et al., 2020). The photoelectrocatalytic reduction of CO_2 using bismuth oxyhalides (BiOX, where X = Cl, Br, I) was investigated through a combination of physicochemical and photoelectrochemical analyses. The results from the photoelectrochemical measurements demonstrate that all BiOI-metal composites are effective materials for CO_2 reduction in neutral media (Mora-Hernandez et al., 2023).

3

MATERIALS AND METHODS

3.1 Computational Methods

3.1.1 Packages and software

In this dissertation, a variety of computational packages and software tools were employed for numerical calculations, data visualization, and graphical plotting. For computational calculations, the QUANTUM ESPRESSO package, Materials Studio, and Gaussian 09 package were utilized. The name "ESPRESSO" stands for "opEn-Source Package for Research in Electronic Structure, Simulation, and Optimization". For visualization and plotting of results, several software applications were implemented, including Visualization for Electronic and STructural Analaysis (VESTA), phonopy (X-window) Crystalline Structures and Densities (XCrysDen), and XMGrace, along with Origin Pro 2018, Match for diffraction analysis and ImageJ.

3.1.2 Electronic, Optical, Vibrational and Thermodynamics properties calculation

For this dissertation work, the crystallographic information file (CIF) of the BiOX was obtained from the Materials Project database. The computational investigation followed a systematic approach to optimize the crystal structure and analyze its properties. The geometry was optimized using the GGA method and the Perdew-Burke-Ernzerhof (PBE) exchange-correlation functional. To achieve acceptable convergence, the force acting on the atoms was set at less than 0.03 eV, the maximum stress was set at less than 0.05 Gpa, the maximum displacement of the atom was set at less than 0.001 Å, and the energy modifications per atom were set at less than 10^{-5} eV.

Following structure optimization, a non-self-consistent (non-SCF) calculation was performed on a denser k-point mesh grid to analyze the electronic properties. The band structures were computed along the special lines connecting the following high-symmetry points Γ-X-M-Γ-Z-R-A-Z|X-R|M-A where Γ(0, 0, 0), X (0, 0.5 0), M (0.5, 0.5, 0), Z (0, 0, 0.5), R (0, 0.5, 0.5), and A (0.5, 0.5, 0.5) are the coordinates of a crystal in the k-space. The energy

band gap of BiOX was calculated using GGA and HSE methods. The density of states (DOS) was calculated using a denser k-point grid than that used for the SCF calculation. The tetrahedron method was employed, wherein the Brillouin zone was divided into non-overlapping tetrahedra. The integrated quantity was computed using linear interpolation of energy for each tetrahedron, yielding a comprehensive DOS profile. To evaluate the contributions of specific atoms or orbitals to the total density of states, the partial density of states (PDOS) was computed. This analysis provides insights into the electronic structure, demonstrating how particular atomic characteristics influence the overall electronic properties of BiOX.

The optical properties were calculated using norm conservation pseudo potential with linear response methods, which relate the dielectric function to the electronic polarizability. Other optical properties of the BiOX were calculated via the equations discussed in section 2.2.2. The response of the electric field of BiOX in the infrared region was investigated through the calculation of infrared (IR) and Raman spectra. The IR and Raman spectra were calculated at the gamma point and the system was configured to operate as a crystal structure, with the option for Raman intensity calculations enabled. Additionally, the electronic minimization was set to all bands of electronic density functional theory (EDFT) to enhance computational efficiency. Similarly, we used the GGA approximation with norm-conserving pseudopotentials to calculate the phonon frequency of the BiOX crystal. The phonon frequencies are computed based on a plane wave basis set on a 6 × 6 × 6 mesh grid with a cutoff energy of 750 eV. The phonon calculations were configured to compute both phonon dispersion and density of states utilizing the linear response method. Interpolation was performed on a q-vector grid with a spacing of 0.05 1/Å, and a convergence tolerance of 1 X 10^{-5} eV/Å^2 was applied to ensure the accuracy of the results. The phonon frequencies were estimated by sloping the dynamic matrix, which was built from the force constant array acquired by the linear response method. The heat capacity and other thermodynamic properties were computed at constant volume as a function of temperature utilizing the quantified wave spectrum.

To consider the effect of doping concentration, a supercell of 2 x 2 x 1, and 4 x 2 x 1 were constructed using phonopy software. A convergence tolerance per atom of total energy of 1 x 10^{-4} eV and a high-energy convergence tolerance of 1 $\times$ 10^{-6} eV was used. Here we considered a model of $Sn_xBi_{1-x}OBr_xCl_{1-x}$, where x represents the replacement of 1, 2, or 3 Sn/Br atoms for every host atom in the supercell of BiOCl, which represents the concentration of 0.0625, 0.125, and 0.25, respectively. We calculated the band structures, DOS, PDOS, JDOS, and optical properties using the optimized structure. To investigate the effects of doping and co-doping of post-transition metals on the electronic and optical properties, BiOCl has been selected from the BiOX family due to its promising characteristics and applications in photocatalysis. BiOCl has a wide band gap of approximately 3.0 to 3.5 eV, which limits its photocatalytic activity mainly to ultraviolet (UV) light. This wide band gap is beneficial because it enables BiOCl to absorb a significant amount of UV radiation, which

is abundant in sunlight, thereby facilitating efficient photocatalytic reactions under UV illumination. Although BiOCl's absorption in the visible spectrum is limited, modifications such as doping and co-doping can enhance its light absorption capabilities, making it more effective for photocatalytic applications.

3.1.3 Molecular Interaction and Adsorption Calculation

The chemical structures of the MB, MO, and MR dyes were optimized using the B3LYP / 6-311G base set implemented in the Gaussian 09 software. The electronic properties of these structures were analyzed through NAO and NBO analysis. To explore the chemical reactivity and kinetic stability of the molecules, various quantum chemical descriptors, such as absolute electronegativity (χ), global hardness (η), softness (S), chemical potential(μ) and electrophilicity index (ω), were analyzed. These descriptors are obtained from calculations of the HOMO and LUMO energy values. The effects of the solvent were examined by computing the conductor-like screening model (COSMO) sigma profile for each dye via the DMol3 module within the Material Studio software.

The molecular Quantum Theory of Atoms in Molecules (QTAIM) and Non-Covalent Interaction (NCI) calculations were conducted as follows: The wavefunction was generated from the optimized electronic structure of each dye using Gaussian 09W software. The electron density was derived from the wavefunction generated. Then a point-by-point topological analysis was performed on the electron density to identify critical points and bond paths. This analysis was conducted using the Multiwfn software version 3.8, and the results were visualized with visual molecular dynamics (VMD) software.

MCDS methodology was utilized to identify the most stable and lowest-energy adsorption sites and investigate the preferential adsorption behavior of different dyes (MB, MO and MR) on the 001 facet of BiOCl crystals in an aqueous environment. This approach employs the adsorption locator code integrated within the Materials Studio software. Initially, a slap of 001 facets of a BiOCl crystal with a vacuum layer of 30 Å was built and then expanded to create a (6 x 6 x 1) supercell. A dye, water and BiOCl system was subsequently developed for MCDS calculations. Throughout the simulation, the universal force field (UFF) was applied to optimize the geometries of all the components within the system under investigation. Furthermore, each adsorption configuration included 100 H_2O molecules to simulate the effects of the solvent accurately.

3.2 Experimental Methods

3.2.1 Chemicals and Reagents

The precursors salt and reagents used to synthesize pure and Sn-doped BiOCl nanoparticles are bismuth nitrate pentahydrate ($Bi(NO_3)_3.5H_2O$), 99%, analytical grade), Quangdang Quanghua sci-Tech, China, deionized water, potassium chloride (KCl) 99 % Loba Chemie

PVT. Ltd, stannous chloride dihydrate ($SnCl_2.2H_2O$) 97 % Sisco research laboratory PVT. Ltd, India, sodium hydroxide (NaOH) and ethanol.

3.2.2 Synthesis of BiOCl and Sn-BiOCl Nanosheets

Pure BiOCl nanosheets were synthesized via a co-precipitation method according to method developed by (Puttaraju et al., 2022). Initially, 0.1 M of ($Bi(NO_3)_3.5H_2O$) was dissolved in 100 mL of a 1:1 (v/v) mixture of ethanol and distilled water. The solution was subjected to continuous stirring for 20 minutes. Subsequently, 5 mL of a 2 mmol KCl solution was added to the stirring mixture, which was maintained at room temperature for an additional 60 minutes. Following the formation of a white precipitate, the product was washed several times with ethanol and distilled water to eliminate impurities. The resulting sample was then filtered using Whatman filter paper and dried at 80 °C for 6 hours.

Sn-doped BiOCl nanosheets with doping concentrations of 1%, 3%, and 5% were also synthesized through the co-precipitation method. For this synthesis, 4.81 grams of ($Bi(NO_3)_3.5H_2O$) was dissolved in 50 mL of a 1:1 (v/v) mixture of ethanol and distilled water, labeled as Solution A (Sol-A). In a separate container, 0.15 grams of potassium chloride (KCl) was dissolved in 30 mL of the same solvent mixture, designated as Solution B (Sol-B). Additionally, 0.04 grams of ($SnCl_2.2H_2O$) was dissolved in 15 mL of the solvent mixture, referred to as Solution C (Sol-C). Solution B was gradually introduced into Sol-A under magnetic stirring at a controlled rate. Following this, 5 mL of NaOH was added slowly to the amalgamated Sol-A and Sol-B. After stirring for 60 minutes, Sol-C was added dropwise into the mixture, which was then stirred for an additional 3 hours. The resultant precipitate was subjected to several washes with ethanol and deionized water to remove residual contaminants. Finally, the product was filtered and dried at 80 °C for 6 hours.

4

RESULTS AND DISCUSSION

4.1 Computational Characterization of Pristine Bismuth Oxyhalides

4.1.1 Crystal structure

Figure 4.1 shows a crystal structure of BiOX crystal. The crystal structure of BiOX is characterized by interlocking $[Bi_2O_2]$ blocks and double halogen slabs, resulting in a two-dimensional arrangement. Within this structure, bismuth-oxygen (Bi-O) and bismuth-halogen (Bi-X) bonds are established through strong covalent interactions, while the halogen atoms (X-X) are connected via weaker van der Waals forces. BiOX compounds typically exhibit a layered architecture, wherein bismuth and oxygen atoms form a continuous network, with halide atoms (such as F, Cl, Br, or I) occupying interstitial sites between these layers. The optimized crystal structure of BiOX is identified as a tetragonal matlockite structure, classified under space group 129 (P4/nmm, P 4ab 2ab-1ab) and point group 15 (D4h, 4/mmm, 4/m 2/m 2/m). The calculated lattice parameters for the unit cell of each BiOX crystal are presented in Table 4.1. The result suggests that the current work presents reliable band gap and lattice parameter values for the studied BiOX compounds. The results show significant alignment with both previous reports Huang et al. (2020), indicating the effectiveness of the computational methods employed. This investigation contributes critical knowledge to the understanding of the electronic and structural properties of bismuth oxyhalides, which is essential for their potential applications in photocatalysis and other technological domains.

4.1.2 Electronic band structure and Density of states

Band gap is a crucial parameter in studying the optical properties of semiconductor materials. In this work, the electronic band structures of BiOX crystal species were calculated. In the BZ, the band structure demonstrates how the electronic energies depend on the k-vector along with high symmetry points. The electronic band structure of BiOX crystal is plotted in Fig. 4.2. From the electronic band structure, the locations of the maximum valence band (MVB) and the minimum conduction band (MCB) for BiOX are located at different

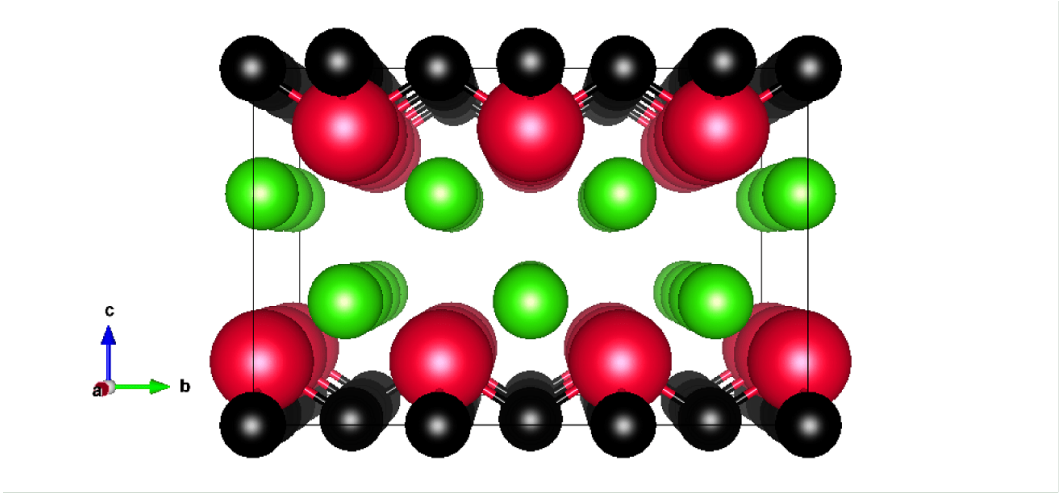

Figure 4.1: Crystal structure of BiOX crystals, where red color is the bismuth atom, green color is halogen atoms (F, Cl, Br or I) and black is the oxygen atom.

Table 4.1: Electronic band gap energies and lattice parameters of BiOX

Crystal	Energy Band Gap (eV)				Optimized Lattice Parameters					
	Current Work		Literature *		Current		Literature			
	PBE	HSE06	PBE, HSE06	Exp.	Compt. a(Å)	Compt. c(Å)	Comp. a(Å)	Comp. c(Å)	Exp.** a(Å)	Exp.** c(Å)
BiOF	3.36	3.43	3.34, 4.18	3.2-3.6	3.99	5.75	3.72	6.2	-	-
BiOCl	2.9	3.29	2.92, 3.37	2.9-3.4	3.87	8.01	3.87	7.42	3.88	7.35
BiOBr	2.37	3.05	2.65, 2.82	2.3-2.92	3.91	9.01	3.9	8.14	3.91	8.08
BiOI	1.58	2.19	1.75, 2.00	1.8-2.1	3.99	9.89	3.98	9.15	3.98	9.13

$*$ (Huang and Zhu, 2008; Huizhong et al., 2008), $**$ (Zhao et al., 2012)

high symmetry k-points, indicating that all BiOX crystal's exhibit indirect band gaps. This finding is consistent with literature report (Huang and Zhu, 2008).

The energy band gap for the BiOX (X= F, Cl, Br, or I) system was estimated using PBE and HSE06 exchange-correlation functionals. The band gap calculated by PBE is 1.58 eV, 2.37 eV, 2.90 eV, and 3.36 eV for BiOI, BiOBr, BiOCl, and BiOF respectively. This result is below the experimental results due to the approximation used by PBE functional. However, the energy band gaps using HSE06 functional are 2.19 eV, 3.05 eV, 3.29 eV, and 3.43 eV, for BiOI, BiOBr, BiOCl, and BiOF respectively. The result obtained from HSE06 functional is in good agreement with previously reported experimental data as listed in Table 4.1. According to the previous report (Barhoumi and Said, 2021) and current calculation result, the HSE functional is the best pseudo-potential for determining the electronic band structure of a periodic crystal. From both functional, the calculated energy band gap decreases as the atomic number of the halogen atoms increases from F to I. Because the band gap of materials is influenced by their atomic structure and the nature of the bonds between atoms. As the halogen atoms change from fluorine to iodine, the electronegativity and the size of halogen atoms change. Fluorine being the smallest and most electronegative, leads to a stronger

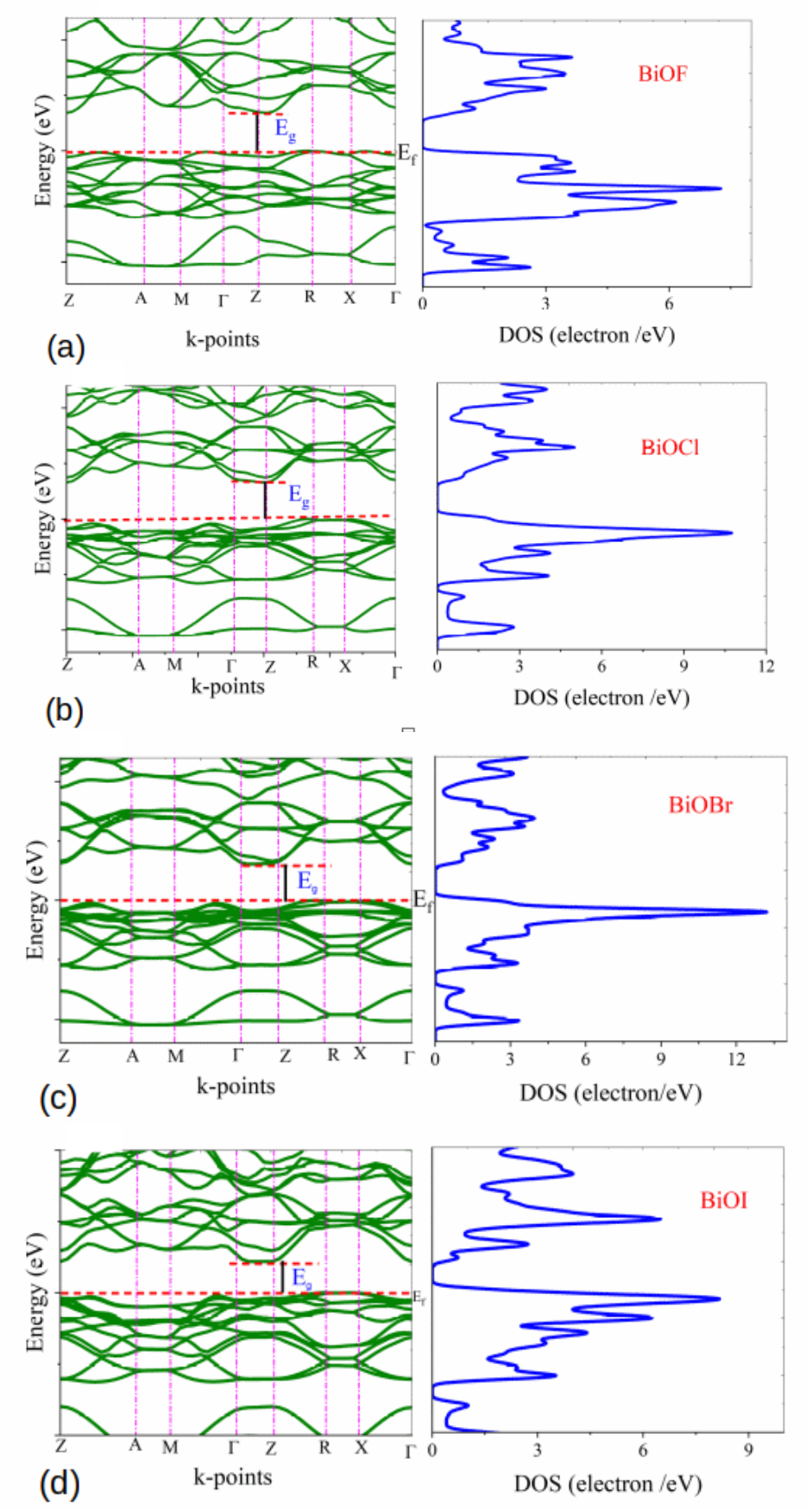

Figure 4.2: The electronic band structures and DOS of (a) BiOF, (b) BiOCl, (c) BiOBr and (d) BiOI crystals.

interaction with bismuth, resulting in a wider band gap compared to other BiOX families. Furthermore, as we move from I to F in the halogen series, the atomic radii decrease and the electron affinity increases. This can affect the overlap of atomic orbitals and energy levels of the electrons, thus altering the band gap.

The energy band gap and the configuration of band edges play a pivotal role in the efficiency of photocatalytic applications. Additionally, the lifetime of excited electrons is crucial for facilitating redox processes inherent in photocatalysis (Hazaraimi et al., 2022). Indirect band gap semiconductors are particularly advantageous for photocatalytic applications due to their ability to prolong the lifespan of photogenerated charge carriers. This is because these carriers traverse a finite k-space distance before transitioning to the conduction band (CB). The presence of photogenerated charge carriers is associated with considerable redox potential, which is contingent upon the position of the valence band edge in the photocatalyst (Han et al., 2016). A higher valence band position correlates with enhanced photocatalytic oxidation capabilities. Consequently, the upward shift of the conduction band minimum (CBM) leads to an increased generation of electrons that can react with oxygen molecules adsorbed on the material's surface (Wu et al., 2022).

To better understand the types of orbital mixing in the chemical bonds of BiOX crystal structure, the projected density of states (PDOS) of each BiOX species was analyzed. Figure 4.3 shows the PDOS of the BiOX species. According to the previous report (Wang et al., 2013) and current analysis of PDOS results, the VBM of the BiOX crystal consists mainly of the O 2p and halide X np states (n = 2, 3, 4, and 5 for X = F, Cl, Br, and I, respectively), and the Bi 6p states dominate the CBM. It is conceivable for an electron to transition from the valence band of O (2p) into the empty conduction band of Bi (6p) in the initial optical interband transition, which progressively transforms into a transition from mixed valence states of X (np) and O (2p), moving from Cl to I (Attri et al., 2023; Barhoumi and Said, 2021). Due to the delocalized nature of the plane wave basis set, to understand the location of the electron in the crystal, i.e. the interatomic bonding behavior, population analyses were performed using the Mulliken formalism (Mulliken, 1955). The net charges of Bi are +0.97e, +1.31e, +1.38e, and +1.57e, in the BiOI, BiOBr, BiOCl, and BiOF crystals; respectively.

Hirschfeld charge analysis of BiOX compounds (X = F, Cl, Br, I) reveals a systematic trend in the charge distribution around the bismuth (Bi) atom as shown in Fig. 4.4. The calculated atomic and charge Mulliken population analysis of BiOF, BiOCl, BiOBr, and BiOI crystals are summarized in Table 4.2. The calculated Hirschfeld charges for Bi in BiOI, BiOBr, BiOCl, and BiOF are +0.47e, +0.52e, +0.55e, and +0.62e, respectively. These positive values indicate that the Bi atom has a partial positive charge, suggesting electron depletion relative to its isolated state. The magnitude of the Hirschfeld charge provides insights into the degree of covalence in the Bi-X bond. A larger positive charge on Bi indicates a greater deviation from a purely ionic bond, implying a stronger covalent character. This observation is consistent with previous reports and the computed density of states (DOS)

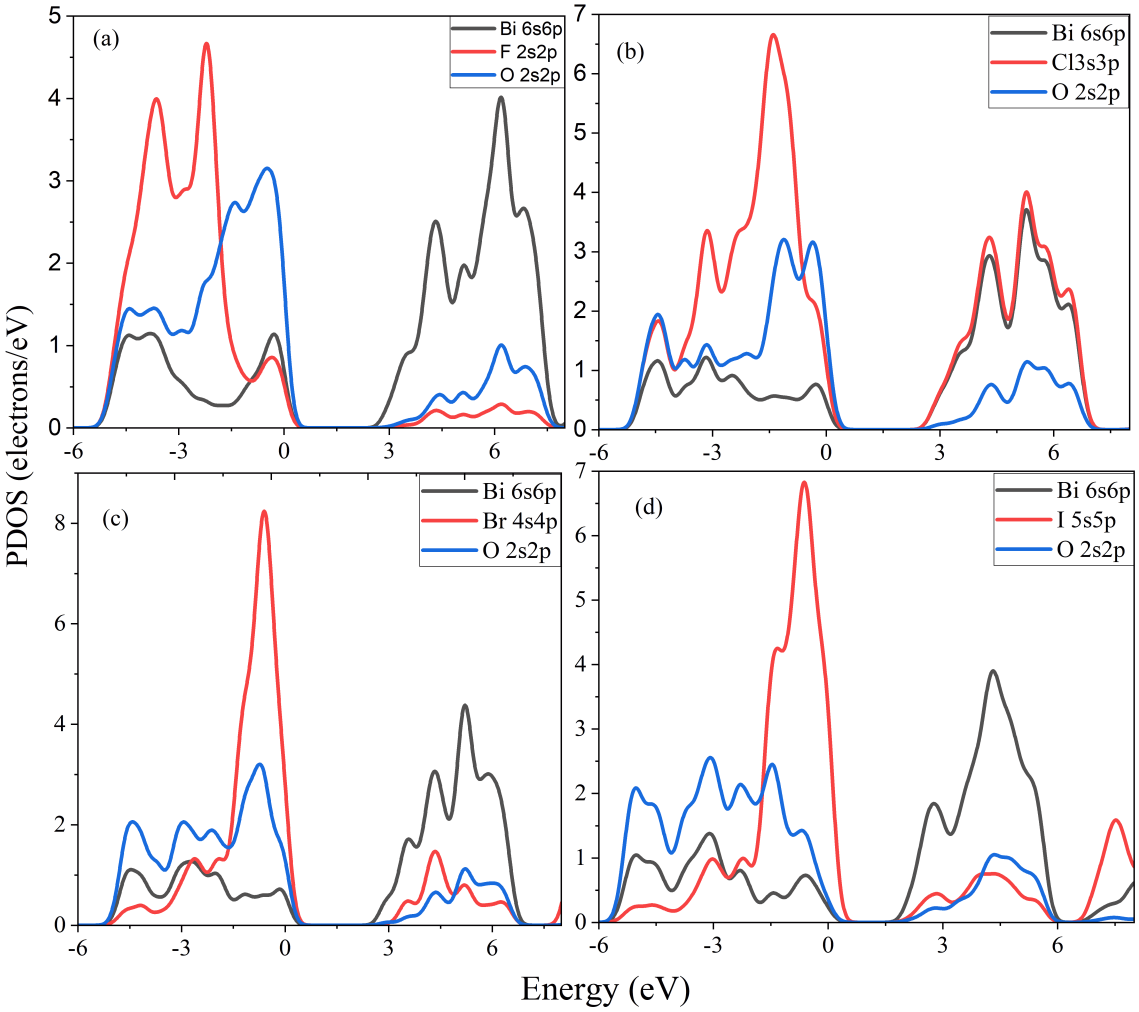

Figure 4.3: The projected density of the state of (a) BiOF, (b) BiOCl, (c) BiOBr, and (d) BiOI crystals.

results, highlighting the stronger and more durable nature of the Bi-O bond compared to the Bi-X bond. The trend in Hirschfeld charges is directly related to the electronegativity of the halogen atom (X). Electronegativity decreases as we move down the halogen group from F to I. This decrease in electronegativity reduces the polarity of the Bi-X bond, resulting in a more electron-rich Bi atom and a less electron-rich halogen atom. Consequently, the charge density shifts towards the Bi atom as we progress from BiOF to BiOI. The significant difference in hybridization ranges between Bi and I, as observed in the DOS results, further supports the stronger covalent character of the Bi-X bond. This difference in hybridization suggests a more substantial overlap of atomic orbitals, contributing to the enhanced covalent bonding strength.

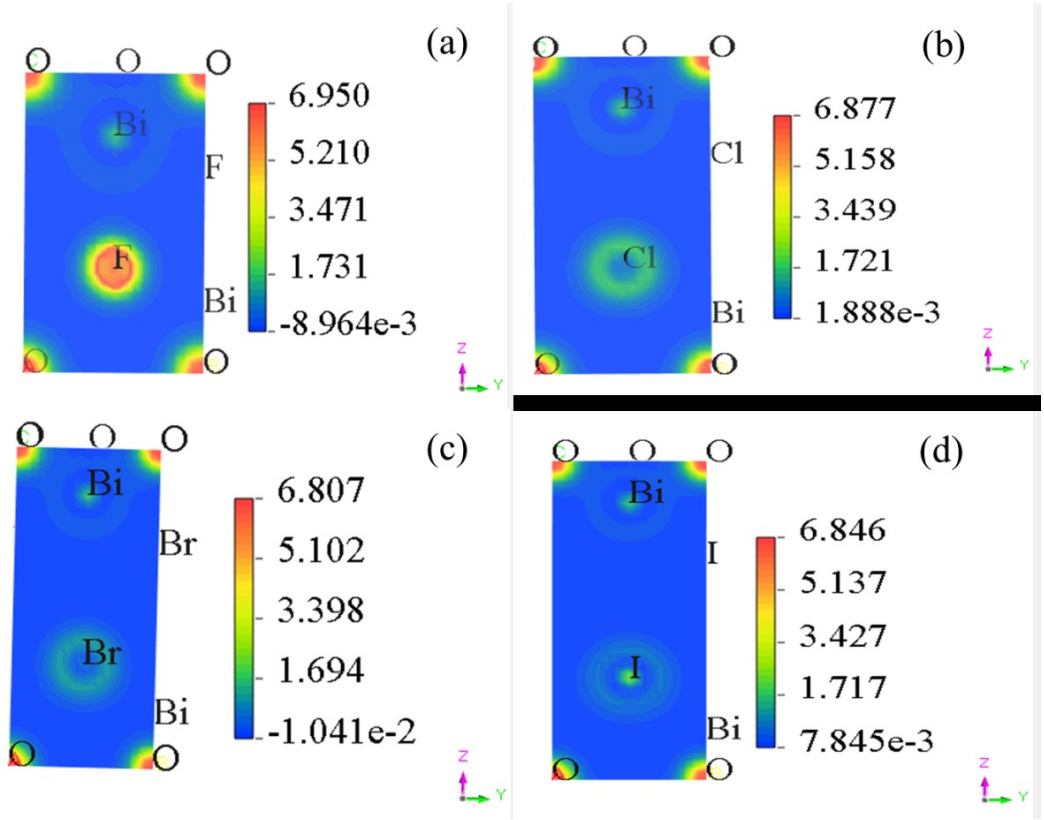

Figure 4.4: The charge density plot for (a) BiOF, (b) BiOCl, (c) BiOBr and (d) BiOI crystal.

Table 4.2: Calculated atomic and charge Mulliken population analysis of BiOF, BiOCl, BiOBr, and BiOI crystals.

Species	s	p	d	f	Total	Charge(e)	Hirschfield Charge (e)
O	1.92	5.00	0.00	0.00	6.92	-0.92	-0.35
F	1.97	5.67	0.00	0.00	7.65	-0.65	-0.27
Bi	1.96	1.47	0.00	0.00	3.43	1.57	0.62
O	1.93	4.94	0.00	0.00	6.86	-0.86	-0.34
Cl	1.96	5.55	0.00	0.00	7.52	-0.52	-0.21
Bi	1.96	1.66	0.00	0.00	3.62	1.38	0.55
O	1.92	4.94	0.00	0.00	6.86	-0.86	-0.86
Br	1.95	5.47	0.00	0.00	7.42	-0.42	-0.18
Bi	1.99	1.70	0.00	0.00	3.69	1.31	0.52
O	1.91	4.66	0.00	0.00	6.56	-0.56	-0.36
I	1.95	5.45	0.00	0.00	7.40	-0.40	-0.11
Bi	1.97	2.06	0.00	0.00	4.03	0.97	0.47

4.1.3 Optical properties

The optical properties of BiOX crystal species were analyzed considering the electronic transitions within the crystal. When an electron within the crystal interacts with an electromagnetic wave, it leads to the excitation of electrons from the ground state to higher energy

states. The complex dielectric functions provide a description of the process through which an electron moves between these different energy states.

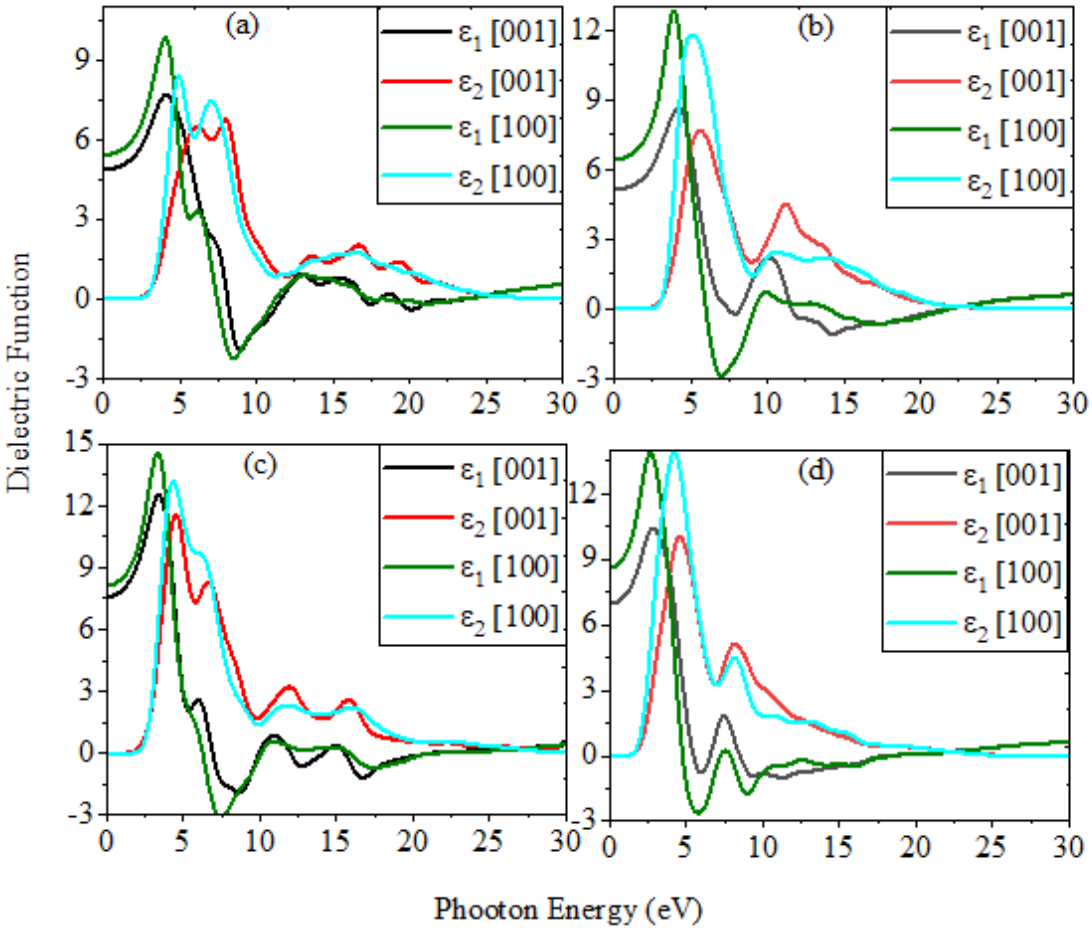

Figure 4.5: The real and imaginary dielectric function for (a) BiOF, (b) BiOCl, (c) BiOBr, and (d) BiOI crystal.

Due to the anisotropy property of the BiOX crystal structure, the real and imaginary parts of the dielectric constants were calculated along different polarization directions. The polarization directions considered in this work were [100] and [001]. For the crystal structure of BiOX, the imaginary and real parts of the dielectric function were calculated in an energy range of 0-30 eV, as plotted in Fig. 4.5. It can be seen that there are two peaks for both the imaginary and real spectra curves of all three crystals. The intensity of the main peaks along the [001] polarization direction is lower than along the [100] polarization direction. The main peaks for BiOF, BiOCl, BiOBr, and BiOI in the real spectra are at 4.04, 3.75, 3.33, and 2.82 eV along the polarization direction [001]. It occurs at photon energies of 8.07 eV, 5.76 eV, 4.54 eV, and 4.21 eV for the imaginary parts, respectively. However, in real spectra, the main peak along the [100] polarization direction appears for BiOF, BiOCl, BiOBr, and BiOI at 4.04 eV, 3.94 eV, 3.33 eV, and 2.62 eV, respectively. For imaginary spectra, the main peaks appear at 4.84 eV, 5.16 eV, 4.24 eV, and 4.14 eV for BiOF, BiOCl,

BiOBr, and BiOBr, respectively. The intense peaks in the real spectrum of each BiOX crystal species are caused by the optical transition between the Cl and O p-state in the highest VB and the Bi p-state in the lowest CB. However, the intense peak for the imaginary part indicates an electron transition between the X-np states in the VB and Bi 6p states in the lower CB. The spectra curve then decreases from the main peaks to the lowest points. After that, it gradually increases until the local peaks, and then gradually drops, suggesting that the gradual appearance of X-nanosecond states in the upper VB and lower CB affects electron transition efficiency to some extent.

As depicted in Fig. 4.6, the strong absorption of the edge of BiOF, BiOCl, BiOBr, and BiOI crystals was estimated to be 320 nm, 367 nm, 449 nm, and 540 nm respectively. The absorption edges of BiOF and BiOCl are in the UV spectra region. This result agrees with the experimental and theoretical studies (Huizhong et al., 2008; Castillo-Cabrera et al., 2022). The peak absorption edge of BiOBr and BiOI is in the visible spectra region. Additionally, different BiOX species exhibit different absorption edges, and their absorption edge red shifts with increasing X atomic number.

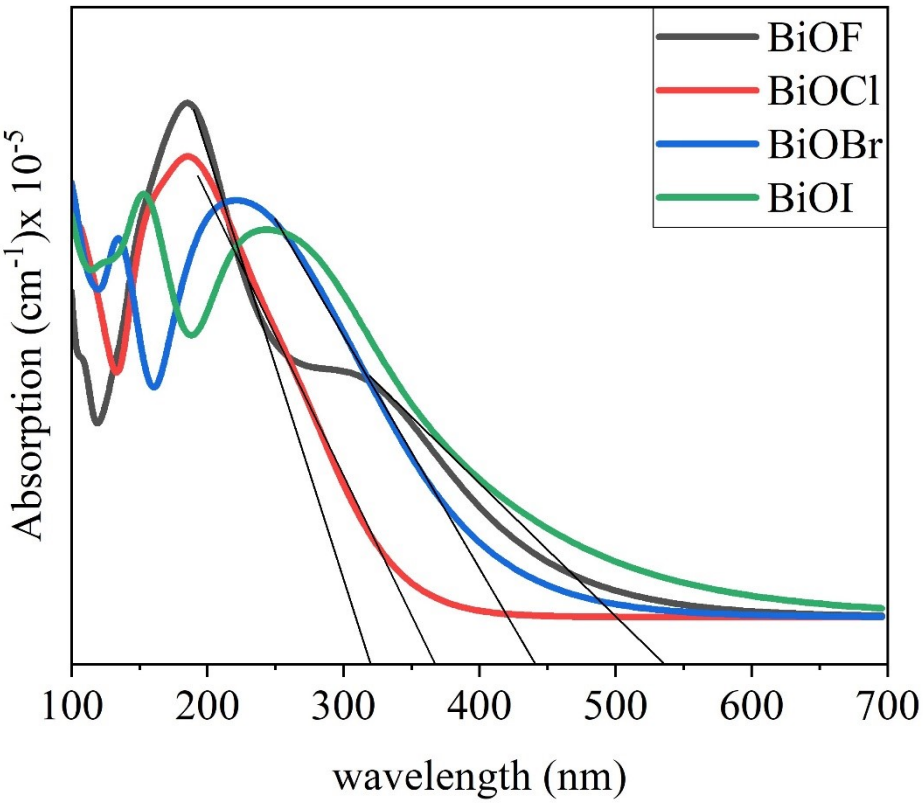

Figure 4.6: Absorption spectrum of BiOX crystal calculated from DFT simulation.

Table 4.3 shows the calculated optical properties of BiOX crystals in different polarization directions. The static dielectric constant is an important parameter that affects how

Table 4.3: Calculated optical properties of BiOX along different polarization directions

Crystals	Polarization Directions	Static dielectric constant	Refractive index	Reflectivity
BiOF	100	5.41	2.31	0.16
	001	4.86	2.19	0.14
BiOCl	100	6.50	2.55	0.19
	001	5.30	2.30	0.15
BiOBr	100	7.06	2.66	0.20
	001	5.66	2.38	0.17
BiOI	100	8.51	2.92	0.24
	001	6.74	2.60	0.20

materials respond to electric fields and thus their photocatalytic efficiency. Higher dielectric constants generally indicate better charge separation and stability, which are critical for photocatalytic processes. The static dielectric constant along all polarization directions increases as the atomic mass of halogen atoms increases from F to I. BiOI displays the highest static dielectric constant of 8.51 in the 100 and 010 directions and 6.74 in the 001 direction, indicating potentially superior charge separation capabilities crucial for photocatalytic applications. The refractive index provides insight into how light propagates through a material, which impacts its optical absorption and photocatalytic efficacy. The refractive index analysis shows that BiOI crystal has the highest refractive index of 2.92 for the 100 directions and 2.60 for the 001 direction, which could enhance interactions between light and the photocatalyst, improving photoabsorption and efficacy in photocatalytic applications. Furthermore, we have also analyzed the reflectivity of BiOX crystals. Lower reflectivity values are preferable as they signify more light being absorbed for photocatalytic reactions. Hence, the calculated result confirms all BiOX crystals have lower reflectivity with slightly larger BiOI crystals. Therefore, the analysis suggests that BiOI demonstrates the most promising optical properties for photocatalytic applications due to its high static dielectric constant and refractive index, which correlate with improved light interaction and charge separation capabilities.

4.1.4 Raman and IR spectra

Raman spectroscopy involves the scattering of light caused by the interaction with vibrational modes (phonons) in a material. BiOX crystals typically display characteristic Raman and IR spectra, which provide valuable information about their crystal structure and phonon modes. BiOX crystals possess several Raman-active vibrations arising from the displacements of atoms within their crystal lattice. These modes can include vibrations of Bi-O bonds, stretching or bending modes of oxygen, and lattice vibrations. The Raman-active modes can vary depending on the specific BiOX composition (X = halogen) and crystal structure. The positions and intensities of IR absorption peaks can be used to identify specific functional groups and confirm the crystal structure of BiOX crystal. Figure 4.8 (a, b)

illustrates the Raman and IR spectrum of BiOX crystals. BiOX is a tetragonal crystalline material with a space group of P4/nmm and a point group of 15, D4h. A tetragonal crystal of BiOX can be described by the vibrational modes $2A_{1g}$ + B_{1g} + $3E_g$ + $2E_u$ + $2A_{2u}$ computed by the analysis of its eigenvectors in group theory (Ferrer et al., 2018; Yu et al., 2007). The modes A_{1g}, B_{1g} and E_g and others represent different types of vibrations. Where A_{1g} is symmetric stretching modes, B_{1g} is antisymmetric bending modes, E_g is degenerate modes involving in-plane vibrations and E_u and A_{2u} are represents out-of-plane vibrations. The vibration mode with subscript g is Raman active mode and the vibration with u subscript is IR active mode. The Raman spectra of the BiOX species consist of strong peaks and weak peaks scattered band. The strong peaks are located at 80.32, 101.61, 132, and 167.16 cm^{-1} for BiOI, BiOBr, BiOCl and BiOF respectively. BiOI, BiOBr, and BiOCl crystals had Rama scattered bands of 87, 109.9, and 142 $cm^{-}1$, respectively. Based on the vibrational mode position, the calculated Raman spectrum matches the experimental results (Dutta et al., 2018; Sajjad et al., 2020). Thus, from the previous reports and our analysis results, the strong scattered band were due to the first order scattering of A_{1g} modes of Bi atoms for BiOX (X= I, Bi or Cl), and B1g modes for BiOF crystals. Moreover, the peaks at 42.53, 350.19, 395; 51.92, 162.27, 365; 60.56, 190, 385, 457; 60.56, 190, 385, 457, and 133, 338.95, 397 cm^{-1} for BiOI, BiOBr, BiOCl, and BiOF are corresponding to A1g external Bi-X stretching mode, Eg internal Bi-X stretching mode, and A_{2u}, produced by the motion of oxygen atoms (Dutta et al., 2018). As a result, there are very weak bands produced at 395, 365, 385, and 397 $cm-1$ for BiOI, BiOBr, BiOCl and BiOF, respectively, which cross-correspond to the modes A_{2u}. The presence of sharp scattering peaks indicates the crystallization of BiOX species. The theoretical calculations can provide insights into the temperature-dependent behavior of Raman-active modes in BiOX crystals. The intensity of the Raman spectrum for BiOX crystals was investigated at different temperatures. Figure 4.7(a–d) illustrates the effect of temperature on the intensity of the Raman spectrum for the BiOX crystal. As the temperature increases, the intensity of the Raman spectrum peak increases due to the increase in the polarizability of electrons in the crystal. This is because, the crystals undergo thermal expansion, leading to changes in the lattice parameters. This thermal expansion affects the phonon energies and alters the Raman scattering process. As a result, the Raman intensity may change with temperature due to modifications in the phonon modes' frequencies and their associated scattering strengths. Anharmonicity in the lattice vibrations becomes more pronounced at high temperatures. Anharmonic effects can lead to changes in the phonon energies and Raman scattering strength. Furthermore, BiOX crystals exhibit phase transitions with temperature changes. These transitions may occur due to alterations in the crystal structure, symmetry, or atomic arrangements.

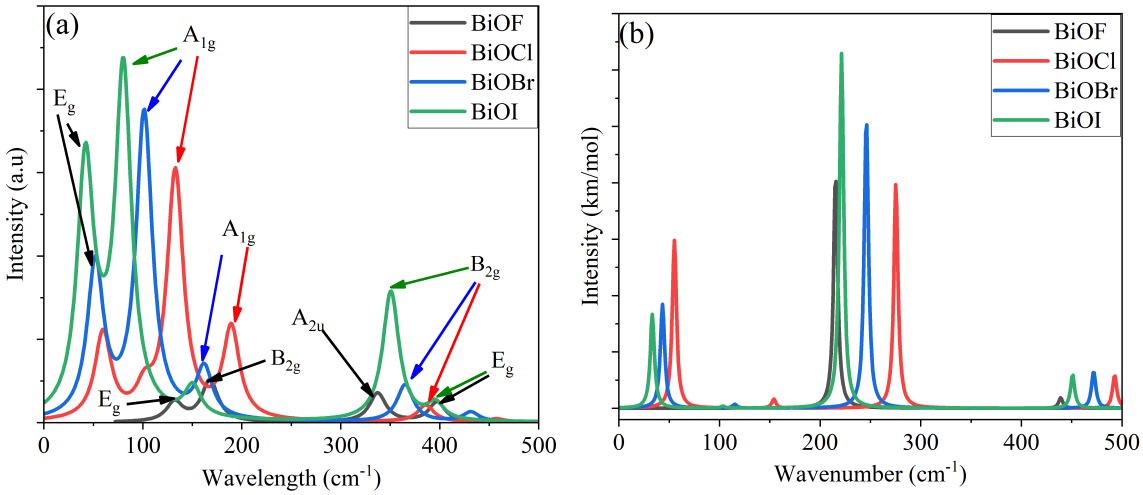

Figure 4.7: (a) Raman Spectrum and (b) IR spectrum of BiOX calculated by the GGA method.

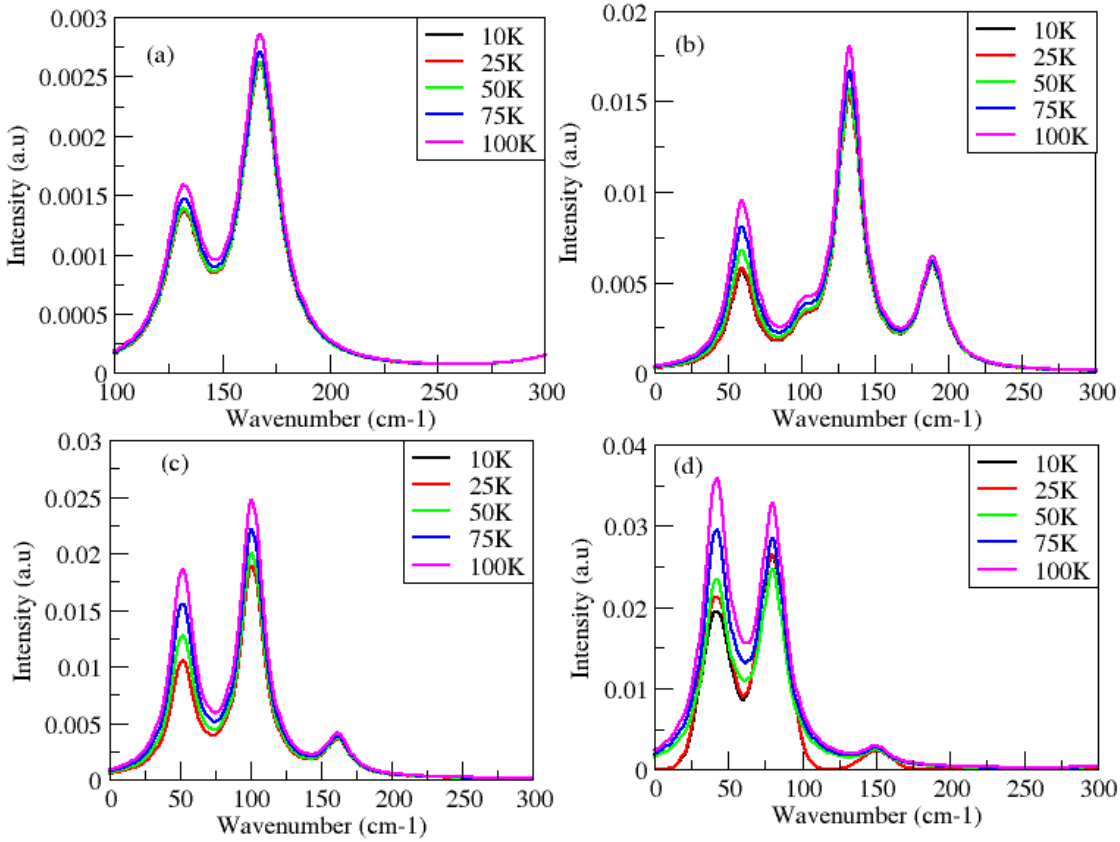

Figure 4.8: Effect of temperature on the intensity of Raman spectrum of (a) BiOF, (b) BiOCl, (c) BiOBr and (d) BiOI crystal.

4.1.5 Phonon and thermodynamics properties

Phonon calculation provides valuable information regarding the properties, such as thermal expansion, specific heat capacity, heat conduction, electron-phonon interactions, supercon-

ductivity, and resistivity. X-ray scattering and neutron scattering can be used experimentally to determine such properties of the materials. Currently, the phonon properties of the BiOX crystal have been calculated on the basis of the density functional perturbation theory (DFPT) method. The phonon dispersion curves in the Brillouin zone provide insight into the variation in the phonon energy with the q-vector along directions of high symmetry. The BiOX crystal unit cell consists of three types of atoms: Bi, O, and X (F, Cl, Br, or I). As a result, it has three acoustic and 3(N-1) optical phonon modes of vibration. Hence, there are longitudinal optical (LO), transverse optical (TO), longitudinal acoustic (LA) and transverse acoustic (TA) phonon modes for all BiOX crystals. In Fig.4.9, the phonon vibrations and their density of states for BiOF and BiOCl are plotted. Figure 4.9 (a) shows that the phonon dispersion for the BiOF crystal has only one region. On the other hand, the phonon dispersions for BiOCl, BiOBr and BiOI crystals have two characteristic regions separated by a phonon gap or forbidden frequency gap around (6–8) THz. The phonon dispersion and density of states for the BiOBr and BiOI crystals are plotted in Fig. 4.10. In the low-frequency range, there is a hybrid of TO, LA and TA phonon modes. This is due to the vibrations of Bi atoms causing acoustic phonons and optical phonons to produce low-frequency phonons. In the second region (above 6 THz), an optical phonon is generated from the vibrations of light oxygen atoms. The calculated phonon frequencies in all the BiOX crystal species are positive (Ferrer et al., 2018). This result confirmed that the optimized crystal structure of the BiOX crystal was geometrically stable. These findings align with previous research conducted by Dutta et al. [59] and Sajjad et al. [60]. According to Dutta et al., the dynamic stability of BiOF crystals was achieved by a compression strain of 4%. In our fndings, the dynamic stability of the phonon band dispersion of all the species of the BiOX crystal was attained without using compression strain.

The quasi-harmonic approach has been used to study the thermodynamic properties related to phonon vibration such as Helmholtz free energy (E), enthalpy, entropy, and isochoric heat capacity as a function of temperature. The statistical thermodynamic expressions used to determine the thermodynamic properties of BiOX crystals in the reciprocal space are discussed in section 2.2.4. The zero-point vibrational energy of the BiOX crystal was calculated. At absolute zero, the zero-point energy of the BiOX system is 0.316 eV, 0.258 eV, 0.337 eV, and 0.211 eV for BiOF, BiOCl, BiOBr, and BiOI, respectively. Figure 4.11(a-d) shows the thermodynamic properties of BiOX crystal at room temperature for each species. The graph of energy versus temperature indicates that as temperature increases, the degree of disorder in the crystal of BiOX species also increases because the particles get more kinetic energy. Similarly, as the temperature increases, the internal energy of BiOX crystal species increases, which means that the change in enthalpy of the system is positive at constant volume. However, as temperature increases, the Helmholtz free energy will decrease because there is a high degree of disorder at a large temperature in the crystal of BiOX crystal species. This is the consequence of the conservation of energy because, at non-zero temper-

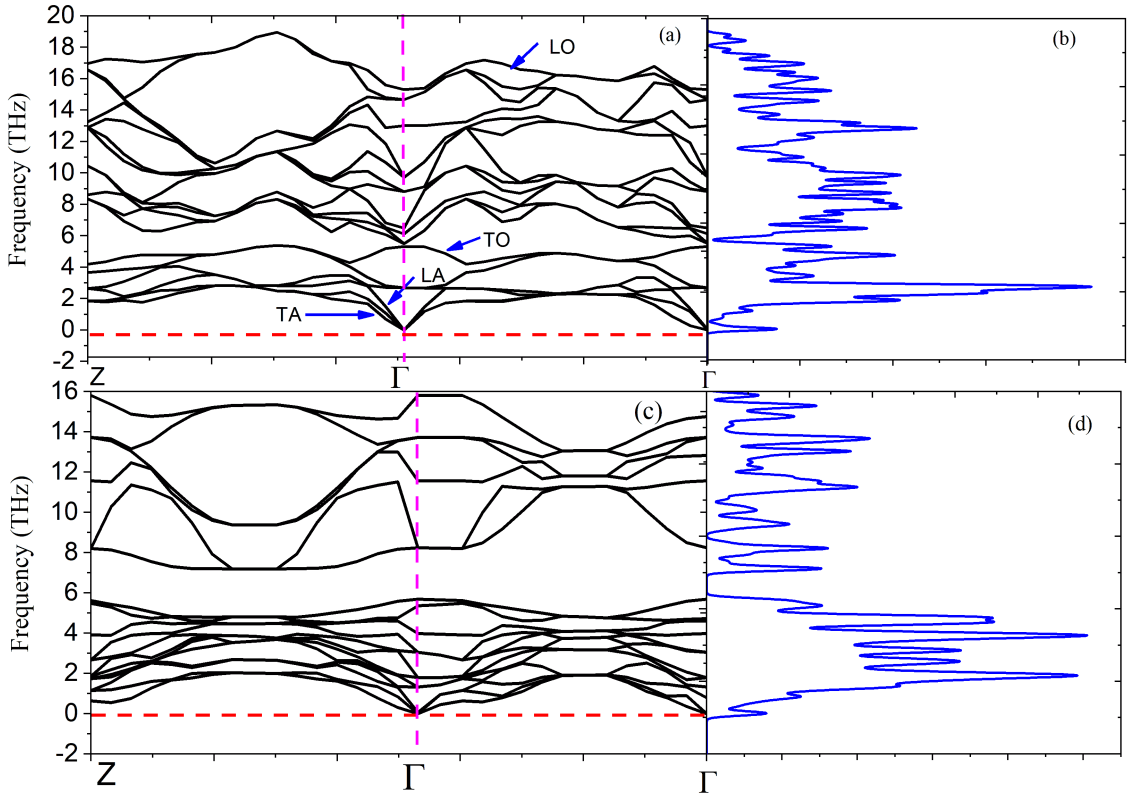

Figure 4.9: Phonon dispersion a(c) and DOS b(d) of BiOF(BiOCl) crystal respectively.

atures, the lattice's energy is not constant, but rather fluctuates randomly around some mean value. Random lattice vibrations, which can be viewed as a gas of phonons, cause these energy fluctuations. Furthermore, at a constant volume, as temperature rises, so does phonon oscillation, as their kinetic energy rises with temperature. As a result, the potential energy in the BiOX crystal system decreases.

The phonon density of states combines all possible phonons described by the above phonon dispersion relations to determine a crystal's heat capacity. The heat capacity of harmonic oscillators of BiOX crystal species was calculated at constant volume and plotted in Fig. 4.12 (a). The results show that, at high temperatures, the heat capacity of BiOX crystal is independent of temperature, which agrees with the classical result of Dulong and Petit's law of solids materials. This shows the existence of an anharmonic effect at high temperatures. The calculated value of the specific heat capacity at room temperature is 29.9, 30.7, 31.8 and 32.4 J/mol.K for BiOF, BiOCl, BiOBr and BiOI crystal respectively. As seen in Fig. 4.12(a), in the temperature range of 5 K to 200 K, there is a rapid increase in heat capacity with temperature. But below 5 K temperatures, the vibrational heat capacity of BiOX crystals confirms that the vibrational degrees of freedom of atoms are getting frozen out. At absolute zero temperature, crystal lattices do not have phonons in their ground state. The temperature dependence of heat capacity is given by the Debye model.

The Debye temperature can be linked to the Debye frequency (the maximum frequency

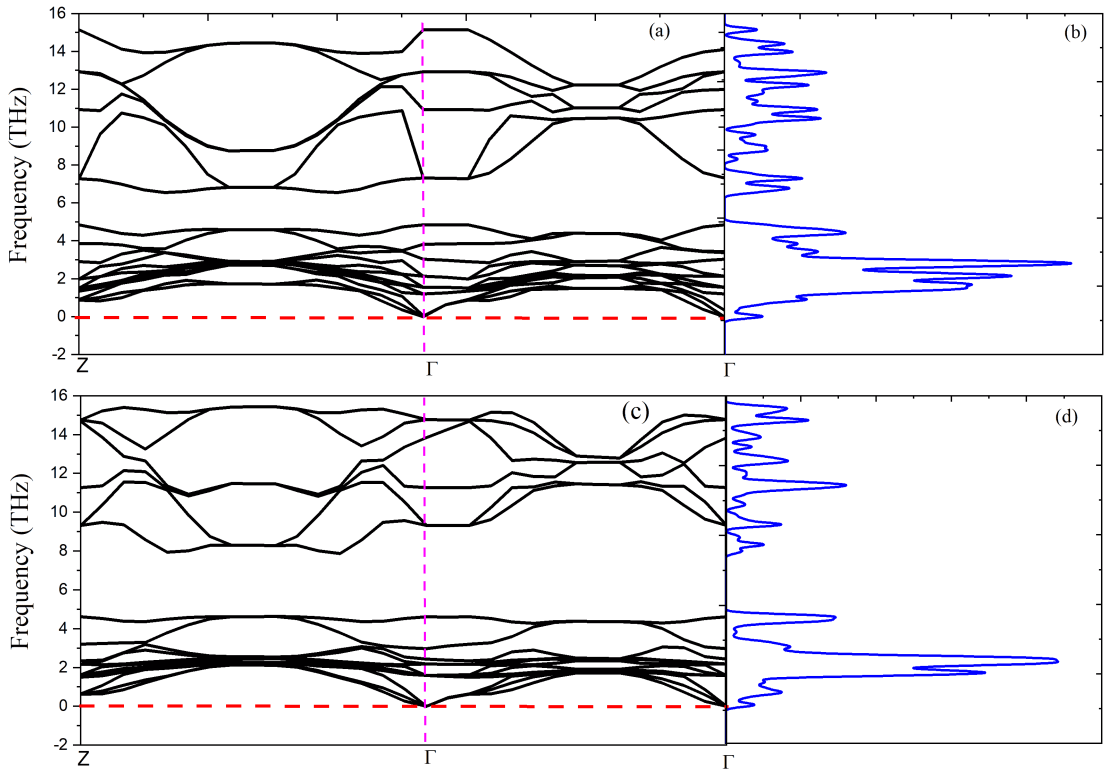

Figure 4.10: Phonon dispersion a(c) and DOS b(d) of BiOBr(BiOI) crystal respectively.

of the phonons in the crystal). Debye's temperature is proportional to sound velocity in the crystal. Figure 4.12(b) illustrates the Debye temperature versus temperature graph of the BiOC crystal. The results indicate that at high temperatures, the high kinetic energy of the crystal's atoms or molecules results in phonons with high velocities. In other words, phonon oscillation is faster at high temperatures than at low temperatures. Therefore, BiOX has the properties of hard materials at high temperatures but the properties of soft materials at low temperatures. Therefore, BiOX crystals exhibit promising thermoelectric properties at high temperatures. BiOX crystals can also be utilized in high-temperature sensors for applications such as gas sensing or combustion monitoring. Furthermore, the wide band gap and surface properties of BiOX crystals make them potential catalysts for high-temperature reactions, such as oxidative coupling of hydrocarbons, steam reforming, or selective oxidation. At low temperatures, the band gap energy of BiOX crystals allows them to absorb visible light and generate photo-excited charge carriers, enabling efficient solar energy conversion processes. BiOX crystals can be utilized as gas sensors at low temperatures, operating in ambient environment. Moreover, BiOX crystals, with their wide band gaps and photoconductive properties, hold potential for the development of optoelectronic devices such as photodetectors and light-emitting devices.

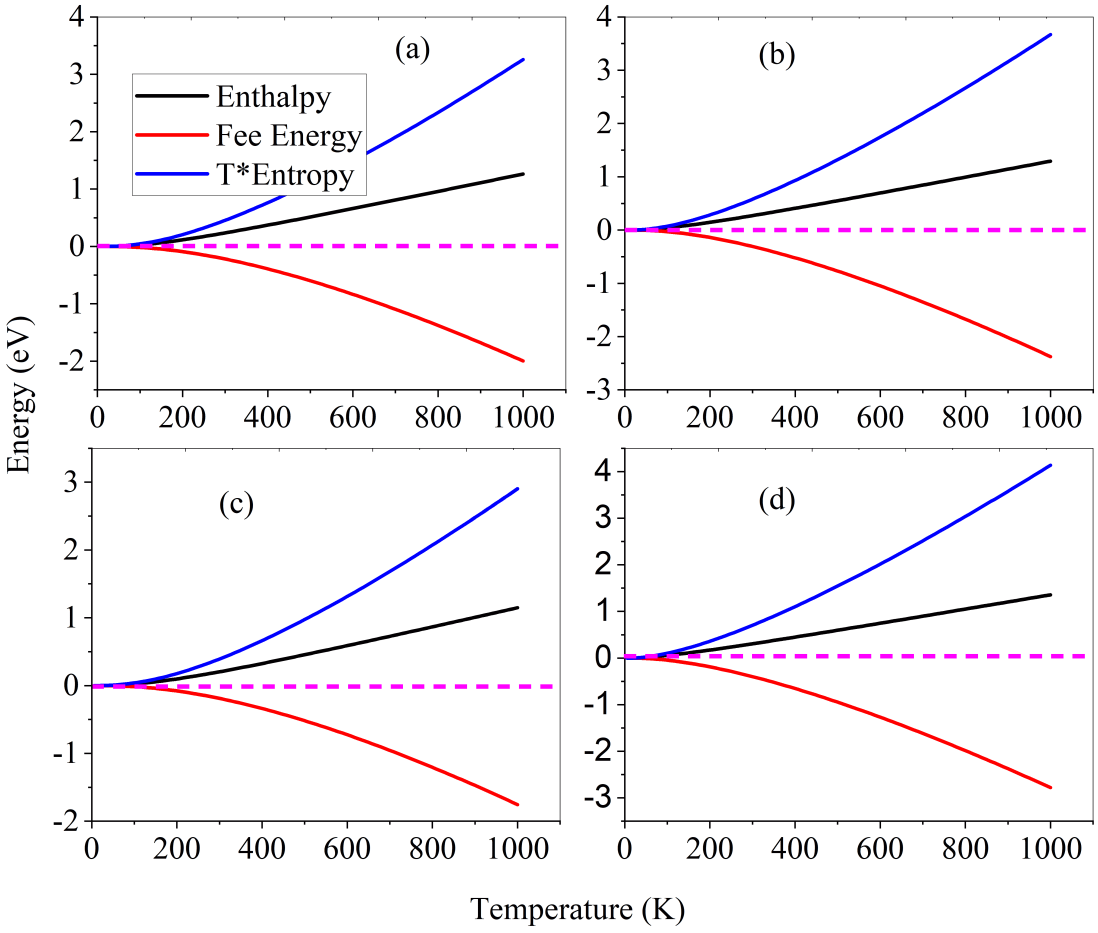

Figure 4.11: Helmholtz free energy, enthalpy, and entropy of (a) BiOF, (b) BiOCl, (c) BiOBr, and (d) BiOI crystal.

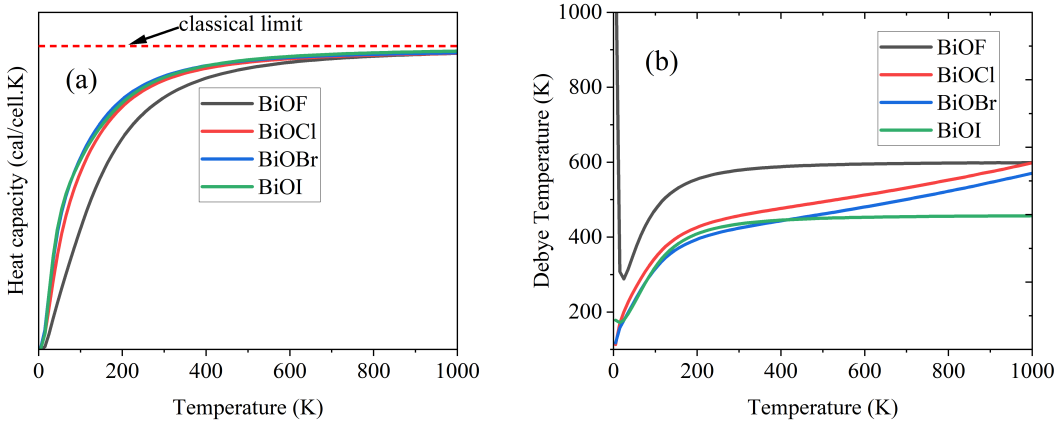

Figure 4.12: The heat capacity and (b) Debye temperature of BiOX crystal.

4.2 Electronic and optical of properties doped and co-doped BiOCl

4.2.1 Effect of doping and co-doping on electronic properties

The crystal structure of bismuth oxychloride (BiOCl) is tetragonal, classified under space group P4/nmm (no. 129). It features layers of $[Bi_2O_2]$ double units, with chloride ions interleaved to maintain charge neutrality. In the $[Bi_2O_2]$ unit, bismuth ions are arranged in a square planar configuration, with oxygen ions positioned above and below. This structure contributes to BiOCl's semiconductor properties and photocatalytic activity.

Upon doping with post-transition metals (In, Sn, Tl), minimal lattice distortions were observed, attributed to difference in ionic radii and valence configurations. The top view of the crystal structure of the undoped and post-transition metal-doped BiOCl crystal is shown in Fig. 4.13. The unit cell of BiOCl contains six atoms, with Bi^{3+} coordinated to four O^{2-} and four Cl^{1-} ions in a four-coordinate arrangement. Characteristic bond lengths are 2.34 Å (Bi-O), 3.10 Å (Bi-Cl), and 3.91 Å (Bi-Bi). Recent studies have confirmed that the experimental lattice parameters for both pristine and Sn-doped BiOCl align closely with theoretical predictions, with slight variations noted along the c-axis. Doping does not alter the fundamental crystal structure, indicating structural stability despite changes in bond lengths due to size differences between dopants and host atoms (Zulkiflee et al., 2023b).

The optimized lattice parameters of the pristine and doped systems are summarized in Table 4.4. Recently, Zulkiflee et al. reported that the experimental lattice parameters for pristine and Sn-doped BiOCl were a = b = 3.885; 3.876 Å, and c =7.371; 7.343 Å, (Zulkiflee et al., 2023b). The calculated lattice parameters were in agreement with previously reported experimental results (Xie et al., 2014; Zulkiflee et al., 2023b). The crystal structure of Sn/Br co-doped is depicted in Fig. 4.14.

The electronic band structures of pristine BiOCl, In-doped BiOCl, Sn-doped BiOCl, and Tl-doped BiOCl were computed along a high-symmetry path in reciprocal space, which includes the k-points Γ, X, M, Z, R, and A. The resulting band structures for these materials are illustrated in Figure 4.15(a-d). BiOCl exhibits semiconductor behavior characterized by a layered structure. The band arrangement reveals that the valence band is predominantly composed of oxygen (O) and chlorine (Cl) p orbitals, while the conduction band primarily consists of bismuth (Bi) p orbitals. Notably, BiOCl displays a valence band maximum (VBM) at the R k-point and a conduction band minimum (CBM) at the Z k-point, indicating its nature as an indirect band gap semiconductor.

The impurity states emerge within the band gap of doped BiOCl crystals (Fig. 4.15(b-d)) due to the presence of dopant atoms. This result is consistent with previous reports (Zulkiflee et al., 2023b; Long et al., 2022). Doping BiOCl with In, Sn, or Tl results in specific energy band configurations. For example, the distance between the impurity energy band's bottom

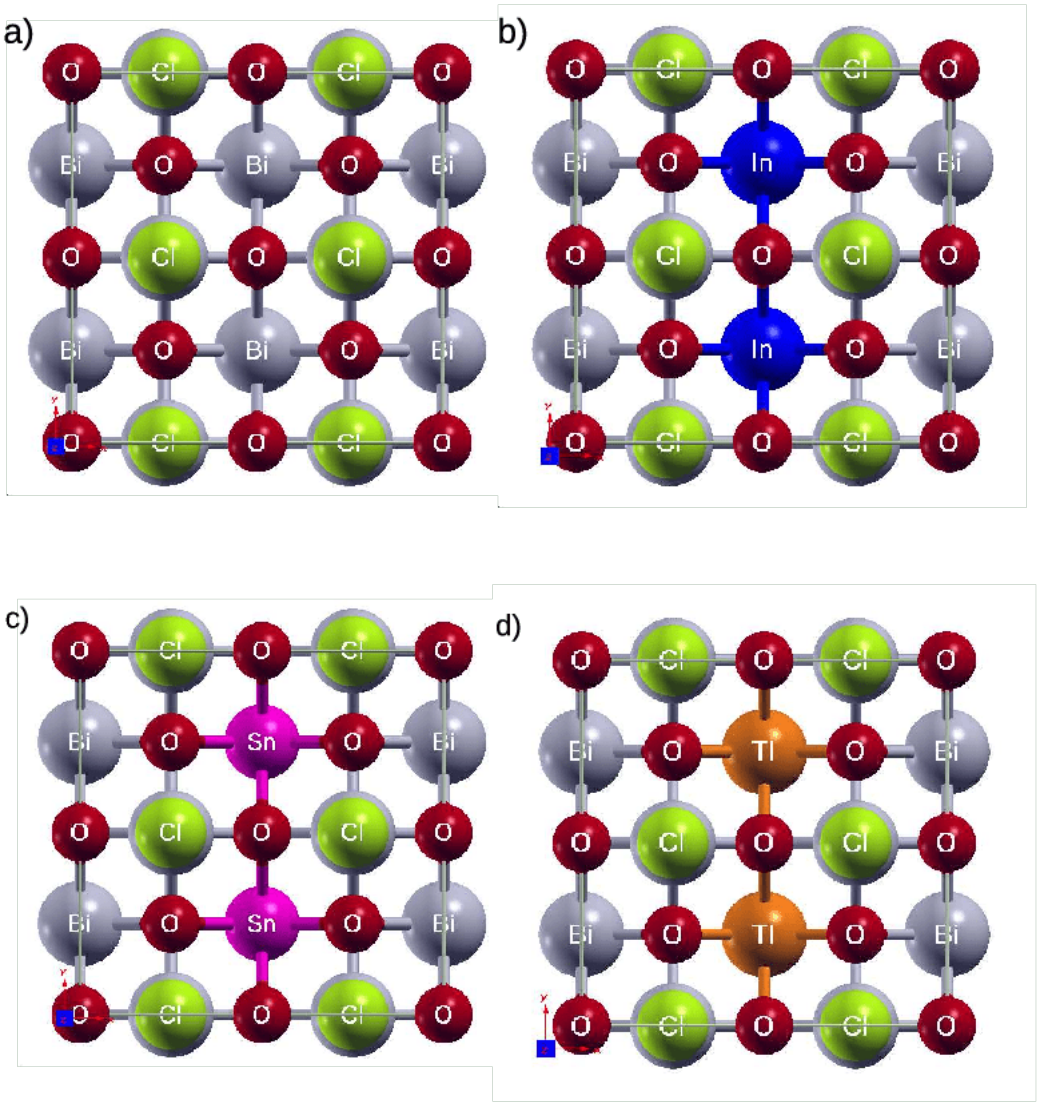

Figure 4.13: The Crystal structure of (a) Pure BiOCl, (b) In-doped BiOCl, (c) Sn-doped BiOCl and (d) Tl-doped BiOCl

and the valence band's top is 0.62 eV for In-doped, 0.77 eV for Sn-doped, and 1.47 eV for Tl-doped BiOCl. Additionally, the gap between the impurity energy band's top and the conduction band's bottom varies, with values of 1.83 eV for In-doped, 1.58 eV for Sn-doped, and 1.07 eV for Tl-doped BiOCl. The width of the impurity band gap also differs among these doped crystals, measuring 0.40 eV for In-doped, 0.61 eV for Sn-doped, and 0.19 eV for Tl-doped BiOCl. As a result, the differences between the highest point in the valence band and the lowest point in the conduction band are 2.45 eV for In-doped, 2.35 eV for Sn-doped, and 2.54 eV for Tl-doped BiOCl. These values are less than the energy gap observed in pure BiOCl crystals (2.80 eV). These calculations suggest that incorporating posttransition metals into the BiOCl host creates new impurity energy levels while preserving the fundamental characteristics of the electronic structure of BiOCl. In addition, the current findings indicate

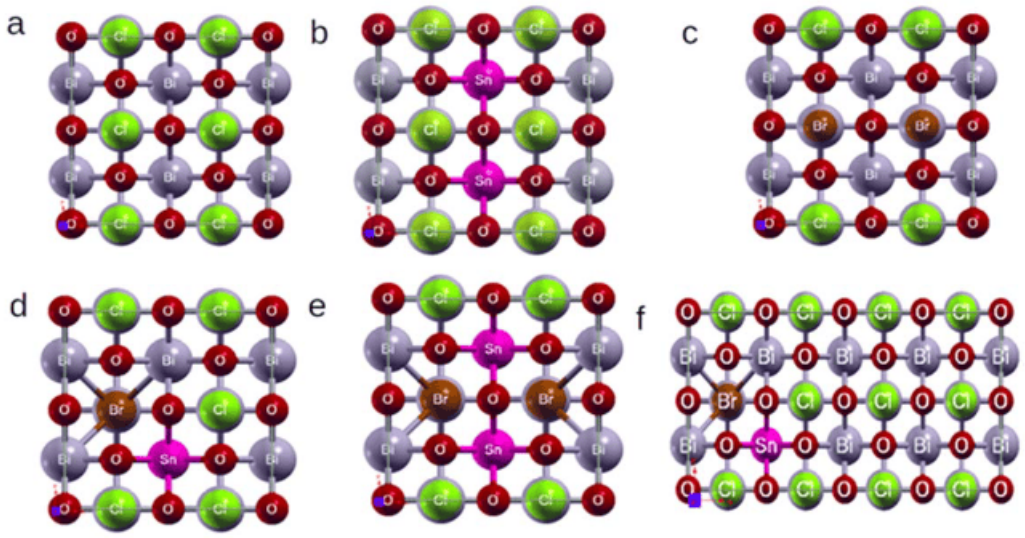

Figure 4.14: (a) Top view of 2× 2 × 1 supercell of pure BiOCl, (b) $Sn_{0.25}Bi_{0.75}OCl$, (c) $BiOBr_{0.25}Cl_{0.75}$ (d) $Sn_xBi_{1-x}OBr_xCl_{1-x}$,(x = 0.25), (e) $Sn_xBi_{1x}OBr_xCl_{1-x}$ (x = 0.125), and (f) 4× 2 × 1 supercell of $Sn_xBi_{1-x}OBr_xCl_{1-x}$ (x = 0.0625), crystal structure

.

that the energy required to excite an electron in any of the doped crystals is reduced due to the formation of intermediate states (Attri et al., 2023; Belousov et al., 2023).

Additionally, the electronic band structure of Sn/Br co-doped BiOCl was calculated and is presented in Fig. 4.16(a-d). The analysis indicates that Sn/Br co-doping preserves the

Table 4.4: Calculated value of bond angles, bond length, lattice parameters and band gap of pristine, doped and co-doped BiOCl crystal.

Crystal	Angles(^{o})		Distances(Å)		Lattice Parameter (Å) a=b	c	E_g (eV)
BiOCl	O-Bi-O	113.57	Bi-O	2.34	3.91	7.88	2.80
	Cl-Bi-Cl	78.45	Bi-Cl	3.10			
	O-Bi-Cl	73.50	Bi-Bi	3.91			
Sn-BiOCl	O-Bi-O	112.45	Bi-O	2.29	3.83	8.46	2.35
	Cl-Sn-Cl	78.61	Bi-Cl	3.01			
	O-Sn-Cl	73.76	Bi-Sn	3.81			
BiOCl-Br	O-Bi-O	108.66	Bi-O	2.34	3.94	8.23	2.30
	Cl-Bi-Br	77.25	Bi-Cl	3.07			
	O-Bi-Br	76.52	Bi-Sn	3.90			
6.25% Sn/Br-BiOCl	O-Sn-O	76.74	Bi-O	2.26	3.88	8.42	2.30
	Bi-O-Bi	112.40	Bi-Bi	3.88			
	Bi-Cl-Bi	79.92	Bi-O	2.34			
12.5% Sn/Br-BiOCl	O-Sn-O	76.44	Bi-O	2.37	3.90	8.62	2.02
	Cl-Sn-Br	74.45	Bi-Cl	3.07			
	O-Bi-O	71.34	Bi-Sn	3.90			
25% Sn/Br-BiOCl	O-Bi-O	111.24	Bi-O	2.35	3.89	8.36	2.20
	Cl-Sn-Br	76.20	Bi-Cl	3.06			
	O-Bi-Br	73.57	Bi-Sn	3.89			

indirect band gap characteristic of BiOCl, with the maximum valence band (MVB) and minimum conduction band (MCB) appearing at distinct high-symmetry points. The bandgap of the co-doped BiOCl crystal is narrower compared to both the Sn-doped and pristine BiOCl, aligning with previous experimental observations reported by (Li et al., 2018). The introduction of Sn and Br atoms generates additional localized energy states within the band gap due to differences in electronic configurations and atomic sizes between Sn and Bi, as well as Cl and Br. These new states facilitate band gap narrowing, which directly impacts its optical properties, including absorption spectra, transparency, and charge carrier dynamics (Li et al., 2018; Xie et al., 2014). A reduced band gap enhances BiOCl's ability to absorb light at longer wavelengths, notably within the visible spectrum, thereby increasing its optical absorption efficiency.

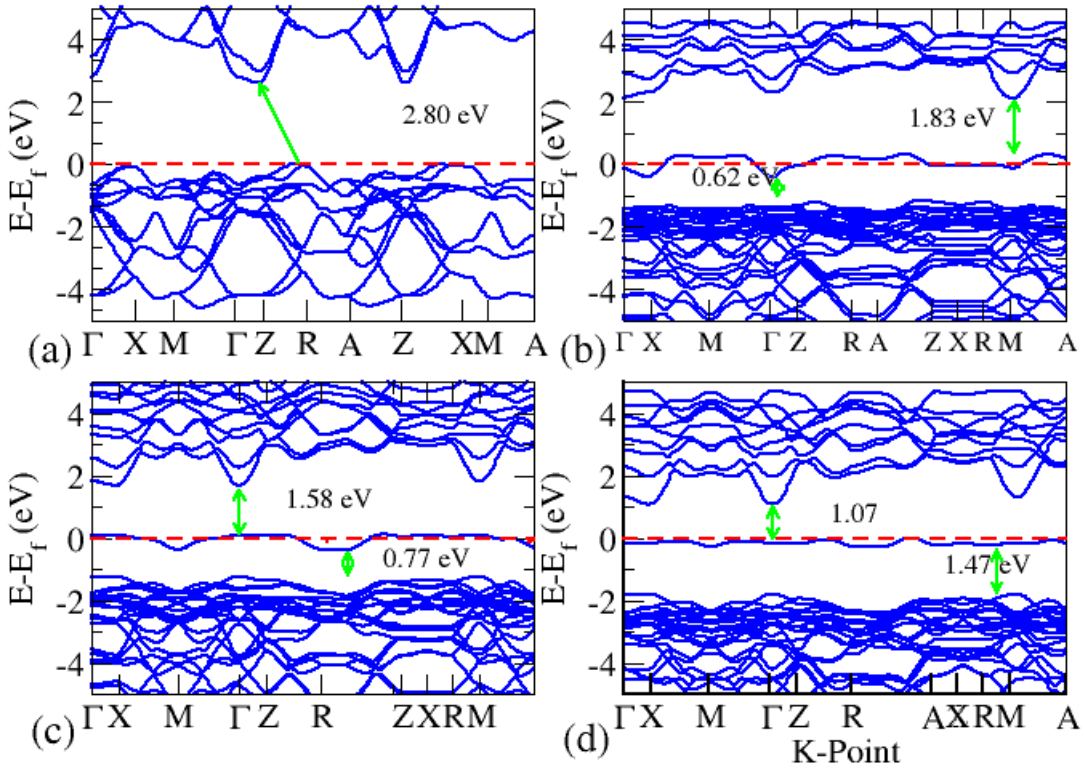

Figure 4.15: Electronic band structure of (a) pure BiOCl, (b) In-doped BiOCl, (c) Sn-doped BiOCl and (d) Tl-doped BiOCl

Figure 4.17 shows the total density of states and projected density of states for different atoms in the In-doped BiOCl crystals. The results indicate that the In-doped BiOCl crystals' valence band primarily consists of hybridizing O and Cl atoms. Figures 4.17 (b-d) illustrate the projected density of states (PDOS) for the In-doped BiOCl crystal. The valence band is

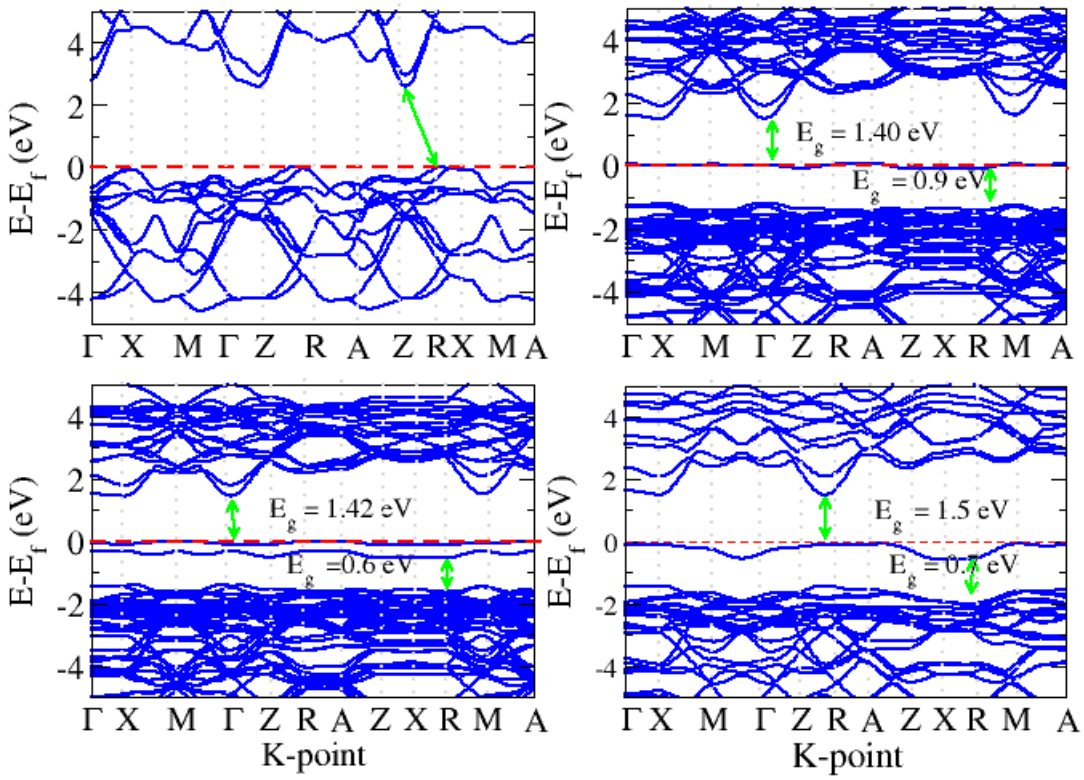

Figure 4.16: Optical bandgap of (a) BiOCl, (b) 6.25% Sn/Br-BiOCl, (c) 12.5% Sn/Br-BiOCl-Br and (d) 25%Sn/Br-BiOCl.

predominantly influenced by the hybridization of the O 2p and Cl 3p states, whereas the Bi 6p states are crucial for the conduction band. These findings align with previous studies, and the impurity energy band mainly consists of In-5 s states [Fig. 4.17 (c)], showing localized states. Figure 4.18 (a) illustrates the total density of states and projected density of states for various atoms in the Sn-doped BiOCl crystal. The results demonstrate that the valence band of the Sn-doped BiOCl crystal primarily consists of a hybridization of O and Cl atoms.

Figure 4.18 (b-d) shows the PDOS from the orbitals of each atom in the In-doped BiOCl crystal. The valence band consists of O-2p and Cl-3p states and the conduction band is dominated by Bi-6p states. These bonding characteristics are consistent with previous findings (Barhoumi and Said, 2021) and are maintained in the case of In-doped BiOCl, where the impurity energy band consists primarily of Sn-5 s states [Fig. 4.18 (c)], displaying isolated and localized states. Notably, vacant states are formed above the Fermi level (half-occupied) due to the presence of Sn impurities.

The DOS of the Tl-doped BiOCl crystal is shown in Fig. 4.19 (a). The valence band of the Tl-doped BiOCl crystal is mainly formed by the hybridization of O and Cl atoms. The

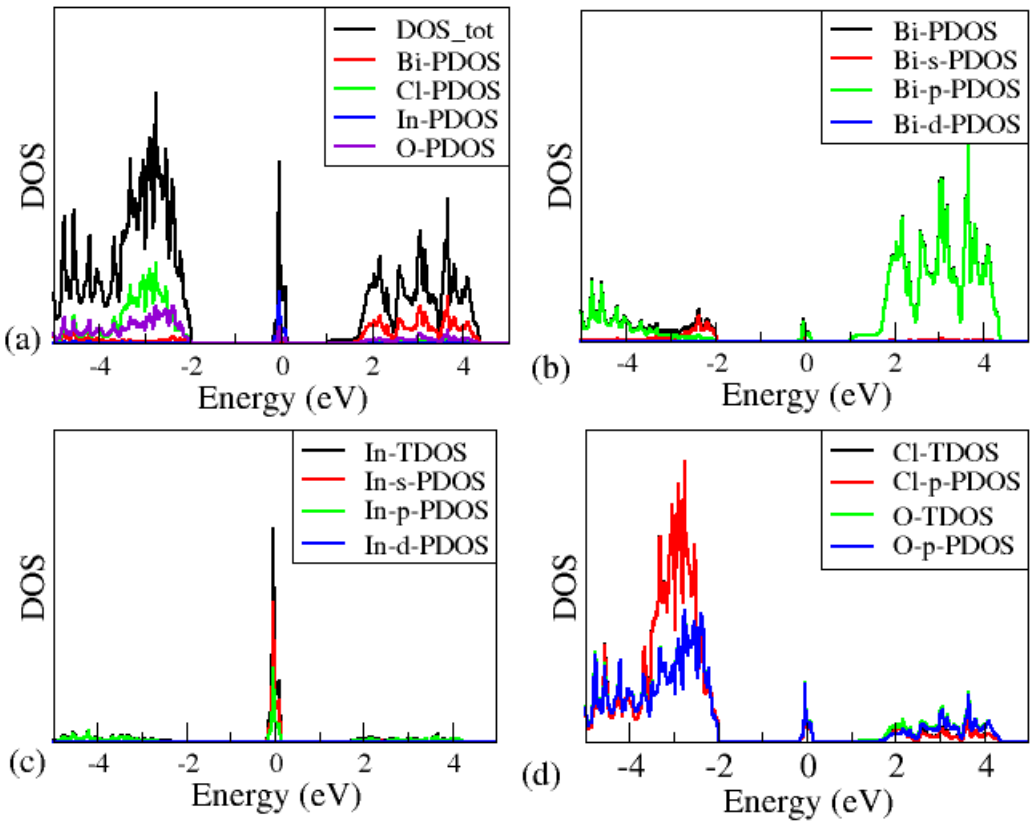

Figure 4.17: TDOS and PDOS of In-doped BiOCl

projected density of states for the orbitals of each atom is illustrated in Fig. 4.19 (b-d). As with In- and Sn-doped BiOCl crystals, the valence band is a hybridization of O-2p and Cl-3p states, while the conduction band is predominantly composed of Bi-6p states. The interband level in the Tl-doped BiOCl crystal arises from the presence of Tl atoms, primarily from the 5 s orbital states [Fig. 4.19 (c)].

The total density of states and the partial density of states (PDOS) of each atom in co-doped are shown in Fig. 4.20 (a). The PDOS of each element's atomic orbital states are displayed in Fig. 4.20 (b-f). According to the finding, the valence band (VB) of Sn/Br co-doped BiOCl crystal is composed of Cl(3p), Br(3p), O(2p), Sn(5s) states. The conduction band (CB) is mainly composed of the Bi(6p) states. This confirms that there is an optical transition of the electron from the top valence states to the conduction bands. Therefore, the presence of Sn and Br atoms in the crystal brings about a change in the electronic structure. There is a redshift in the energy state to a lower energy level (large wavelength). Our findings are inconsistent with previously reported experimental results (Zulkiflee et al., 2023b; Chen et al., 2020; Xie et al., 2014). These energy changes can influence the electronic transition and optical absorption properties of the materials.

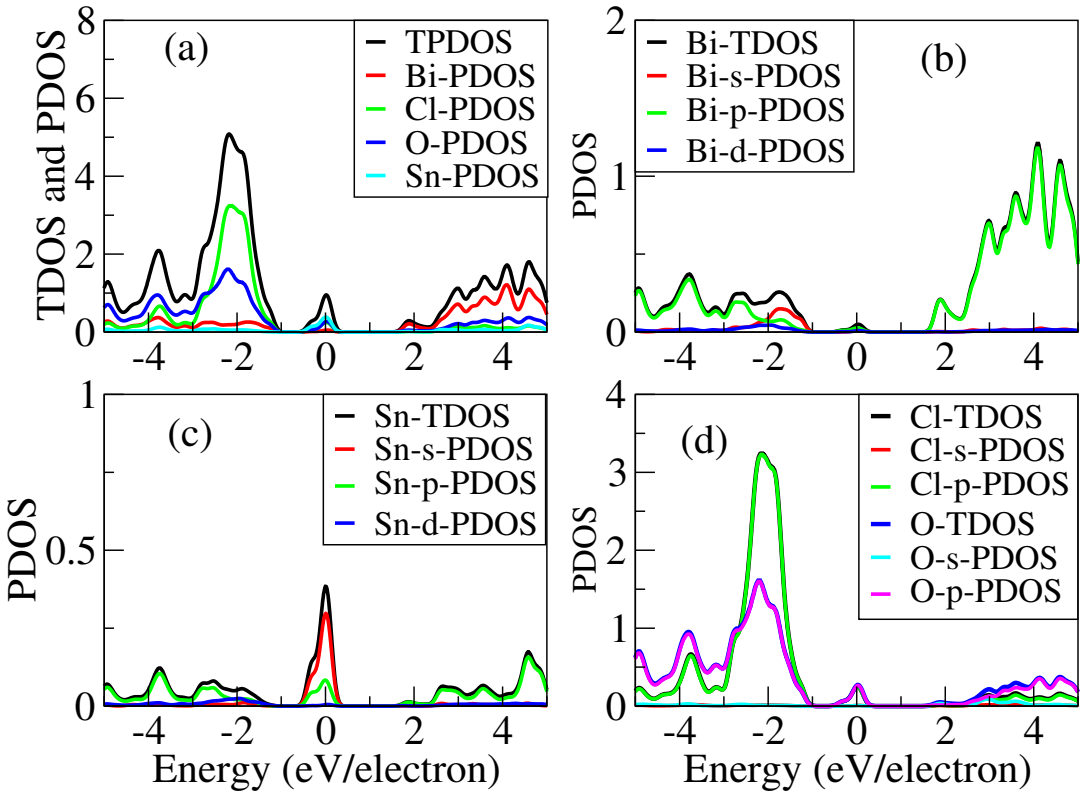

Figure 4.18: TDOS and PDOS of Sn-doped BiOCl crystal

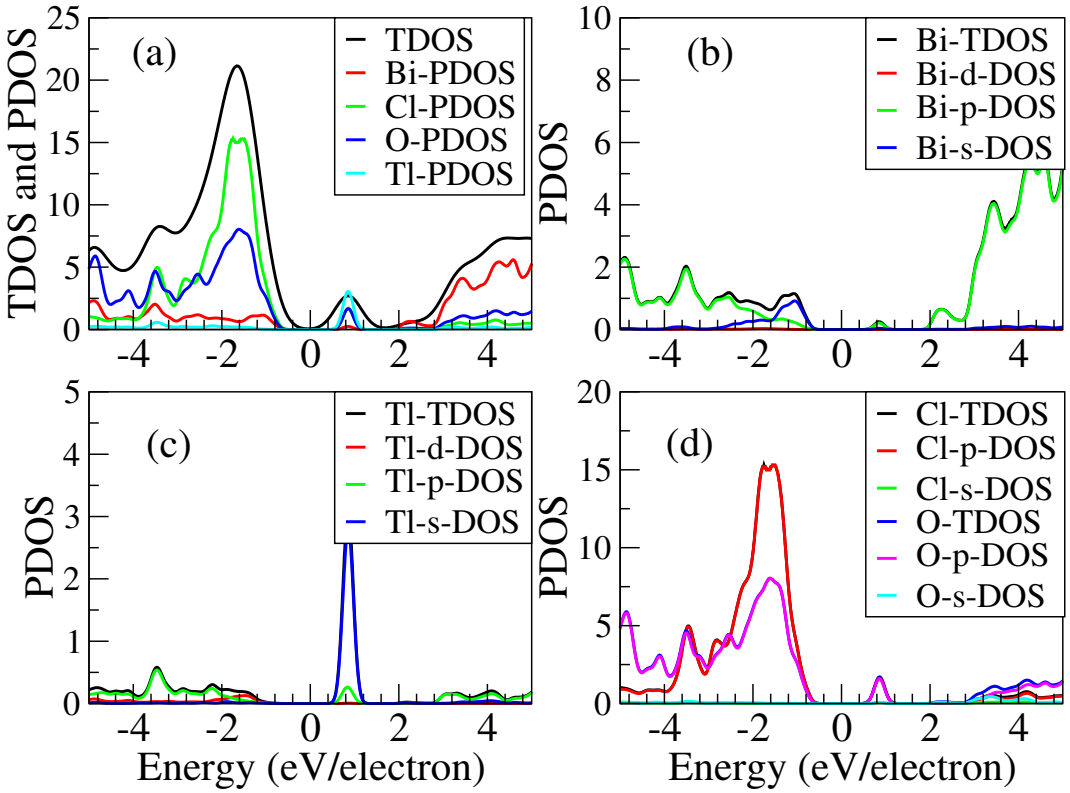

Figure 4.19: TDOS and PDOS of Tl-doped BiOCl crystal

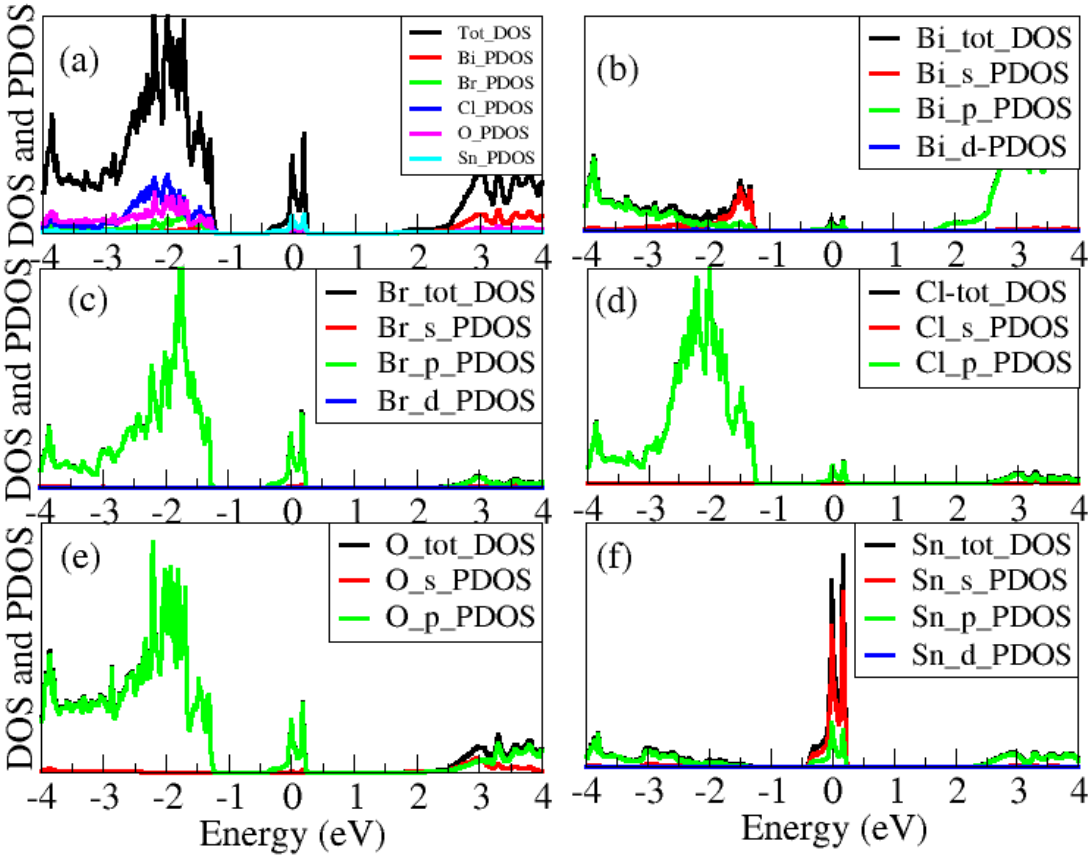

Figure 4.20: (a) PDOS of the 25 % Sn/Br co-doped BiOCl crystal (b) PDOS of the Bi atom from each orbital, (c) DOS of the Br atom from each orbital, (d) DOS of the Cl atom from each orbital, (e) PDOS of the O atom from each orbital, and (f) PDOS of the Sn atom from each orbital.

The JDOS of pristine BiOCl and doped BiOCl crystal has been calculated and plotted in Fig. 4.21. The results demonstrate that broad peaks were observed at 3.5 eV, 2.00 eV, and 1.77 eV, for pure BiOCl, 25% Sn-BiOCl, and 25% Sn / Br-BiOCl, respectively. The peak in the JDOS plot indicates an electronic transition from the highest valence band to the lowest conduction band due to the absorption of photons. However, there is no peak observed in the energy range of (0-3) eV for pristine BiOCl crystal due to its wide band gap nature. Hence, Sn and Sn/Br co-doping significantly enhances the optical transition in the lower energy of pure BiOCl crystal. The DOS results generally indicate that incorporating In, Sn, and Tl dopants into BiOCl crystals leads to alterations in the valence and conduction bands, which impacts the optical transitions and absorption characteristics of the material. These findings are consistent with prior studies Liu et al. (2022b); Nussbaum et al. (2014b); Han et al. (2016) and highlight the significance of changes in the electronic structure and optical properties caused by dopant integration in pristine BiOCl crystal.

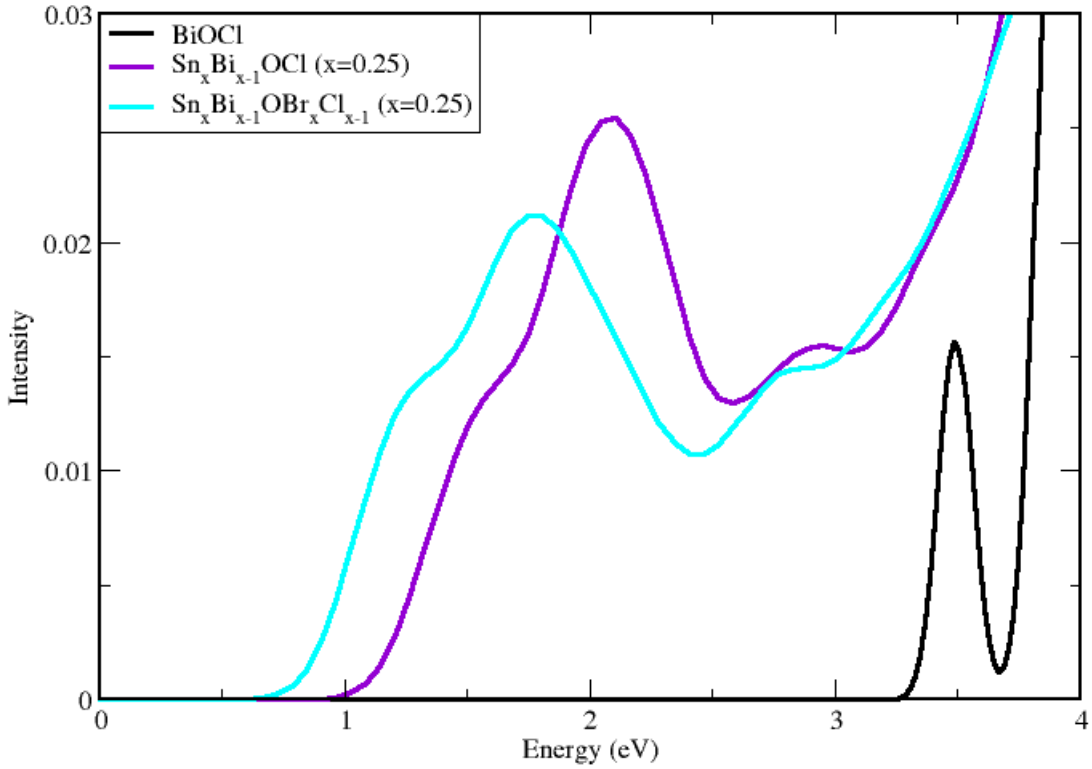

Figure 4.21: The joint density of state for pristine 25%Sn-doped and 25% Sn/Br co-doped BiOCl crystal

.

4.2.2 Effect of doping and co-doping on optical properties

The crystal structure of a material has a significant influence on its optical properties. This is useful for analyzing energy band structure, contamination levels, excitons, lattice defects, lattice vibrations, and magnetic stimulation Barhoumi and Said (2021). It is well-known that the external field can polarize the material. The optical properties of materials are generally assessed using various optical parameters. Figure 4.22, illustrates the optical properties of pure BiOCl and various post-transition metal-doped BiOCl crystals. Figure 4.22(a) shows the absorption spectra of both pure BiOCl and post-transition metal-doped BiOCl crystals. According to the results, the absorption edge of all post-transition metal-doped BiOCl crystals is shifted towards the low-energy region (redshift) compared to the pristine one. Additionally, a new peak is observed in the low-energy region for all doped crystals. The absorption edge of Sn-doped BiOCl shifts more toward the lower energy region than In and Tl-doped BiOCl. As a result, Sn-doped BiOCl absorbs more visible light than In-doped, Tl-doped, and pristine BiOCl. Overall, the findings demonstrate that post-transition metal

doping significantly enhances the absorption coefficient in the visible region for pure BiOCl. The peak position on the absorption graph corresponds to electronic transitions from the valence to the conduction band. In doped crystals, the optical transition occurs from the Cl and O p-states to the Bi p-states in the lowest conduction band. The introduction of dopants aids the transition of electrons from the top of the valence band to the conduction band at lower energy levels (Belousov et al., 2023). Additionally, the peak seen in the absorption spectra suggests that the doped crystals are more likely to absorb visible light compared to pure BiOCl crystals. These findings align with those reported in the literature (Zhang et al., 2017; Attri et al., 2023). Therefore, the significant absorption within the visible spectrum observed in post-transition metal (In, Sn, Tl)-doped BiOCl crystals indicates substantial potential for improving solar energy utilization and boosting the efficiency of solar cells and photocatalytic processes.

Figure 4.22 (b) shows an extinction coefficient of pure BiOCl and doped BiOCl crystal. The result shows that there is an additional peak observed in the visible light energy zone compared to that of the pristine one. This result also agrees with the absorption coefficient graph. Another important parameter used to analyze the optical properties of materials is the dielectric function. The dielectric constant, or relative permittivity, quantifies the capacity of a material to retain electrical energy within an electric field.

Figure 4.22 (c) refractive index of pure BiOCl and post-transition metals doped BiOCl crystal. The refractive index serves as a crucial optical parameter dictating the behavior of light within a material. In the context of pure BiOCl crystals, the refractive index typically ranges from 2.3 to 2.5 in the visible light spectrum, reflecting a notably high value. This high refractive index primarily arises from the substantial polarizability of Bi^{3+} cations and the unique layered crystal structure, which instigates significant dielectric anisotropy (Zhou et al., 2023). The refractive index of BiOCl can be adjusted by manipulating the crystal lattice, for example, through defect introduction or doping. Introducing post-transition metals like In, Tl, or Sn as dopants into BiOCl can elevate the material's optical characteristics. The addition of these dopants can introduce new energy levels within BiOCl's bandgap, influencing its electronic structure and light absorption properties. Doping has the potential to modify the refractive index of BiOCl by either inducing changes in the crystal structure or creating fresh electronic states. Notably, studies have shown that Sn-doped BiOCl exhibits a heightened refractive index compared to its pure counterpart, attributable to the electronic polarizability of Sn^{4+} ions. Likewise, other post-transition metal dopants such as In and Tl can similarly impact the refractive index of BiOCl through analogous mechanisms.

We have calculated the dielectric function of both pure and doped BiOCl crystals. Figure 4.22(d) displays the real dielectric function of both pure BiOCl and doped BiOCl crystals. The relative dielectric constant for the pure BiOCl crystal is 5.26. However, for the doped BiOCl crystals, the calculated static dielectric constants are 5.93, 6.93, and 6.15 for In-, Sn-, and Tl-doped BiOCl, respectively. This result shows that introducing post-transition

metals into the BiOCl crystal increases the static dielectric constant compared to the pristine one. This is because metal doping can alter the charge carrier concentration and mobility within the material. Consequently, this can change the electrical properties and the material's response to an applied electric field.

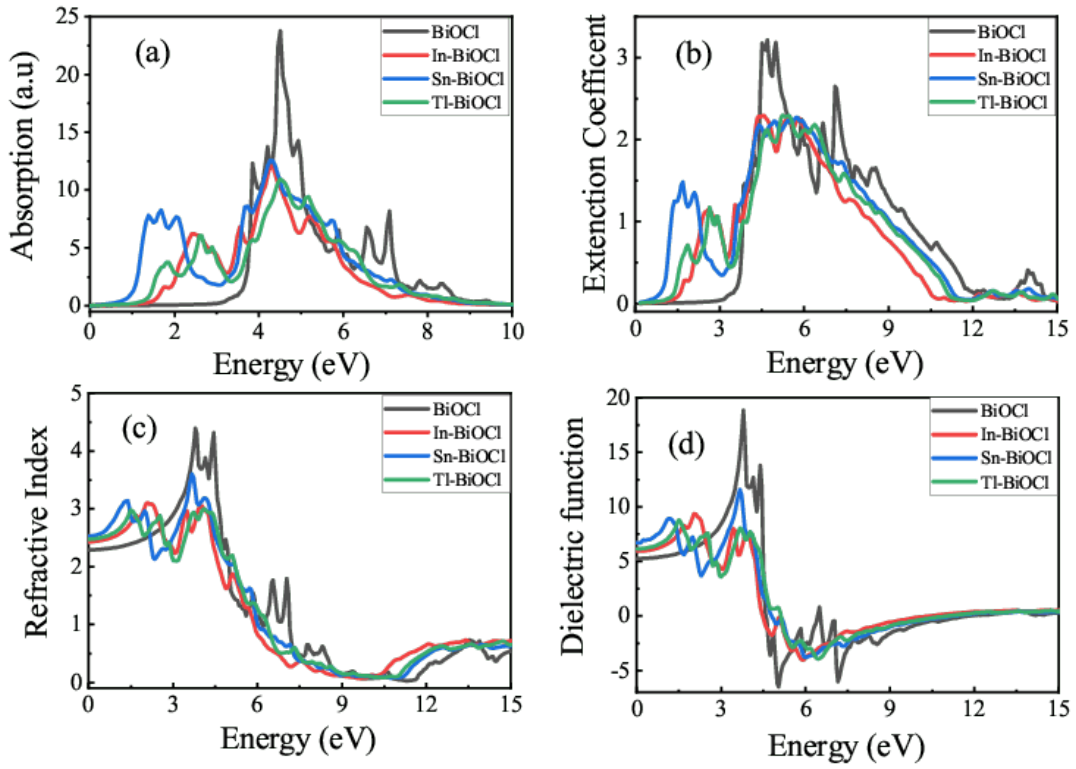

Figure 4.22: Optical properties of pure BiOCl and doped BiOCl, (a) the absorption spectra, (b) an extenction coefficient (c) refractive index and (d) dielectric function.

Furthermore, the optical properties of Sn/Br co-doped were investigated. Figure 4.23 (a-f) shows the dielectric and the electron energy loss function. The calculated static dielectric constant is different for the co-doped crystals in comparison to the pure BiOCl. The substitution of Bi with Sn and Cl with Br in the lattice can affect the charge distribution and polarization, leading to changes in the dielectric constant. The static dielectric constant for the pure and doped system was calculated, and its values are summarized in Table 4.5. Compared to pristine BiOCl, the static dielectric constant is larger for a doped system. This indicates that the dopants enhance the polarization and have a strong binding capacity to electrons; that is, they extend the life span of the photogenerated charge carrier on the conduction band, which is recommended for photocatalytic activity.

The peak position on the imaginary part of the dielectric function corresponds to electronic transitions from the valence to the conduction band. Because pure BiOCl and doped BiOCl have an indirect bandgap, the transition of electrons from the valence band to the conduction band requires the assistance of the phonon, resulting in peaks (Barhoumi and Said,

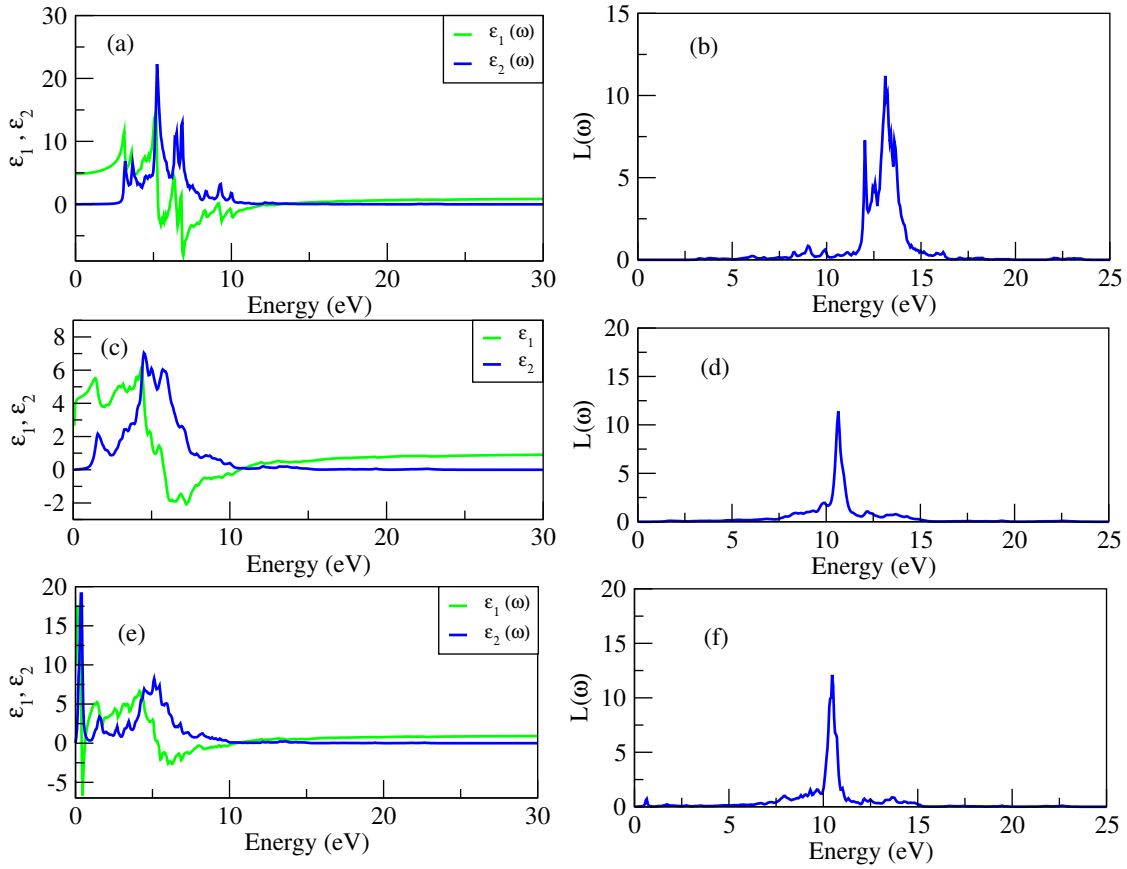

Figure 4.23: (a) Dielectric function, (b) Energy loss function of pure BiOCl crystal, (c) Dielectric function, (d) Energy loss function of 25% Sn/Br-BiOCl, (e) Dielectric function and (f) Energy loss function of 12.5% Sn/Br-BiOCl along ZZ-polarization direction.

2021). For pure BiOCl, the intense peak indicates the optical transition from the Cl 3p, Sn 3p, Br 3p, and O 2p states in the highest valence band to the Bi p states in the lowest conduction band. An extra peak is observed at lower energy for Sn/Br-doped BiOCl, indicating that the presence of dopants facilitates the transition of electrons from the top VB to the CB at lower energy, i.e., from the Sn 3p and Br 3p states to the Bi 6p state. Furthermore, the peak observed in the imaginary curve indicates the presence of an absorption band, revealing energy ranges where photons are more likely to be absorbed by the material. These absorption characteristics are particularly important for applications such as solar cells, light-sensitive detectors, and photocatalysis applications.

Another very important parameter in studying optical properties is the energy loss function. The energy loss corresponds to the difference between the initial and final states of the core electron. The energy-loss spectrum is a useful way of examining the electronic, structural, and vibrational characteristics of materials. It reveals the energy-loss or absorption processes that take place when a material is exposed to external stimuli such as photons or electrons. By studying the energy-loss spectrum, we can gain insight into the properties of the material. Figure 4.24(b-d) shows the energy loss function of a pure BiOCl and Sn/Br co-doped system along the XX, YY and ZZ-polarization directions. The sharp maxima in

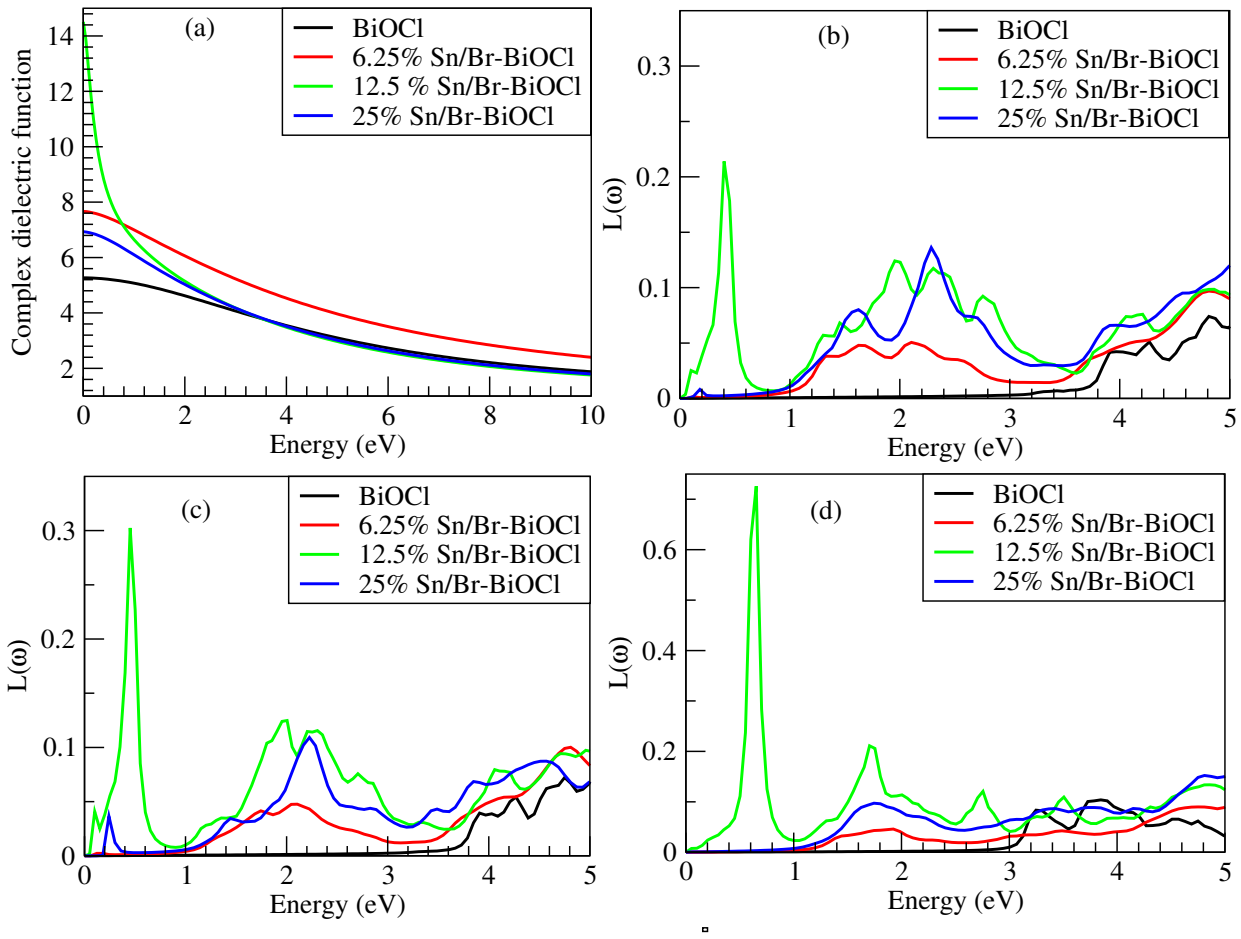

Figure 4.24: (a)complex dielectric function (b) Energy loss function along XX-polarization direction, (c) energy loss function along YY-polarization direction, (d) energy loss function along ZZ-polarization direction.

the energy loss function correspond to plasma oscillations. The plasma frequency for the pure BiOCl crystal along the crystallographic polarization directions of XX, YY, and ZZ appears at 10.9 eV, 12.12 eV and 11.22 eV, respectively. However, 6.25 % Sn/Br, 12.5% Sn/Br and 25% Sn/Br co-doped BiOCl have a plasmon frequency of 15.46 eV, 8.75 eV and 8.93 eV along ZZ-polarization direction respectively. In comparison to an undoped BiOCl crystal, the plasmon frequency for the doped system appears at different energies. This shows that doping can change the energy-loss properties of the BiOCl crystal. Sn/Br co-doping can affect the loss energy function of BiOCl, and through band modification, Sn/Br doping modifies the bandgap of pure BiOCl. Sn/Br co-doped BiOCl can absorb photons with lower energy and, consequently, experience higher energy losses. Band gap narrowing caused by Sn and Br doping results in increased absorption of visible light. Thus, Sn/Br co-doped BiOCl crystals have a small energy band gap and higher energy losses in the visible spectrum compared to those of pure BiOCl. Additionally, there are optical absorption that arises from the promotion of electronic transitions enabled by the defect energy levels introduced by the Sn and Br impurities. Moreover, Sn/Br co-doping may also affect the plasmonic behavior

Table 4.5: The peaks values of energy loss function between (0-5) eV along different polarization direction and its corresponding plasma energy and static dielectric constants of pure and Sn/Br-BiOCl crystal.

Crystal	Direction	Energy at peaks (eV)	$\hbar\omega_p$ (eV)	$\epsilon_1(0)$
BiOCl	XX	3.92, 4.25. 4.80	11.84	5.27
	YY	3.90, 4.24, 4.77	13.06	6.07
	ZZ	3.28, 3.82	13.17	4.85
6.25% Sn/Br-BiOCl	XX	1.68, 2.14, 4.78	19.27	3.52
	YY	2.07, 4.77	19.27	3.00
	ZZ	1.87, 4.69	19.27	4.25
12.5% Sn/Br-BiOCl	XX	1.62, 2.29	10.90	8.46
	YY	0.25, 2.25, 4.55	11.10	7.79
	ZZ	1.73, 4.83	10.60	14.4
25% Sn/Br-BiOCl	XX	1.73, 1.95, 2.34, 2.78, 4.14, 4.82	11.30	6.93
	YY	0.46, 1.98, 2.32, 4.07, 4.71	11.55	6.43
	ZZ	0.64, 1.75, 2.75, 3.50, 4.85	10.56	4.32

where, ω_p is plasma frequency

of BiOCl crystal. Plasmon are collective oscillations of electrons, and the introduction of Sn and Br impurities can alter the electron density and dielectric properties of the material. Extra electrons contribute to the overall electron density. As a result, the frequency of the plasmon tends to decrease with increasing Sn concentration. This decrease is due to the increased screening effect from the higher electron density, which reduces the strength of the collective electron oscillations.

We also evaluated the real values of the dielectric permittivity or complex dielectric function at the imaginary frequencies $\epsilon(i\omega)$ by utilizing the Kramers-Kronig formula. The complex dielectric function of a material describes its electrical response to an applied external electric field. The dielectric function versus imaginary frequency graph provides important insights into the optical properties of a material. The complex dielectric function is plotted in Fig. 4.24(a). The calculated static complex dielectric function along the ZZ-polarization direction where 5.20, 7.67, 14.39 and 6.98 for BiOCl, 6.25% Sn/Br-BiOCl, 12.5% Sn/Br-BiOCl and 25 % Sn/Br-BiOCl respectively. The findings demonstrate that doping alters the dielectric permittivity, which is consistent with the results from the real dielectric function curve. For Sn/Br co-doped system, the complex dielectric function changes with concentration due to the alteration in the material's composition and structure. It affects the arrangement and density of atoms in the BiOCl crystal, resulting in modifications to the electronic and vibrational properties.

4.3 Molecular interaction and adsorption of dyes on bismuth oxychloride surfaces

4.3.1 Molecular orbitals and population analysis

Molecular orbitals and population analysis are essential factors for comprehending electron distribution, which aids in predicting molecular reactivity, stability, and interactions. In this study, NAO and NBO analyses of MB, MO, and MR dyes were performed via Gaussian NBO Version 3.1 as implemented in Gaussian 09 software. NPA revealed that MB has a stable electronic structure characterized by high occupancy of the core (99.96% of 24 electrons) and high valence levels (99.6% of 52 electrons), indicating robustness in its molecular integrity and reactivity. The near-complete occupancy of the core and valence populations suggests a balance that enhances the stability and interaction capabilities of the dye. The minimal contribution from the natural Rydberg basis, comprising only 0.29% of the 76 electrons, supports the hypothesis that excitation to higher electronic states is limited. The optimized structure and atomic charge distributions of the MB dye, represented by NAO and NBO analyses, are illustrated in Fig. 4.29 (a) and (b), respectively. The charge distribution for the NAO analysis ranged from -0.841 to +0.841, whereas that for the NBO analysis ranged from -0.505 to +0.505. This finding is in agreement with previous findings (Demircioğlu et al., 2015). Additionally, both Fig. 4.29 (a) and (b) depict bond lengths, color-coded within a range of 1.081 to +1.773 Å. The total Lewis population for MB was 72.84 electrons, which accounted for 97.12% of the expected total. The valence non-Lewis population was recorded as 2.02 electrons, constituting 2.69% of the total electron count. Furthermore, the Rydberg non-Lewis population was 0.14 electrons, representing only 0.18% of the total. This demonstrates that the contribution from the Rydberg orbitals is minimal in the context of the electronic structure of MB in the ground state. The high percentage of the total Lewis population indicates that a substantial majority of the electrons in the molecule are engaged in bonding interactions, resulting in a stable electronic structure. The presence of a predominantly complete Lewis electron configuration suggests that MB has optimal electronic characteristics.

The NPA analysis of the MO dye revealed that the core population was 49.98 electrons, representing 99.97% of the expected total of 50 electrons. The valence population is quantified at 109.39 electrons, corresponding to 99.44% of the anticipated total (110 electrons). The natural minimal basis population is measured at 159.37 electrons, which is 99.61% of the expected total (160 electrons). The Rydberg basis population is reported at 0.63 electrons, constituting 0.39% of the total. The NPA data for MO illustrate a well-defined electronic structure characterized by high occupancy of core and valence electrons. This stability, coupled with the minimal contribution from Rydberg states, underscores the efficacy of MO as a dye in diverse applications, particularly in photonics, dye-sensitized solar cells, and chemical

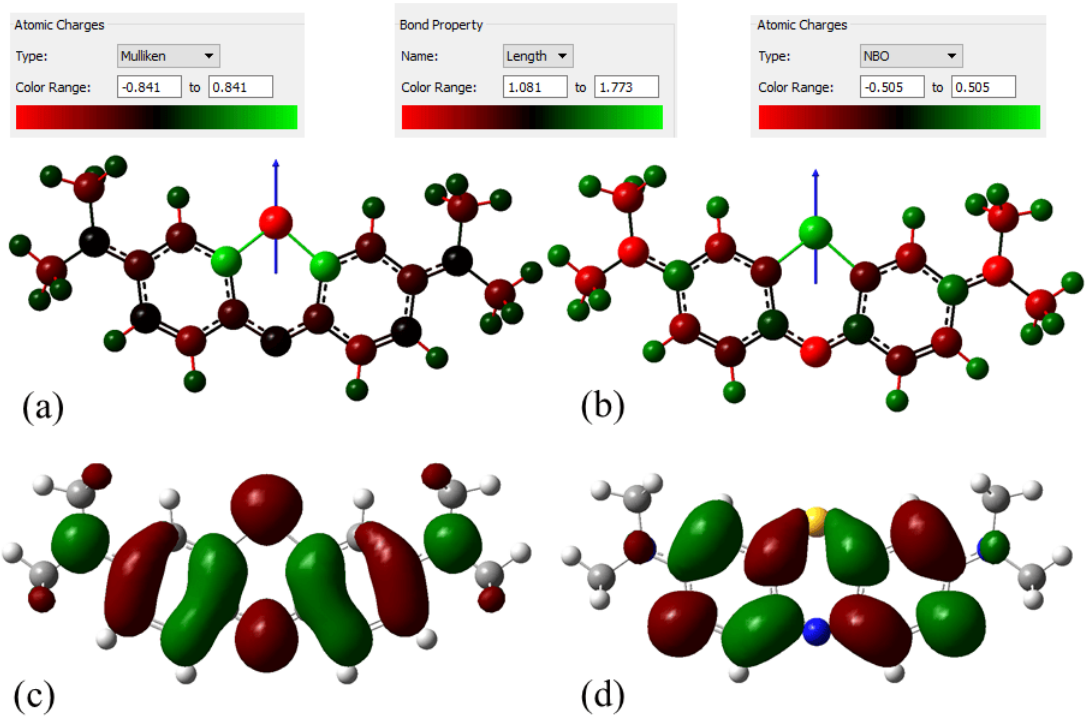

Figure 4.25: (a) Atomic charge distributions of MB of the Mulliken type (b) Atomic charge distribution by natural bond orbitals, (c) molecular orbital energy level of HOMO (d) molecular orbital energy level of the LUMO of the MB dye.

sensors. The optimized structure and atomic charge distributions of the MO dye, represented by NAO and NBO analyses, are illustrated in Fig. 4.26 (a) and (b), respectively. The charge distribution for the NAO analysis ranges from -0.659-+0.659, whereas that for the NBO analysis ranges from -2.253 - +2.253. Additionally, both Fig. 4.26 (a) and (b) depict bond lengths, color-coded within a range of 0.973 to +1.776 Å. The valence Lewis population was quantified at 104.95 electrons, corresponding to 95.41% of the anticipated total of 110 electrons, whereas the total Lewis population amounted to 96.83% of the expected total of 160 electrons. The valence of the non-Lewis population is reported to be 4.65 electrons, constituting 2.91% of the total. This small proportion indicates a limited number of nonbonding electrons, potentially including lone pair electrons. This near-complete occupancy reflects a well-defined bonding structure, suggesting that methyl orange is effectively represented by natural population analysis and indicating robust predictive capabilities for its chemical behavior. Furthermore, the Rydberg non-Lewis population is measured at 0.41 electrons, or 0.26% of the total. The minimal occupancy of Rydberg states suggests that the contributions from excited states are negligible underground state conditions. This finding indicates that the molecule primarily resides in a stable lower-energy configuration. The total non-Lewis population amounts to 5.07 electrons, accounting for 3.17% of the total population. This rel-

atively low value confirms that the electronic properties of methyl orange are predominantly governed by Lewis electrons, reinforcing its stability and reactivity. Similarly, the NPA of

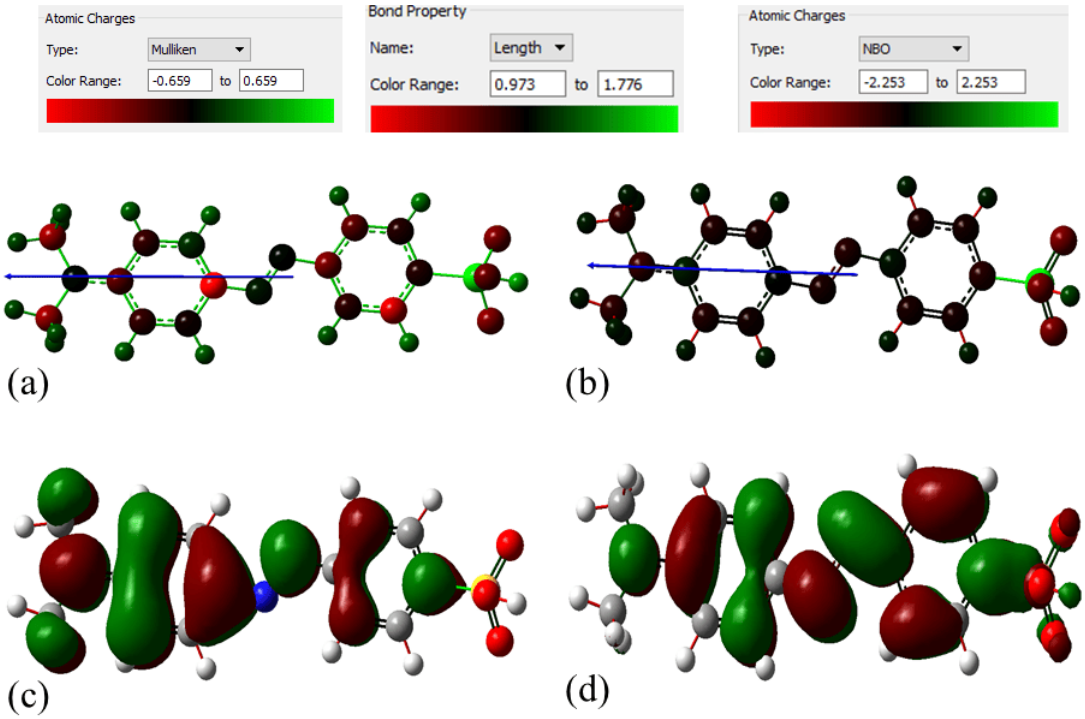

Figure 4.26: (a) Atomic charge distributions of the Mulliken type, (b) atomic charge distribution by natural bond orbitals, (c) molecular orbital energy level of the HOMO, and (d) molecular orbital energy level of the LUMO of the MO dye.

the MR dye core population accounted for 99.96% of 40 electrons, the valence population accounted for 99.64% of 102 electrons, the natural minimal basis population accounted for 99.73% of 142 electrons, and the Rydberg basis population accounted for only 0.27% of 142 electrons. The results indicate that MR dyes exhibit a well-defined electron distribution, with nearly complete core and valence populations, suggesting stability and significant involvement in bonding. The minimal contribution from the Rydberg state implies that the dye remains predominantly in its ground state, which is pertinent for understanding its chemical reactivity and properties. The optimized structure and atomic charge distributions of the MR dye, represented by NAO and NBO analyses, are illustrated in Fig. 4.27 (a) and (b), respectively. The charge distribution for the NAO analysis ranges from -0.598 - +0.598, whereas that for the NBO analysis ranges from -0.846 - +0.846. Additionally, both Fig. 4.27 (a) and (b) depict bond lengths, color-coded within a range of 0.986 to +1.492 Å. The total Lewis population is quantified at 137.86 electrons, representing 97.08% of the expected total. The valence of the non-Lewis population is 3.84 electrons, which corresponds to 2.70% of the total. This relatively small contribution indicates the presence of nonbonding electrons, likely

representing lone pairs that may influence the chemical reactivity and physical properties of the dye. Furthermore, the Rydberg non-Lewis population was measured at 0.30 electrons, accounting for 0.21% of the total. The high total Lewis population suggests that the MR possesses a stable electronic structure, which is advantageous for its performance as a dye. The significant presence of bonding electrons contributes to the stability and reactivity of dyes under various chemical conditions. The probability distributions of the charge density

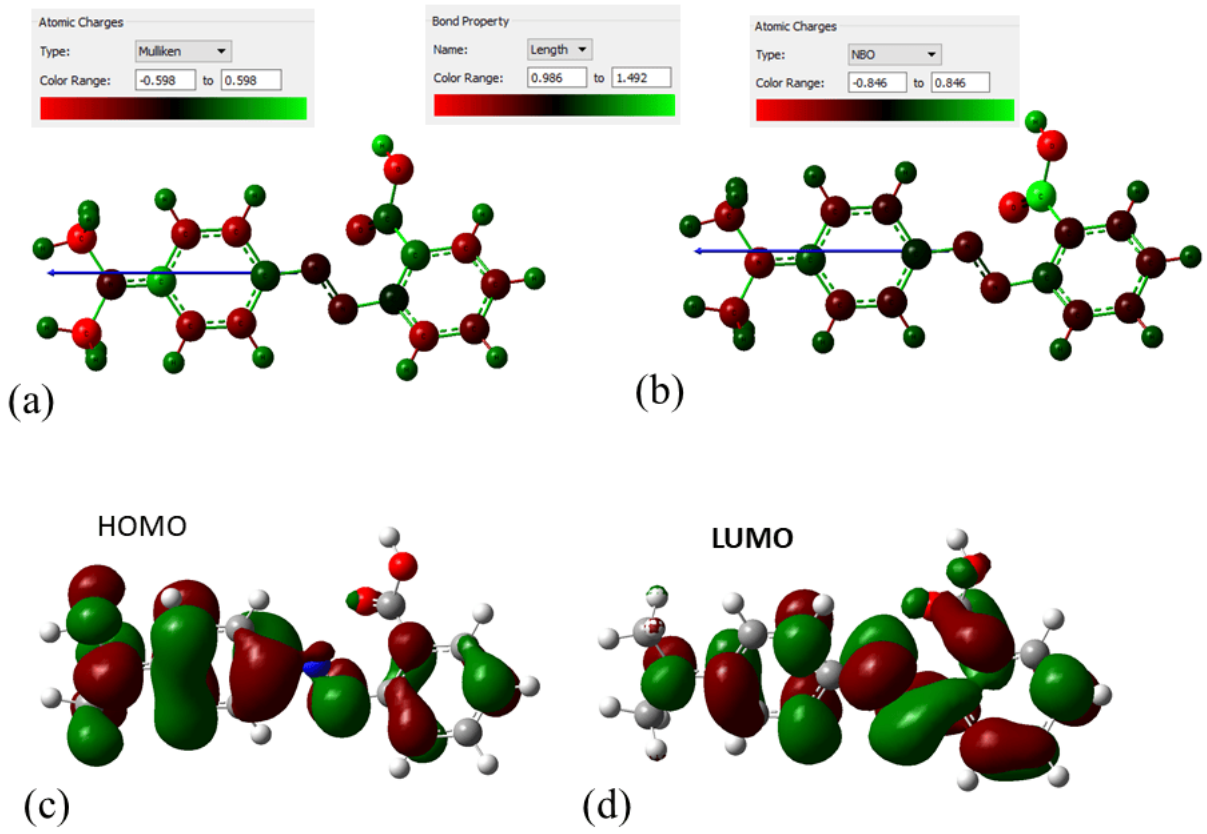

Figure 4.27: Atomic charge distributions of the Mulliken type, (b) atomic charge distribution by natural bond orbitals, (c) molecular orbital energy level of the HOMO, and (d) molecular orbital energy level of the LUMO of the MR dye.

and surface area fragmentation were analyzed via sigma (σ) profile calculations of MB, MO, and MR, as shown in Fig. 4.28. These (σ) profiles allow for quantification of the spatial distribution of the charge density, offering insights into the surface characteristics of the dyes. Furthermore, the analysis of the (σ) profiles aids in assessing surface area fragmentation, which helps evaluate how these properties affect the interaction dynamics and adsorption behavior of the compounds in different environments. The sigma profile of H_2O displays a broad distribution that indicates significant charge polarization. A prominent peak between σ = 0.014 and σ = 0.015 e/$\AA^2$is associated with the oxygen lone pairs and polar hydrogen atoms, whereas a peak at approximately σ = 0.001 e/$\AA^2$ reflects the characteristics of the

nonpolar surface region. Additionally, the peak at -0.015 e/$\mathring{A}^2$ is related to polar hydrogen atoms, emphasizing their role in hydrogen bonding. The peaks observed in the symmetric regions of the sigma profile underscore the stability and strength of the hydrogen bonds formed between water and other molecular entities, highlighting the critical role of the polar nature of water in facilitating intermolecular interactions. The sigma profile for MB is shown in Fig. 4.28 (b). The peaks at -0.005, -0.002, 0.005 and 0.01 correspond to different parts of the molecule, such as the nitrogen-containing aromatic groups and the sulfonate functional group. This finding is in agreement with previous findings Khnifiraa et al. (2020). These peaks reflect areas of high electron density, which are pivotal in determining the ability of a molecule to interact with electromagnetic radiation and facilitate electron transfer processes. Furthermore, the polar regions (such as where the ionic sulfonate groups are located) may show increased charge density, whereas nonpolar regions corresponding to the hydrocarbon-like components of the molecule may indicate lower electron density. The peaks at -0.006, -0.003, 0.004, and 0.009 in the sigma profile of MO in Fig. 4.28 (c) likely arise from the interactions between the functional groups and their surrounding electronic environment. The -SO_3H group is polar and contributes to specific charge density characteristics, which may correlate with the observed peaks in the sigma profile. Similarly, the peaks observed at -0.005, -0.002, 0.004, and 0.012 in the sigma profile MR dye in Fig. 4.28 (d) are typically associated with specific functional groups, such as azo groups (-N=N-) and aromatic rings. The electron-donating and electron-withdrawing characteristics of the azo group can affect the electron density distribution, leading to distinct peaks in the sigma profile. The presence of sulfonic acid groups also influences the charge distribution in the molecule. The contributions from the benzene rings in the MR structure can also result in characteristic peaks. The resonance stabilization within the aromatic systems may lead to localized electron density, contributing to the sigma profile peaks.

4.3.2 Bonding and antibonding interaction analysis

Second-order perturbation theory in the context of NBO analysis allows us to quantitatively assess donor–acceptor interactions, which are crucial in understanding molecular stability, reactivity, and properties in molecular systems. The analysis was carried out by examining all possible interactions between ”filled” (donor) Lewis-type NBOs and ”empty” (acceptor) non-Lewis NBOs. The chemical structure of MB, MO and MR dyes is portrayed in Fig. 4.29. The stabilization energy between the donor-acceptor interactions was calculated via Eq. (2.44). The stabilization energy of the N_3–C_{20} bond donors to the antibonding acceptor of C_5–C_{11} in the MB dye was calculated to be 4181.78 kcal/mol, indicating that the strongest interaction was observed. Similarly, the stabilization energy of the N3–C19 bond donors to the antibonding states of the C_5–C_{11} antibonding acceptor was calculated to be 994.84 kcal/mol. Furthermore, the stabilization energy of the C_6–C_{12} bond donors to the antibonding acceptor of C_5–C_{11} was calculated to be 739.20 kcal/mol. In addition, the de-

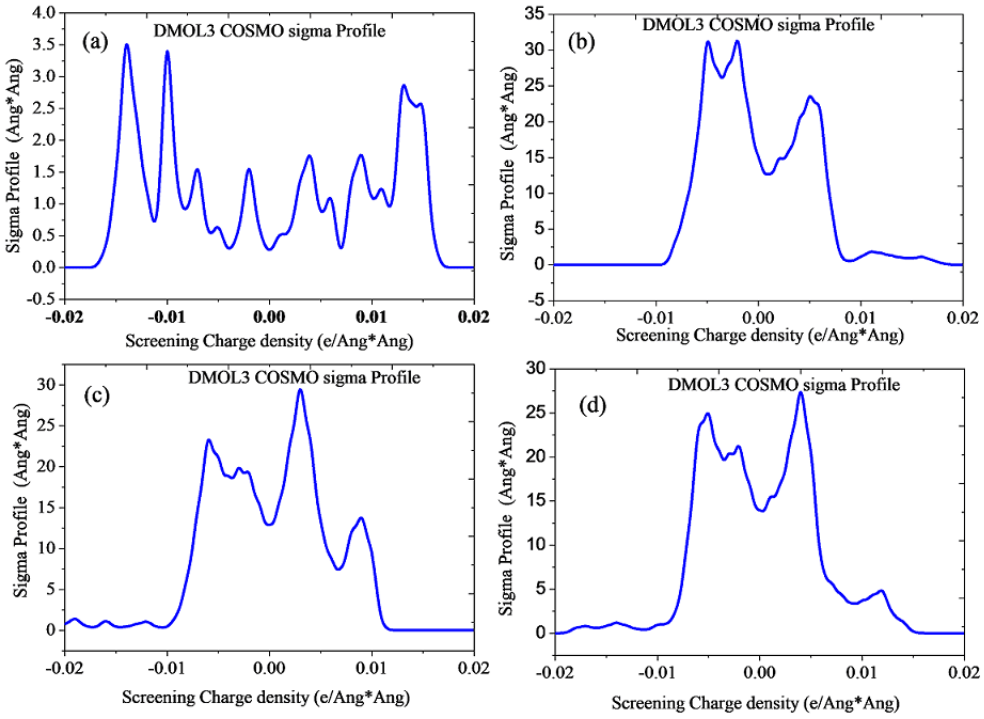

Figure 4.28: Sigma profile of (a) H_2O, (b) MB, (c) MO and (d) MR

localization of the MB dye involves interactions between the nitrogen and sulfur lone pairs. Specifically, powerful pi-type conjugative delocalization from the sulfur lone pair donors to the C_{12}-H_{22} antibonding acceptor was observed, with a stabilization energy of 1143.13 kcal/mol. Moreover, the interaction between the nitrogen lone pair and the antibonding state of C_{10} C_{12} is estimated to provide a stabilization energy of 27.60 kcal/mol. These findings are in agreement with a previous report Pembere et al. (2017).

The stabilization energies associated with various interactions in the MO dye were calculated, revealing significant insights into its electronic structure. The interaction between the bonding and antibonding states of the S_1-O_2 system and C_{21}-H_{35} yielded a stabilization energy of 17.85 kcal/mol. Additionally, the bonding interaction of N_7-C_{15} with the antibonding states of C_{21}-H_{35} resulted in a stabilization energy of 16.39 kcal/mol. A stronger interaction was observed between the bonding of C_{12}-C_{13} and the antibonding states of N_6-N_7, providing a stabilization energy of 30.74 kCal/mol. Furthermore, interactions between the nitrogen and oxygen lone pairs influenced delocalization in the MO dye, with the oxygen lone pair interacting with S_1-O_2 antibonding state and contributing 32.28 kcal/mol to stabilization. Notably, the interaction between the nitrogen lone pair and the antibonding state of C_8-C_9 resulted in the highest stabilization energy (55.68 kcal/mol). The interactions in the MR dye show significant stabilization energies between various atomic pairs. Specifically, the bonding interaction between N_4-N_5 and the antibonding states of C_{14} -C_{15} produces a stabilization

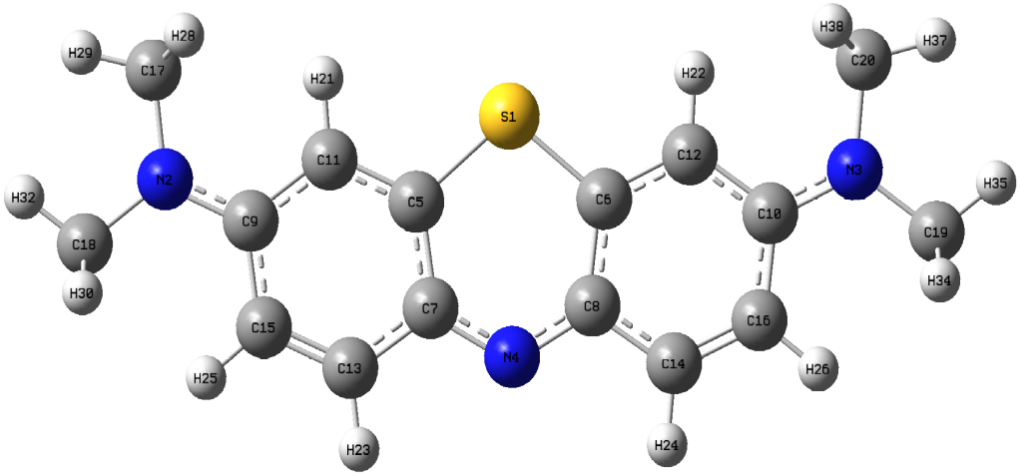

a)

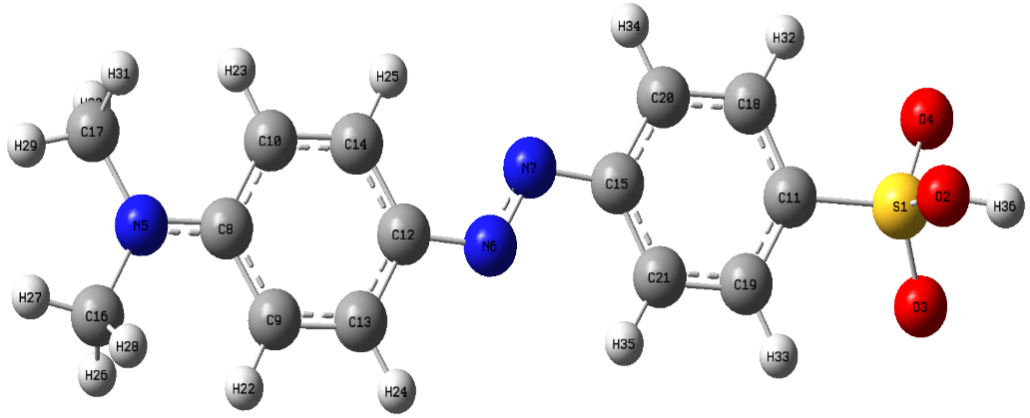

b)

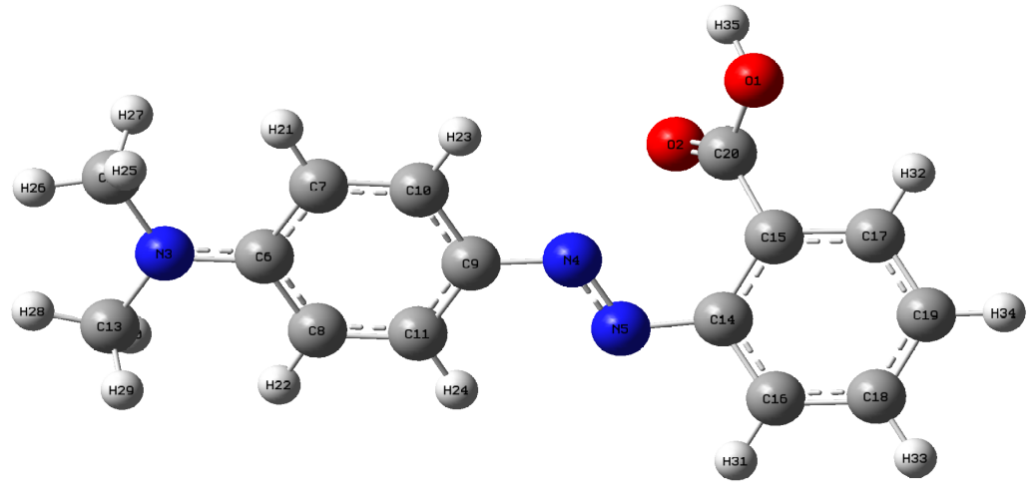

c)

Figure 4.29: Optimized molecular structure of (a) MB, (b) MO and (c) MR dyes

energy of 10.45 kcal/mol. The bonding of C_{14} -C_{15} with the antibonding states of C_{17} -C_{19} generates a stabilization energy of 21.41 kcal/mol. The interaction between C_{16}-C_{18} and the antibonding states of C_{14} -C_{15} provides a stabilization energy of 23.02 kcal/mol. Delocalization within the MR dye also involves interactions between lone pairs on the nitrogen, carbon, and oxygen atoms. The interaction between the lone pair of O_1 and the antibonding state of O_2-C_{20} yields a stabilization energy of 42.24 kcal/mol. The contribution of the nitrogen lone pair (N_3) to the antibonding state of N_4-N_5 is estimated to be 115.35 kcal/mol. Furthermore, the interaction between the (N_3) lone pair and the antilone pair state of C_6 results in the highest stabilization energy of 120.74 kcal/mol within the MR dye.

4.3.3 Quantum chemical descriptor analysis

Several quantum chemical descriptors have been used to analyze the chemical reactivity of MB, MO and MR dyes. The HOMO and LUMO structures of MB, MO and MR dyes are plotted in Fig. 4.25 (c, d), Fig. 4.26 (c, d), and Fig. 4.27 (c, d), respectively. The important electronic properties of the three dyes are summarized in Table 4.6. The results show that the HOMO energy levels of the dyes MB, MO, and MR were approximately -4.25, -5.70, and -5.53 eV, respectively. In contrast, the calculated LUMO energy levels for these dyes were approximately -2.65, -2.85, and -2.58 eV, respectively. Compared with the MO and MR dyes, the MB dye has higher E_{HOMO} values, which indicates a greater ability to donate electrons to the surface of the BiOCl crystal. The HOMO of MB is mainly localized on the nitrogen and carbon atoms of the nitrogen-containing aromatic rings, reflecting the electronic structure of the compound and its potential reactivity in various chemical environments. The LUMO of MB is predominantly localized on the carbon atoms, reflecting the electronic properties of the compound and its ability to participate in electron transfer processes. The carbon atoms contribute significantly to the HOMO for both the MO and MR dyes. Their involvement in resonance structures enhances electron density. In addition, the nitrogen atoms in aromatic rings are also key contributors. The delocalized π-electrons in these rings enhance the stability and reactivity of the HOMO. The nitrogen atoms in the azo group play a significant role in defining the LUMOs of the MO and MR dyes. The LUMO is also localized on the carbon atoms of the aromatic rings, involving a $\pi^{\star}$ character that allows for electron acceptance.

The energy difference between the HOMO and LUMO was calculated using Eq. (2.40) and its values for the MB, MO and MR dyes were 1.60, 2.65, and 3.26 eV, respectively. The results revealed that, compared with MO and MR dyes, MB has a smaller energy gap, which results in more electron donors. The χ was calculated via Eq. (2.41), and its values are 3.45, 4.44 and 3.95 eV for the MB, MO and MR dyes, respectively. This result shows that MO has the highest electronegativity and is likely to attract electrons more strongly than the other two dyes. This characteristic can enhance its reactivity, particularly in nucleophilic reactions. The η, which reflects the stability of the electronic structure, is 0.8 for MB, 1.33 for MO, and

Table 4.6: Calculated quantum chemical descriptors (electronegativity (χ), global hardness (η), global softness (S), electrochemical potential (μ) and global electrophilicity index (ω)) of different dyes

Dyes	E_{HOMO}(eV)	E_{LUMO}(eV)	ΔE_{gap} (eV)	χ	η	S	μ	ω
MB	-4.25	-2.65	1.60	3.45	0.8	1.25	-3.45	7.44
MO	-5.76	-3.11	2.65	4.44	1.33	0.76	-4.44	7.41
MR	-5.58	-2.32	3.26	3.95	1.63	0.61	-3.95	4.79

1.63 for MR. Higher values suggest that MO and MR are more thermodynamically stable and resistant to changes in electron density than MB. Consequently, MB is more chemically reactive than MO and MR on BiOCl crystals' surface. ω was calculated via Eq. (2.43) for the MB, MO, and MR dyes, and the values were 7.44, 7.41, and 4.79 eV, respectively. The ω for MB is greater than those for MO and MR. According to a previous report, dyes with a high electrophilic index are more likely to participate in electrophilic substitution reactions Cao et al. (2021). Consequently, this property facilitates electron transfer of the MB dye on the 001 surface of BiOCl crystals.

4.3.4 Quantum Theory of Atoms in Molecules and the Non-Covalent Interactions Analysis

We have calculated and analyzed the electron density topology of dyes using the Quantum Theory of Atoms in Molecules (QTAIM) and Non-Covalent Interactions (NCI) methods Cao et al. (2021). The analysis of electron density topology serves as a fundamental approach for identifying and classifying both inter- and intramolecular interactions within molecular systems Ji et al. (2022). QTAIM employs topological properties derived from electron density to identify and classify interactions. For the three dyes, three critical points were observed in QTAIM analysis. An atom critical point (3,-3) corresponds to the position of a nucleus in the molecular structure shown in a pink sphere and is characterized by a local maximum in electron density Gianopoulos et al. (2019). All bond critical points (3,-1) are shown in orange spheres for the three dyes in Fig. 4.30(a-c). A bond critical point is located along the bond path between two nuclei and signifies a local minimum in electron density. A ring critical point (3, 1) occurs at the center of a cyclic structure shown in a yellow sphere where there is a local minimum in the electron density within a plane defined by the atoms forming the ring Ji et al. (2022).

In particular, the NCI method allows for the visualization of non-covalent interactions by employing parameters derived from the electron density. The NCI isosurfaces for MB, MO, and MR, the non-covalent interactions, were computed using Multiwfn software. The plot of the 2D-RDG graph and the 3D isosurfaces of the NCI analysis for the three dyes are shown in Fig. 4.31 (a-f). The 2D-RDG graph shows three regions: (I) the Repulsive Interaction Region: In $\lambda_2 > 0$, the electron density is depleted. (II) Concentrated Electron Density Region; here $\lambda_2 < 0$ indicates the electron density concentration; (III) Weak van der

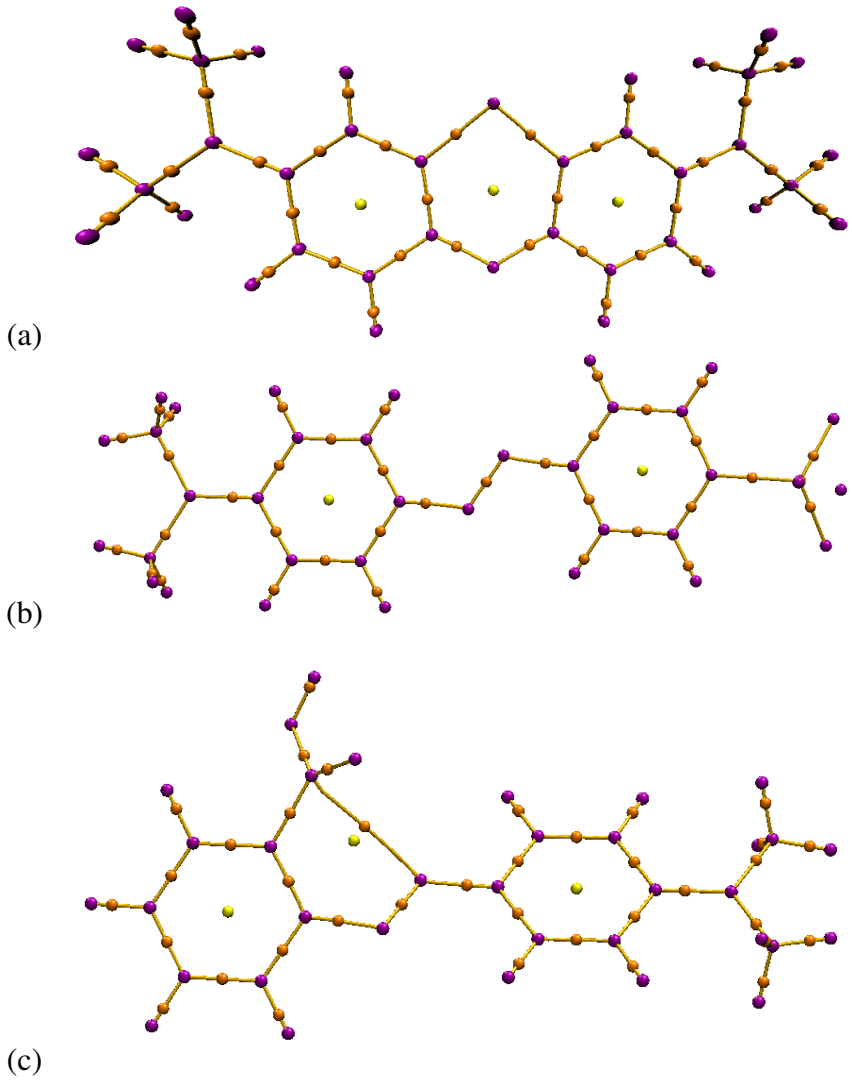

Figure 4.30: : QTAIM topology map of (a) MB, (b) MO and (c) MR dyes

Waals Interaction Region: This region corresponds to $\lambda_2 \approx 0$. This finding is in agreement with previous reports. Typically, higher RDG values suggest regions where the electron density changes rapidly, indicating possible covalent or strong non-covalent interactions. Regions with high RDG and negative (λ) values indicate strong attractive forces, whereas high RDG values with positive (λ) values imply repulsive forces or areas lacking significant stabilizing interactions Cao et al. (2021). The 3D isosurfaces of the NCI analysis confirmed the existence of non-covalent dispersive interactions in each dye.

Furthermore, the molecular electrostatic potential (MEP) maps of dyes were analyzed to identify the regions of nucleophilic and electrophilic character within a molecule, which can influence the reactivity, stability, and interaction with other molecular species Ji et al. (2022); Cao et al. (2021). The electrostatic potential energy per unit charge experienced by a positive test charge is placed in the vicinity of the dyes. This was derived from the electron density distribution calculated using quantum chemical methods. The MEP analysis of the MB dyes

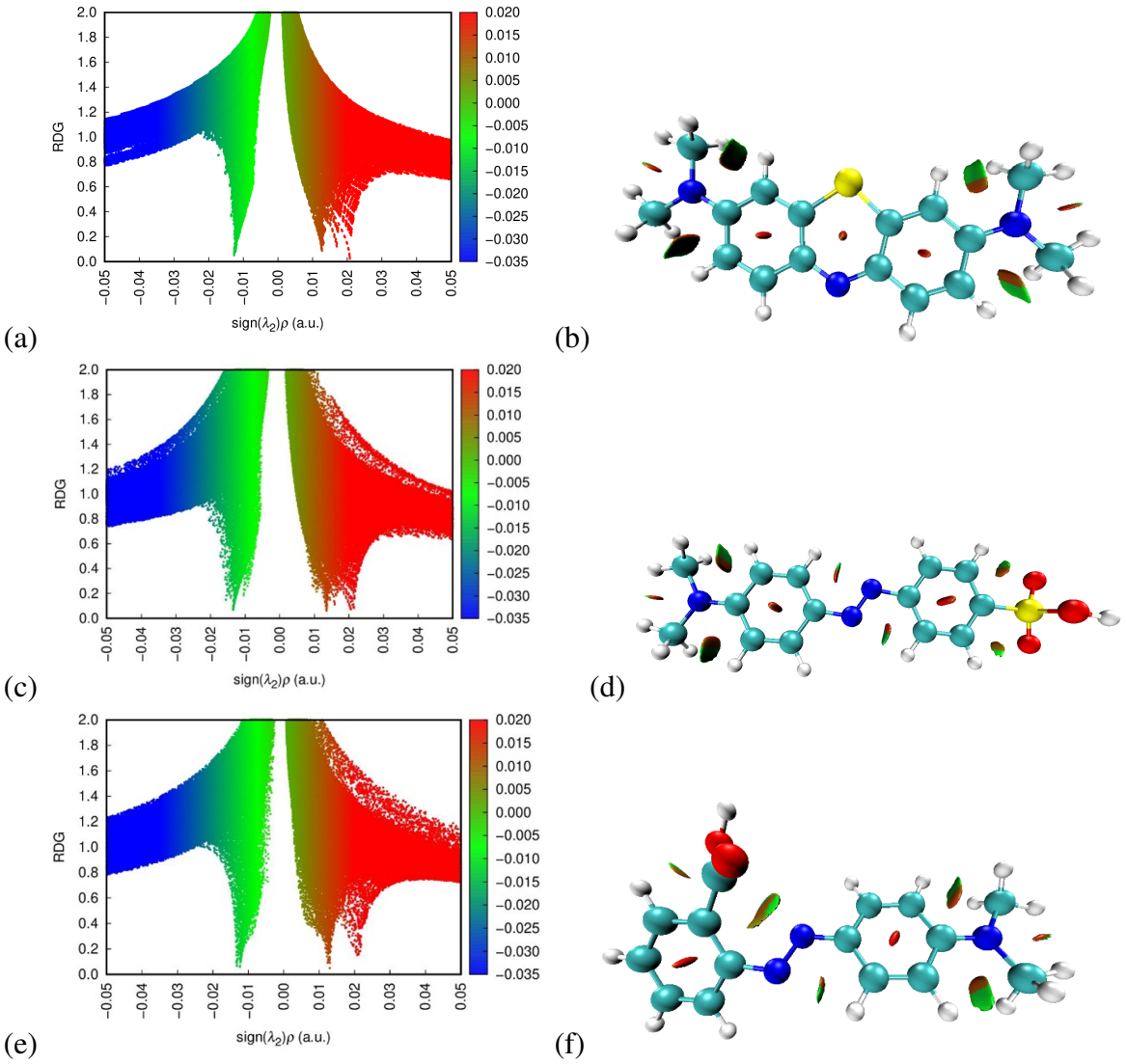

Figure 4.31: (a, c, e) 2D-RDG graphs and (b, d, f) NCI isosurfaces of MB, MO, and MR, respectively (where the green color indicates van der Waals interactions, red denotes strong non-bonded overlap or repulsive interactions, and blue highlights strong attractive interactions, including hydrogen bonds and electrostatic forces).

revealed regions of high electron density associated with the nitrogen atoms in the aromatic rings, indicating potential sites for electrophilic attack (Fig. 4.32(a)). The positive regions suggest strong interactions with the nucleophiles. Similarly, the MEP map in Fig. 4.32 (b) of the MO dyes shows distinct areas of negative potential near the azo group, making it a site for hydrogen bonding and interactions with positively charged species. This behavior indicates its role as a pH indicator. The MEP of the MR dye (Fig. 4.32 (c)) highlighted regions with varying potential values, indicating both nucleophilic and electrophilic sites. The presence of carboxylic acid groups contributed to a more complex electrostatic landscape compared to that of MB and MO.

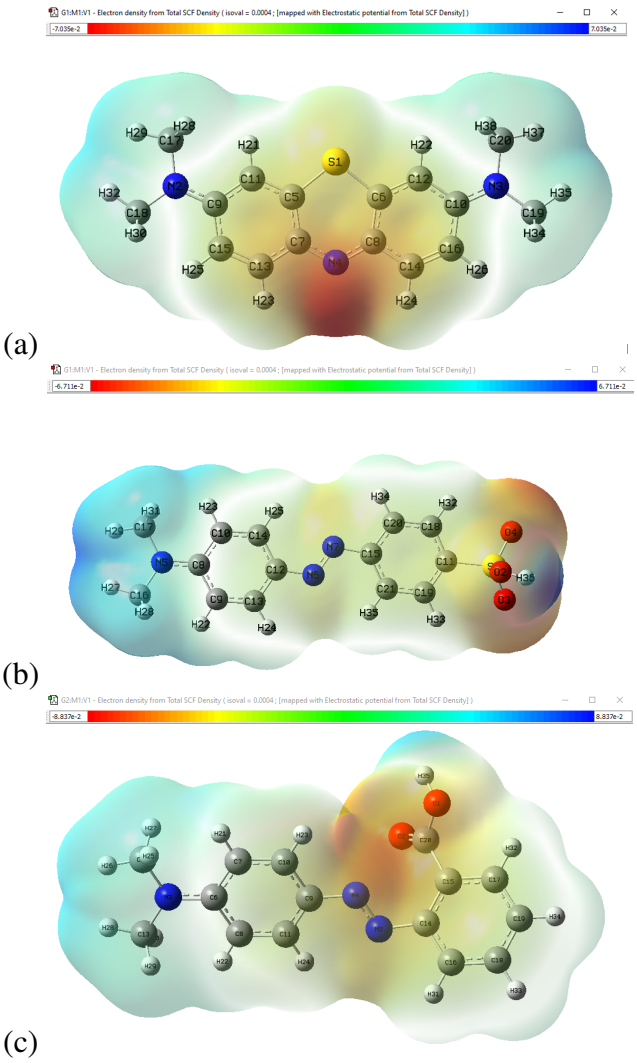

Figure 4.32: MEP map of (a) MB, (b) MO and (c) MR dyes

4.3.5 Molecular Dynamic Simulation Analysis

MCDS was performed to examine the adsorption behavior of various dyes on the BiOCl surface. The MCDS methodology effectively predicted the most favorable configurations for the adsorbed species at low-energy adsorption sites on the BiOCl surface. Figure 4.33 (a, b, c) shows the MCDS model for the system under study. For the complex systems analyzed, which incorporated 100 H_2O molecules to account for solvent effects, different types of energies were calculated. These energy values are the total energy, adsorption energy, rigid adsorption energy(E_{RAE}), deformation energy (E_{def}) and differential adsorption energy ($\frac{dE_{RAE}}{dN_i dye}$). The calculated energies obtained from the adsorption locator module are summarized in Table 4.8. The adsorption energies of MB, MO and MR are -70.82, -89.34 and -60.55 kcal/mol, respectively. MO has a greater absorption energy than MB and MR and is much more attracted than MB and MR are on the surface of the BiOCl crystal. Furthermore, MO dye is a more stable system consisting of a substrate-adsorbate pair, indicating stronger adsorption characteristics. For all dyes, the differential adsorption energy value is

equivalent to the adsorption energy of the system, as there is only one sorbate present in each system. The current findings are in agreement with those of a previous study Khnifiraa et al. (2020).

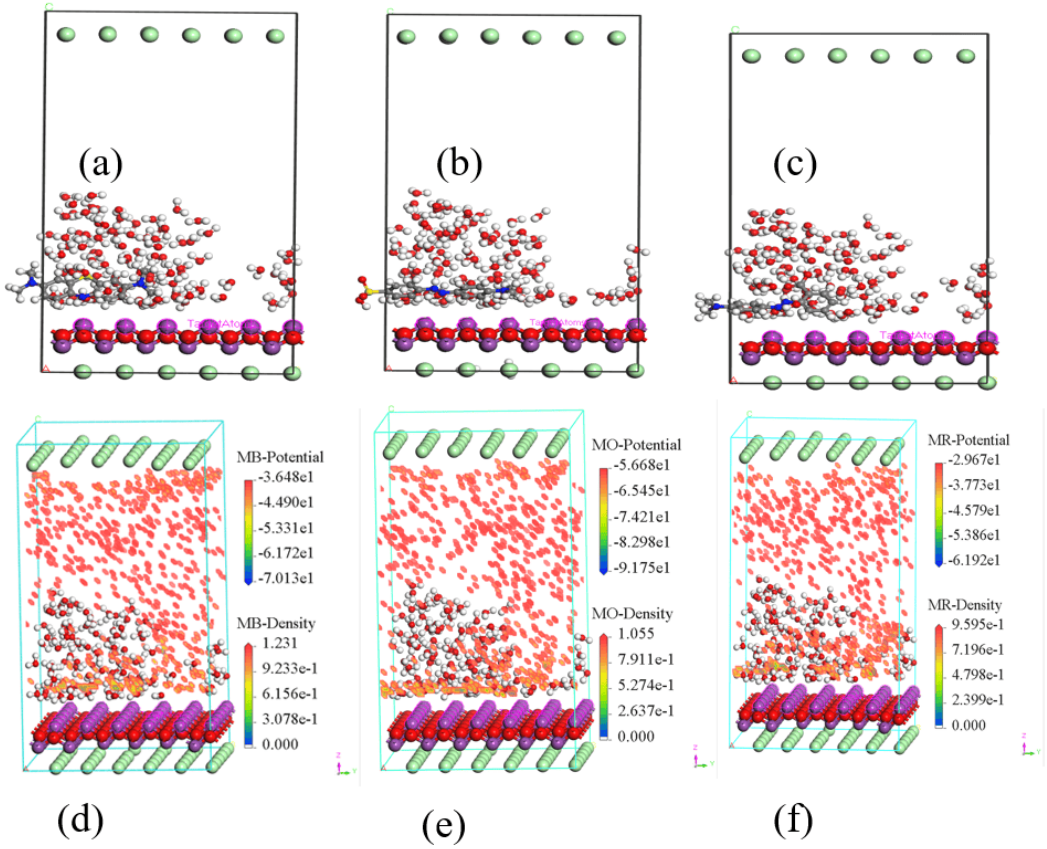

Figure 4.33: Complex structure of (a) BiOCl/MB/H_2O, (b) BiOCl/MO/H_2O, (c) BiOCl/MR/H_2O and (b, d, f) distributions of the charge density and potential of the MB, MO and MR dye adsorption sites respectively

Figure 4.33 (d, e, f) shows the electrostatic potential and charge density of MB, MO and MR, respectively. Regions with high charge density coupled with low electrostatic potential are prime candidates for adsorption, suggesting that these areas can effectively attract and stabilize adsorbates. The energy distributions among the van der Waals, total, electrostatic, average total, and intermolecular energies in the MB, MO and MR dyes obtained from the adsorption locator module are shown in Fig. 7 (a-c).

Table 4.7: Outputs and descriptors calculated via Monte Carlo simulation for the adsorption of the forms of dyes studied on the BiOCl surface (kcal/mol).

Complex	E_{tot}	E_{ads}	E_{RAE}	E_{def}	$\frac{dE_{ads}}{dE_{dye}}$
BiOCl/MB/H_2O	16.40	-70.82	-34.60	-36.22	-70.82
BiOCl/MO/H_2O	94.06	-89.34	-33.34	-56.00	-89.34
BiOCl/MR/H_2O	8.45	-60.55	-32.56	-27.99	-60.55

4.4 Experimental Results Analaysis

In this section, the results of various characterization techniques used to understand the structural, optical, and morphological properties of pure BiOCl and Sn-doped BiOCl crystal was discussed.

4.4.1 XRD Analysis

The crystallinity and phase purity of the prepared samples were examined by XRD analysis. Figure 4.34 illustrates the XRD pattern of pure BiOCl and Sn-doped BiOCl samples. The most intense peaks in terms of 2θ values were identified for the BiOCl sample at angles of 25.92°, 32.58°, and 33.49°; for 1% Sn-doped BiOCl at 26.10°, 32.80°, and 33.61°; for 3% Sn-doped BiOCl at 25.94°, 32.63°, and 33.47°; and for 5% Sn-doped BiOCl at 32.64°, 25.94°, and 33.47°, which correspond to planes (101), (110) and (102) respectively. The crystal structure of the BiOCl sample has space group P 4/n mm (129) and cell parameters of a = 3.887 Å, c= 7.354 Å. All diffraction peaks were well indexed to the standard tetragonal phase of BiOCl (JCPDS: 96-900-8427) (COby, 1993).

The pattern exhibits sharp peaks, indicating high crystallinity of the prepared samples. Notably, a slight shift in the positions of the most intense peaks was for Sn-doped samples. The average crystalline size of undoped BiOCl and Sn-doped BiOCl samples was determined from the intense peak using the classical Debye-Scherrer equation. The results reveal that all prepared samples are nanoscale in size, with decreased crystalline sizes observed with Sn doping. The decrease in crystalline size due to Sn doping suggests that the doping process influences crystal growth and morphology. Moreover, the lattice parameters exhibited a small change with Sn doping, particularly demonstrating a decrease in unit volume for all Sn-doped BiOCl samples, indicating a contraction of the unit cell. The changes in lattice parameters, particularly the contraction observed in Sn-doped BiOCl, may be attributed to the incorporation of Sn ions into the BiOCl structure, potentially resulting in local distortions and changes in unit cell dimensions.

The XRD results show that Sn doping affects the structural properties of BiOCl, including its crystal structure, crystalline size, and lattice parameters. The findings are consistent with previous research by (Zulkiflee et al., 2023b,c). These changes may have an impact on the properties of the material, such as its optical, electronic, or catalytic characteristics.

4.4.2 TEM Analysis

Figure 4.35 shows TEM images of both pure BiOCl and Sn-doped BiOCl samples, demonstrating a layered nanosheet morphology. This layered structure is essential for the unique electronic and optical properties of these materials. The crystal structure of all samples has a tetragonal crystal structure as shown in Fig. 4.36 (a-d), which agrees with the XRD result. The d-spacing values were calculated using ImageJ software. Figure 4.36 (a-d) also shows a magnified section of the TEM image to display the d-space of each sample. The study re-

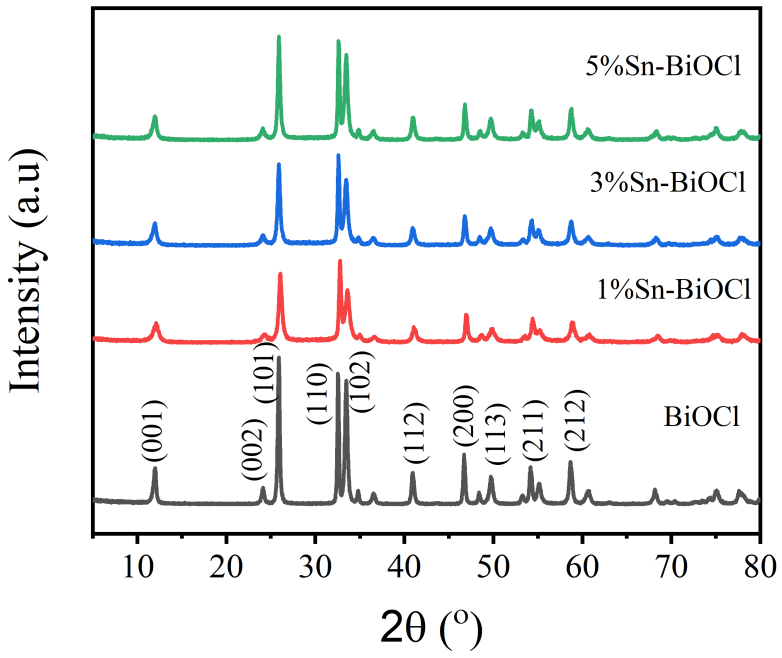

Figure 4.34: XRD pattern pure BiOCl and Sn-BiOCl crystal with different concentrations

Table 4.8: The crystalline size, lattice parameters and energy band gap of BiOCl and Sn-doped BiOCl determined from experiment.

Samples	Crystalline size (nm)	Lattice Parameters (nm)		Volume (A3)	$E_g(eV)$
		a=b	c		
BiOCl	32.76	3.887	7.354	111.11	3.20
1%Sn-BiOCl	21.30	3.860	7.270	108.32	3.15
3%Sn-BiOCl	26.62	3.878	7.362	110.72	3.05
5%Sn-BiOCl	27.48	3.876	7.359	110.56	3.10

ports a d-spacing of 0.496 nm for pure BiOCl, with progressively decreasing values of 0.420 nm, 0.372 nm, and 0.138 nm for 1%, 3%, and 5% Sn-doped BiOCl, respectively. Similar findings can be found in the report by (Zulkiflee et al., 2023b,c; Long et al., 2022). The findings indicate that Sn doping alters the structural properties of BiOCl, as the reduction in d-spacing suggests effective incorporation of Sn atoms into the BiOCl lattice, which may enhance structural stability and modify electronic characteristics. The observed reduction in d-spacing implies that the introduction of Sn may cause lattice contraction, likely related to the smaller ionic radius of Sn compared to Bi. This result aligns with the lattice parameter calculations derived from DFT results. Variations in lattice parameters can significantly affect charge carrier mobility and optical properties, which are critical for applications in photocatalysis and semiconductor devices.

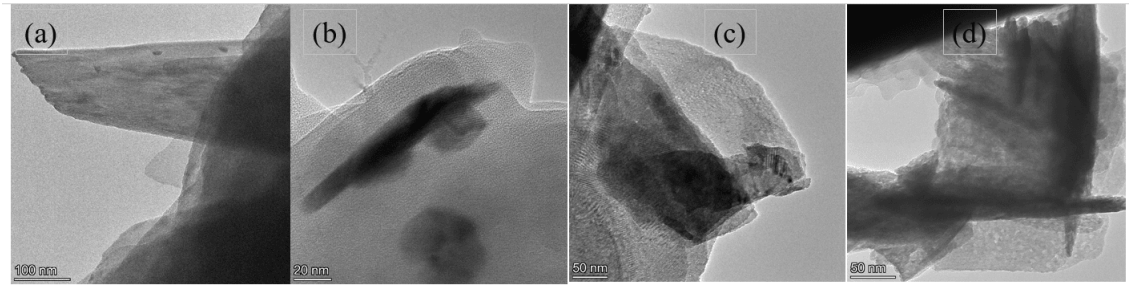

Figure 4.35: TEM image of (a) pure BiOCl, (b) 1% Sn-BiOCl, (c) 3% Sn-BiOCl and (d) 5% Sn-doped BiOCl crystal strucure.

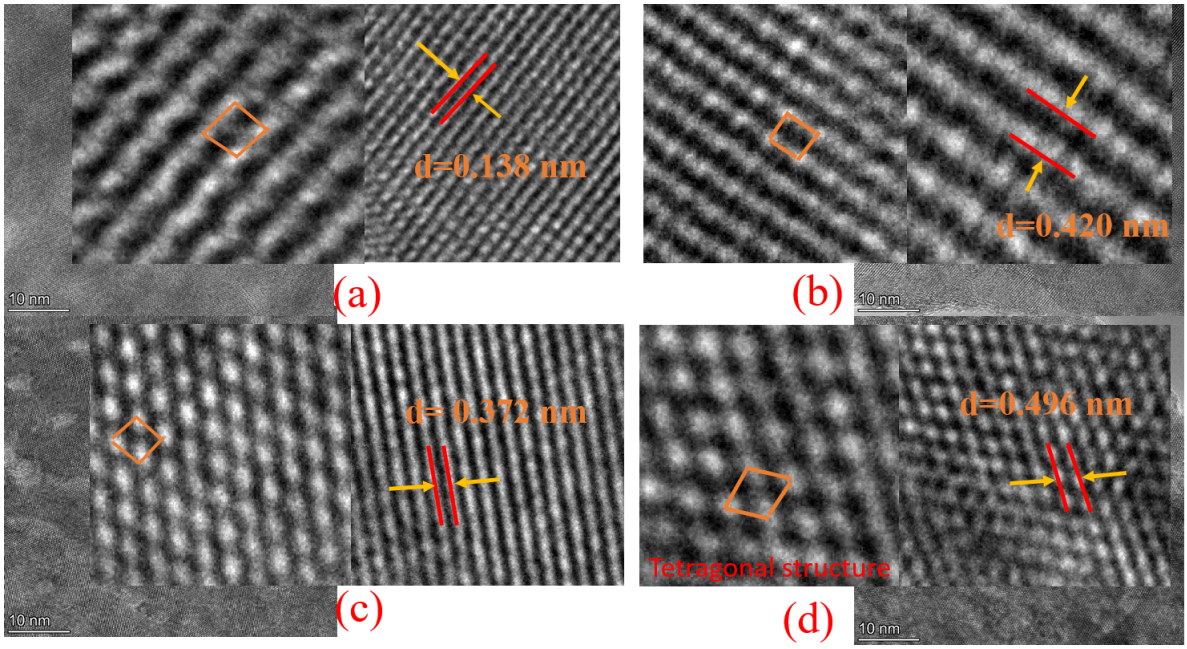

Figure 4.36: TEM image of (a) pure BiOCl, (b) 1% Sn-BiOCl, (c) 3% Sn-BiOCl and (d) 5% Sn-BiOCl: The tetragonal structure and the inter-particle distance.

4.4.3 FTIR Analysis

To elucidate the atomic bonding structure of BiOCl and Sn-doped BiOCl, FTIR was employed to identify the chemical bonds present in BiOCl molecules. As illustrated in Fig. 4.37, the FT-IR spectra of a pure BiOCl sample exhibit a peak at 525 cm^{-1} attributable to Bi-O stretching. In contrast, multiple peaks were observed in the case of Sn-doped BiOCl. The absorption peaks for 3%Sn-BiOCl and 5%Sn-BiOCl crystals are evident at 1220, 1375, 1735, and 3020 cm^{-1}. The peaks at 1220 and 1375 cm^{-1} may be attributed to the asymmetric and symmetric stretching of Bi-Cl and Sn-Cl, while the peak at 3020 cm^{-1} is associated with O-H stretching in free water. The introduction of Sn atoms into the BiOCl lattice can induce changes in the vibrational frequencies and intensity of the observed infrared (IR) bands.

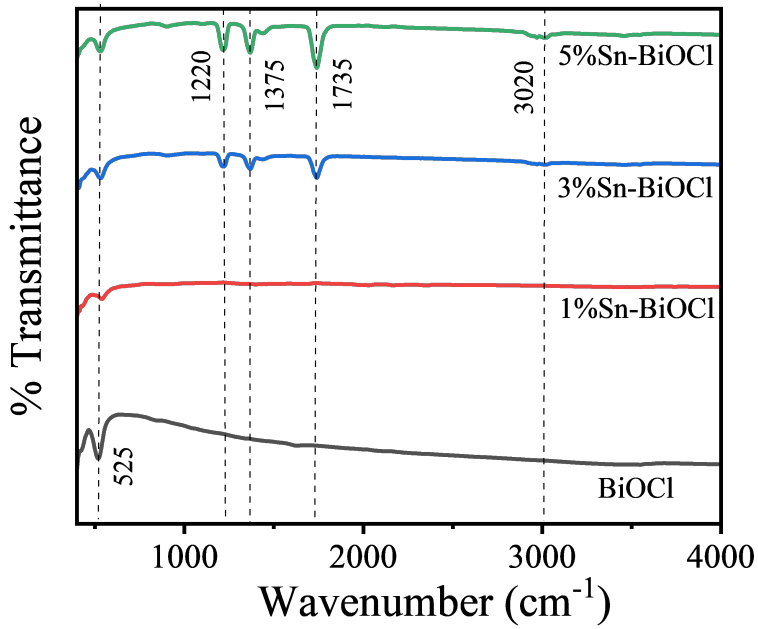

Figure 4.37: FTIR spectra of pure BiOCl and Sn-BiOCl crystal with different concentrations

4.4.4 UV-Vis Analysis

UV-VIS spectroscopy is a powerful analytical technique utilized to investigate the optical properties of materials. The Sn-doped samples exhibit a red shift in the absorption edge as demonstrated in Fig. 4.38 (a), extending into the visible light region. This shift can be attributed to the reduced band gap energy resulting from Sn incorporation, which alters the electronic structure of BiOCl. The optical band gap of samples was calculated using diffuse reflectance spectroscopy using the Kubelka–Munk function. The energy band gap calculated from the Tauc plot for pure BiOCl, 1%Sn-BiOCl, 3%Sn-BiOCl, and 5% Sn-BiOCl is 3.20, 3.15, 3.05, and 3.10 eV respectively, as shown in Fig. 4.39 (a-d). The result reveals that the energy band gap for doped BiOCl is reduced compared with the pure BiOCl samples. This observation is the same as the computational findings. Doping creates an additional energy level within the band gap, which can facilitate electron transitions and enhance light absorption. The intensity of absorption in the visible region increases with Sn doping. This enhancement indicates improved light harvesting capabilities, which is crucial for photocatalytic applications.

4.4.5 PL Analysis

Photoluminescence (PL) analysis is a critical technique employed to investigate the processes of electron-hole recombination and separation in semiconductor materials, as well as to examine surface defects. In this study, the PL spectra of pure BiOCl and Sn-doped BiOCl samples (1%, 3%, and 5% Sn) were recorded over a wavelength range of 350 to

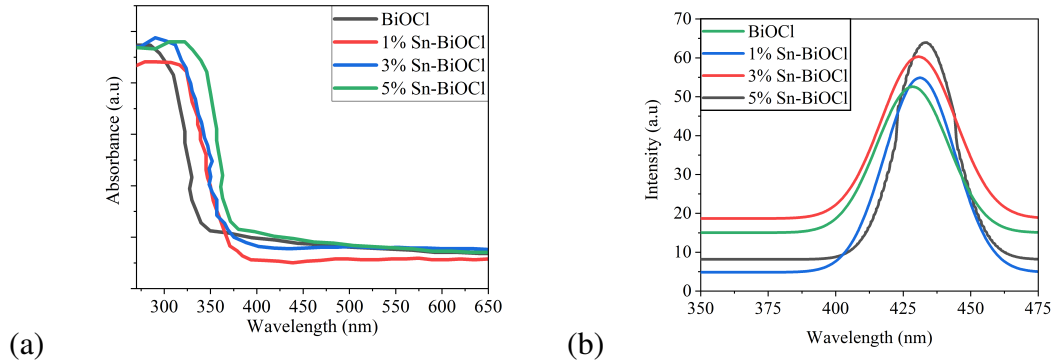

Figure 4.38: (a) UV–Vis absorption spectra, (b) PL spectra of pure BiOCl and Sn-doped BiOCl with different concetrations

475 nm, utilizing an excitation source of 255 nm, as illustrated in Fig. 4.38 (b). The PL spectra indicated that the peak positions remained relatively consistent across the different samples, suggesting that the fundamental electronic transitions within the BiOCl lattice were preserved despite the introduction of Sn dopants. This consistency in peak positions is indicative of the retention of the material's crystalline structure upon doping. Furthermore, a notable enhancement in emission intensity was observed with increasing Sn concentration. This increase can be attributed to the presence of Sn elements within the Sn-doped BiOCl crystal. These dopants can serve as effective electron traps, facilitating the recombination processes and thereby enhancing the luminescence properties of the material. This result indicates that the optical properties of 1%, 3%, and 5% Sn-doped BiOCl were enhanced due

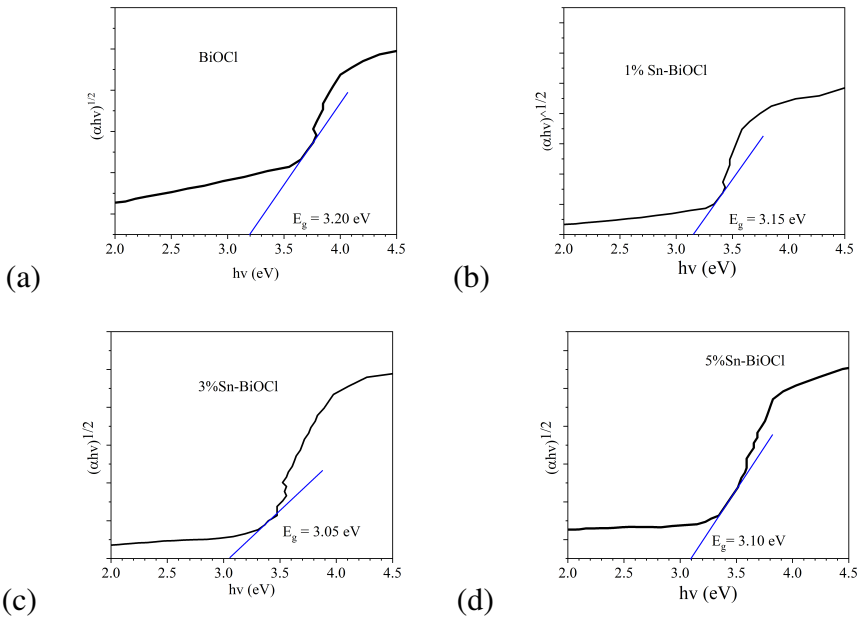

Figure 4.39: Energy band of pure and Sn-doped BiOCl with different concentrations plotted using Tauc's plot

to the effective incorporation of Sn into the structure. The finding is in agreement with the literature (Zulkiflee et al., 2023b; Long et al., 2022).

5

Conclusions and Recommendations

5.1 Conclusions

In conclusion, the studies have elucidated the multifaceted properties of BiOX crystals, emphasizing their potential in photocatalytic applications. Comprehensive analyses of electronic structure, phonon dynamics, optical characteristics, and temperature-dependent thermodynamics reveal that BiOI is the most promising candidate due to its exceptional optical properties, including a high static dielectric constant and refractive index. These attributes facilitate enhanced light-matter interactions and effective charge separation, both of which are critical for photocatalytic efficiency. The first-principles calculations confirm the dynamic stability of BiOX crystals. The Raman and infrared spectral analyses reveal characteristic vibrational modes, such as Bi-O bond vibrations and lattice vibrations, which are essential for understanding the material's vibrational dynamics. Thermodynamic evaluations indicate that the heat capacity remains stable at high temperatures.

The effects of post-transition metal doping on the electronic structure and optical properties of BiOCl crystals demonstrate that substitutions bring changes in the electronic structure of doped BiOCl. The calculated energy band gap for In-, Sn-, and Tl-doped BiOCl are 2.59 eV, 2.35 eV, and 2.54 eV, respectively, all smaller than that of pure BiOCl (2.80 eV). The doped BiOCl has an absorption peak in the low-energy region, which indicates enhanced light absorption capabilities. The density of states analysis underscores the shift in valence band components due to doping, confirming that post-transition metal integration impacts the electronic and optical properties of doped BiOCl.

The study of tin doping and co-doping with bromine also confirms the electronic structure of co-doped BiOCl changed. The calculated electronic band structure of pure, doped co-doped crystals has an indirect band gap structure. The increased static dielectric constant in doped systems indicates a robust binding affinity of dopants to electrons, thereby prolonging the lifespan of photogenerated charge carriers and augmenting photocatalytic activity. The molecular interaction and dye adsorption analysis result shows that BiOCl is an excellent adsorbent for dye removal from wastewater. The calculated adsorption energies indicate a strong affinity of methylene orange (MO) for the BiOCl surface, further estab-

lishing BiOCl as a superior photocatalytic and adsorption material. Overall, this study not only reinforces the viability of BiOX and BiOCl crystals in photocatalytic applications but also opens avenues for their use in environmental remediation strategies, paving the way for future research and development in sustainable material science.

The X-ray diffraction (XRD) patterns of the synthesized samples were aligned well with the standard tetragonal structure, suggesting a significant level of crystallinity. All synthesized samples were of nanoscale dimensions, with a marked reduction in size noted in the tin (Sn)-doped variants. The XRD outcomes imply that Sn incorporation affects the structural traits of BiOCl crystals. Transmission electron microscopy (TEM) analysis indicated that the samples are composed of nanosheets displaying layered morphologies. The calculated d-spacings between lattice planes were 0.496 nm, 0.420 nm, 0.372 nm, and 0.138 nm for BiOCl, 1% Sn-BiOCl, 3% Sn-BiOCl, and 5% Sn-BiOCl, respectively. Ultraviolet-visible (UV-Vis) spectroscopy revealed that Sn doping effectively reduces the energy band gap of the doped samples as compared to pure BiOCl. Furthermore, the absorption intensity of the Sn-doped samples showed a redshift. Photoluminescence (PL) analysis also demonstrated that Sn doping extends the excitation lifetime of the doped samples relative to pure BiOCl. To sum up, both computational and experimental analyses indicate that doping substantially enhances the electronic and optical properties of BiOCl.

5.2 Recommendations

The exploration of post-transition metal-doped BiOX materials represents a promising avenue for enhancing photocatalytic activities. To foster future research and applications, the authors recommend the following strategies:

- Investigate the dynamics of charge carriers in BiOX, focusing on their transport mechanisms, lifetimes, and interactions.
- Test the photocatalytic activity of In/Sn/Tl-doped and Br co-doped for different organic pollutants degradation.
- Explore BiOX-based heterostructures and modifications that enhance electron mobility and efficiency for applications in photovoltaics and photocatalysis.

List of Publications

Throughout my PhD studies, I have authored and co-authored several articles, detailed below.

A. Published Articles, Under review and prepared Manuscripts

1. **Tadesse Lemma Wakjira**, Kumneger Tadele, Abebe Belay Gemta and Gashaw Beyene Kassahun: Electronic, optical, phonon, and thermodynamic properties of bismuth oxyhalides for photocatalysis application using density functional theory: October 2024 **Discover Materials** 4(1) DOI: 10.1007/s43939-024-00131-4.

2. **Tadesse Lemma Wakjira**, Kumneger Tadele, Abebe Belay Gemta and Gashaw Beyene Kassahun: Effect of tin doping and tin-bromine co-doping on electronic and optical properties of BiOCl crystal: density functional theory. June 2024 **Materials Research Express** 11(6), DOI: 10.1088/2053-1591/ad549c

3. **Tadesse Lemma Wakjira**, Abebe Belay Gemta, Gashaw Beyene Kassahun, Dinsefa Mensur Andoshe and Kumneger Tadele. Bismuth-Based Z-Scheme Heterojunction Photocatalysts for Remediation of Contaminated Water. February 2024 **ACS Omega** 9(8) DOI: 10.1021/acsomega.3c08939.

4. **Tadesse Lemma Wakjira**, Abebe Belay Gemta, Kumneger Tadele, Gashaw Beyene Kassahun, Umer sherefedin, Gurumurthi T and Tesfaye Feyisa: Molecular structures and adsorption of dyes on bismuth oxychloride surfaces using density functional theory and Monte Carlo dynamic simulation: First revision is Submitted (**Results in Physics**, Elsevier publisher).

5. **Tadesse Lemma Wakjira**, Abebe Belay Gemta, Kumneger Tadele, Gashaw Beyene Kassahun and Umer sherefedin: Exploring Sn-Doping: Unraveling the Electronic and Optical Properties of BiOCl through Experimental and Computational Synergy. (**prepared manuscript**)

B. Others published and under review Articles

1. Umer Sherefedin, Abebe Belay, Kusse Gudishe, Alemu Kebede, Alemayehu Getahun Kumela, **Tadesse Lemma Wakjira**, Semahegn Asemare, T Gurumurthi and Dereje Gelanu: Investigating the effects of solvent polarity and temperature on the molecular, photophysical, and thermodynamic properties of sinapic acid using DFT and TDDFT. July 2024RSC Advances 14(32):23364-23377, DOI: 10.1039/D4RA04829F.

2. Umer Sherefedin, Abebe Belay, Kusse Gudishe, Alemu Kebede, Alemayehu Getahun Kumela, **Tadesse Lemma Wakjira**, Semahegn Asemare, T. Gurumurthi. Effects of

Temperature and Solvent Polarity on the Thermodynamic and Photophysical Properties of Ferulic Acid Using Density Functional Theory (DFT). June 2024 Journal of Molecular Liquids 407:125175, DOI: 10.1016/j. molliq.2024.125175.

3. Umer Sherefedin, Abebe Belay, Kusse Gudishe, Alemu Kebede, Alemayehu Getahun Kumela, **Tadesse Lemma Wakjira,** Dereje Gelanu, Tesfaye Feyise, Jebel Haji Mahamud, Abdulkerim Abdela, Kebede Shankute Gizew: DFT and Molecular Docking Analyses of the Effects of Solvent Polarity and Temperature on the Structural, Electronic, Thermodynamic Properties, and Binding Affinity of P-Coumaric Acid: For Anti-Cancer Applications: **Accepted manuscript** (in production) Results in physics.

4. Tesfaye Feyisa, Abebe Belay, Fekadu Tolessa, Umer sherefedin, Manza Zityab, Bereket Dalga, Melak Birara, **Tadesse Lemma**: Near Infrared Thermal Emitter Based On Nano Scale Grating Metamaterial For Thermo Photovoltaic Power Generation: (First Revision @ Physica scripta; Manuscript ID: PHYSSCR-135395. R1).

5. Mulgeta Girma, **Tadesse Lemma Wakjira**, Kedir Hussien, Kumneger Tadele, and Seyfan Kelil: The electronic structure and performance analysis of pentagraphene based Thermoelectric generator: Manuscript ID: ADV24-AR-04749 (under revision).

List of Conference Participation and Paper Presentation

1. Certificates of participation on Workshop on Classical and Quantum Machine Learning for Condensed Matter Physics 19-21 June, 2024, organized by ICTP and BRIN.

2. Certificates of participation in the Science Talk on Photophysics of Skin Pigment Melanin on June 25, 2024, organized by ACS Sciences Talks.

3. Certificates of research paper Presentation February 17, 2024 on 18^{th} Annual Conference of the Ethiopian Physical Society, held at Addis Ababa University.

4. Certificates of participation on 18^{th} Annual Conference of the Ethiopian Physical Society, held at Addis Ababa University, held from February 17-18, 2024.

Bibliography

AlMohamadi, H., Awad, S. A., Sharma, A. K., Fayzullaev, N., Távara-Aponte, A., Chiguala-Contreras, L., Amari, A., Rodriguez-Benites, C., Tahoon, M. A., and Esmaeili, H. (2024). Photocatalytic activity of metal-and non-metal-anchored zno and tio2 nanocatalysts for advanced photocatalysis: Comparative study. *Catalysts*, 14(7):420.

Andrade, P. H., Volkringer, C., Loiseau, T., Tejeda, A., Hureau, M., and Moissette, A. (2024). Band gap analysis in mof materials: Distinguishing direct and indirect transitions using uv–vis spectroscopy. *Applied Materials Today*, 37:102094.

Aneyo, I. A., Doherty, F. V., Adebesin, O. A., and Hammed, M. O. (2016). Biodegradation of pollutants in waste water from pharmaceutical, textile and local dye effluent in lagos, nigeria. *Journal of Health and Pollution*, 6(12):34–42.

Aoki, T. (2002). Photoluminescence spectroscopy. *Characterization of Materials*, pages 1–12.

Arbuznikov, A. (2007). Hybrid exchange correlation functionals and potentials: Concept elaboration. *Journal of Structural Chemistry*, 48:S1–S31.

Arumugam, M., Natarajan, T. S., Saelee, T., Praserthdam, S., Ashokkumar, M., and Praserthdam, P. (2021). Recent developments on bismuth oxyhalides (biox; x= cl, br, i) based ternary nanocomposite photocatalysts for environmental applications. *Chemosphere*, 282:131054.

Attri, P., Garg, P., Chauhan, M., Singh, R., Sharma, R. K., Kumar, S., Lim, D.-K., and Chaudhary, G. R. (2023). Metal doped biocl nano-architectures (m-biocl, m= ni, mo, cd, co) for efficient visible light photocatalytic and antibacterial behaviour. *Journal of Environmental Chemical Engineering*, 11(2):109498.

Baaloudj, O., Kenfoud, H., Badawi, A. K., Assadi, A. A., El Jery, A., Assadi, A. A., and Amrane, A. (2022). Bismuth sillenite crystals as recent photocatalysts for water treatment and energy generation: A critical review. *Catalysts*, 12(5):500.

Bai, L., Cao, Y., Pan, X., Shu, Y., Dong, G., Zhao, M., Zhang, Z., Wu, Y., and Wang, B. (2023). Z-scheme bi2s3/bi2o2co3 nanoheterojunction for the degradation of antibiotics

and organic compounds in wastewater: Fabrication, application, and mechanism. *Surfaces and Interfaces*, 36:102612.

Barhoumi, M. and Said, M. (2021). Electronic and optical properties of bismuth oxyhalides from ab initio calculations. *Materials Science and Engineering: B*, 264:114921.

Beal, A. and Liang, W. (1976). Reflectivity spectra of some first row transition metal intercalates of nbs2. *Philosophical Magazine*, 33(1):121–131.

Belousov, A. S., Parkhacheva, A. A., Suleimanov, E. V., Fukina, D. G., Koryagin, A. V., Shafiq, I., Krasheninnikova, O. V., and Kuzmichev, V. V. (2023). Doping vs. heterojunction: A comparative study of the approaches for improving the photocatalytic activity of flower-like bi2wo6 for water treatment with domestic led light. *Catalysis Communications*, page 106705.

Berthomieu, C. and Hienerwadel, R. (2009). Fourier transform infrared (ftir) spectroscopy. *Photosynthesis research*, 101:157–170.

Bhachu, D. S., Moniz, S. J., Sathasivam, S., Scanlon, D. O., Walsh, A., Bawaked, S. M., Mokhtar, M., Obaid, A. Y., Parkin, I. P., Tang, J., et al. (2016). Bismuth oxyhalides: synthesis, structure and photoelectrochemical activity. *Chemical Science*, 7(8):4832–4841.

Bhat, S. S. and Sundaram, N. G. (2015). Photocatalysis of bi 4 nbo 8 cl hierarchical nanostructure for degradation of dye under solar/uv irradiation. *New Journal of Chemistry*, 39(5):3956–3963.

Boutahir, O., Boutahir, M., Fakrach, B., Rahmani, A., Chadli, H., and Rahmani, A. (2020). Nonresonant raman spectroscopy analysis of bithiophene and quater-thiophene chains confined in graphene bilayer: A theoretical study. *Vibrational Spectroscopy*, 109:103064.

Cabrera, C., Contreras-Solorio, D., and Hernández, L. (2016). Joint density of states in low dimensional semiconductors. *Physica E: Low-dimensional Systems and Nanostructures*, 76:103–108.

Cao, Y., Malekshah, R. E., Heidari, Z., Pelalak, R., Marjani, A., and Shirazian, S. (2021). Molecular dynamic simulations and quantum chemical calculations of adsorption process using amino-functionalized silica. *Journal of Molecular Liquids*, 330:115544.

Carrasco, J., Barrio, L., Liu, P., Rodriguez, J. A., and Ganduglia-Pirovano, M. V. (2013). Theoretical studies of the adsorption of co and c on ni (111) and ni/ceo2 (111): evidence of a strong metal–support interaction. *The Journal of Physical Chemistry C*, 117(16):8241–8250.

Castillo-Cabrera, G. X., Espinoza-Montero, P. J., Alulema-Pullupaxi, P., Mora, J. R., and Villacís-García, M. H. (2022). Bismuth oxyhalide-based materials (biox: X= cl, br, i) and their application in photoelectrocatalytic degradation of organic pollutants in water: a review. *Frontiers in Chemistry*, 10:900622.

Chen, G., Chen, G., Wang, Y., Wang, Q., and Zhang, Z. (2015). Facile synthesis of n-doped biocl photocatalyst by an ethylenediamine-assisted hydrothermal method. *Journal of Nanomaterials*, 16(1):137–137.

Chen, P., Liu, H., Cui, W., Lee, S. C., Wang, L., and Dong, F. (2020). Bi-based photocatalysts for light-driven environmental and energy applications: structural tuning, reaction mechanisms, and challenges. *EcoMat*, 2(3):e12047.

Chen, Y., Zhou, Y., Zhang, J., Li, J., Yao, T., Chen, A., Xiang, M., Li, Q., Chen, Z., and Zhou, Y. (2022). Plasmonic bi promotes the construction of z-scheme heterojunction for efficient oxygen molecule activation. *Chemosphere*, 302:134527.

COby, R. (1993). The crystal structure of bioci. *Zeitschrift fur Kristallographie*, 205:35–40.

Demircioğlu, Z., Kaştaş, Ç. A., and Büyükgüngör, O. (2015). Theoretical analysis (nbo, npa, mulliken population method) and molecular orbital studies (hardness, chemical potential, electrophilicity and fukui function analysis) of (e)-2-((4-hydroxy-2-methylphenylimino) methyl)-3-methoxyphenol. *Journal of Molecular structure*, 1091:183–195.

Dutta, S., Das, T., and Datta, S. (2018). Impact of bi-axial strain on the structural, electronic and optical properties of photo-catalytic bulk bismuth oxyhalides. *Physical Chemistry Chemical Physics*, 20(1):103–111.

Dutta, V., Chauhan, A., Verma, R., Gopalkrishnan, C., and Nguyen, V.-H. (2022). Recent trends in bi-based nanomaterials: challenges, fabrication, enhancement techniques, and environmental applications. *Beilstein Journal of Nanotechnology*, 13(1):1316–1336.

Engel, E. (2011). *Density functional theory*. Springer.

Epstein, S. and Rosenthal, C. (1976). The hohenberg-kohn theorem. *Journal of Chemical Physics*, 64(1):247–249.

Feng, C., Liu, X., Zhu, T., and Tian, M. (2021). Catalytic oxidation of co on noble metal-based catalysts. *Environmental Science and Pollution Research*, 28(20):24847–24871.

Ferrer, M. M., Rodrigues, J. E. F., Almeida, M. A., Moura, F., Longo, E., Pizani, P. S., and Sambrano, J. R. (2018). Theoretical methods for calculations of optical phonons in biobr: Analysis and correction of propagated errors. *Journal of Raman Spectroscopy*, 49(8):1356–1363.

Foo, J. J., Tan, X.-Q., Ling, G. Z. S., Tan, L.-L., Chen, X., Ong, W.-J., et al. (2022). Evolutionary face-to-face 2d/2d bismuth-based heterojunction: The quest for sustainable photocatalytic applications. *Applied Materials Today*, 29:101636.

Garrity, K. F., Bennett, J. W., Rabe, K. M., and Vanderbilt, D. (2014). Pseudopotentials for high-throughput dft calculations. *Computational Materials Science*, 81:446–452.

Gianopoulos, C. G., Chua, Z., Zhurov, V. V., Seipp, C. A., Wang, X., Custelcean, R., and Pinkerton, A. A. (2019). Direct air capture of co2–topological analysis of the experimental electron density (qtaim) of the highly insoluble carbonate salt of a 2, 6-pyridine-bis (iminoguanidine),(pybigh2)(co3)(h2o) 4. *IUCrJ*, 6(1):56–65.

Gujar, T., Shinde, V., Lokhande, C., Mane, R., and Han, S.-H. (2005). Bismuth oxide thin films prepared by chemical bath deposition (cbd) method: annealing effect. *Applied surface science*, 250(1-4):161–167.

Hafner, B. (2007). Scanning electron microscopy primer. *Characterization Facility, University of Minnesota-Twin Cities*, pages 1–29.

Hammersley, J. (2013). *Monte carlo methods*. Springer Science & Business Media.

Han, X., Dong, S., Yu, C., Wang, Y., Yang, K., and Sun, J. (2016). Controllable synthesis of sn-doped biocl for efficient photocatalytic degradation of mixed-dye wastewater under natural sunlight irradiation. *Journal of Alloys and Compounds*, 685:997–1007.

Hazaraimi, M., Goh, P., Lau, W., Ismail, A., Wu, Z., Subramaniam, M., Lim, J., and Kanakaraju, D. (2022). The state-of-the-art development of photocatalysts for degrading of persistent herbicides in aqueous environment. *Science of the Total Environment*, page 156975.

Huang, H., Xiao, K., Zhang, T., Dong, F., and Zhang, Y. (2017). Rational design on 3d hierarchical bismuth oxyiodides via in situ self-template phase transformation and phase-junction construction for optimizing photocatalysis against diverse contaminants. *Applied Catalysis B: Environmental*, 203:879–888.

Huang, J., Liu, T., Wang, R., Zhang, M., Wang, L., She, H., and Wang, Q. (2020). Facile loading of cobalt oxide on bismuth vanadate: Proved construction of pn junction for efficient photoelectrochemical water oxidation. *Journal of colloid and interface science*, 570:89–98.

Huang, W. L. and Zhu, Q. (2008). Electronic structures of relaxed biox (x= f, cl, br, i) photocatalysts. *Computational Materials Science*, 43(4):1101–1108.

Huizhong, A., Yi, D., Tianmin, W., Cong, W., Weichang, H., and ZHANG, J. (2008). Photocatalytic properties of biox (x= cl, br, and i). *Rare Metals*, 27(3):243–250.

Islam, T., Repon, M. R., Islam, T., Sarwar, Z., and Rahman, M. M. (2023). Impact of textile dyes on health and ecosystem: A review of structure, causes, and potential solutions. *Environmental Science and Pollution Research*, 30(4):9207–9242.

Jessen, P. and Deutsch, I. (1996). Optical lattices. *Advances in Atomic, Molecular, and Optical Physics*, 37:95–138.

Ji, G.-J., Xiang, T., Zhou, X.-Q., Chen, L., Zhang, Z.-H., Lu, B.-B., and Zhou, X.-J. (2022). Molecular dynamics simulation of adsorption and separation of xylene isomers by cu-hkust-1. *RSC advances*, 12(54):35290–35299.

Jia, T., Wu, J., Xiao, Y., Liu, Q., Wu, Q., Qi, Y., and Qi, X. (2021). Self-grown oxygen vacancies-rich ceo2/biobr z-scheme heterojunction decorated with rgo as charge transfer channel for enhanced photocatalytic oxidation of elemental mercury. *Journal of Colloid and Interface Science*, 587:402–416.

Jupp, A. R., Johnstone, T. C., and Stephan, D. W. (2018). The global electrophilicity index as a metric for lewis acidity. *Dalton Transactions*, 47(20):7029–7035.

Khattab, T. A., Abdelrahman, M. S., and Rehan, M. (2020). Textile dyeing industry: environmental impacts and remediation. *Environmental Science and Pollution Research*, 27(4):3803–3818.

Khnifiraa, M., El Hamidia, S., Machrouhia, A., Mahsounea, A., Boumyaa, W., Tounsadia, H., Mahjoubia, F. Z., Sadiqa, M., Barkaa, N., and Abdennouria, M. (2020). Theoretical and experimental study of the adsorption characteristics of methylene blue on titanium dioxide surface using dft and monte carlo dynamic simulation. *Homo*, 2(2).

Kohn, W. and Sham, L. (1996). Density functional theory. In *Conference Proceedings-Italian Physical Society*, volume 49, pages 561–572. Editrice Compositori.

Kratzer, P. and Neugebauer, J. (2019). The basics of electronic structure theory for periodic systems. *Frontiers in chemistry*, 7:106.

Kumar, A. and Pandey, G. (2017). A review on the factors affecting the photocatalytic degradation of hazardous materials. *Mater. Sci. Eng. Int. J*, 1(3):1–10.

Kumar, S., Parashari, S. S., and Auluck, S. (2009). Disorder effects on electronic and optical properties of the ternary gaxin1- xp (x= 0.25, 0.50, and 0.75) alloy. *physica status solidi (b)*, 246(10):2294–2300.

Lee, G.-J., Zheng, Y.-C., and Wu, J. J. (2018). Fabrication of hierarchical bismuth oxyhalides (biox, x= cl, br, i) materials and application of photocatalytic hydrogen production from water splitting. *Catalysis Today*, 307:197–204.

Lewin, M., Lieb, E. H., and Seiringer, R. (2019). The local density approximation in density functional theory. *Pure and Applied Analysis*, 2(1):35–73.

Li, B., Lai, C., Zeng, G., Qin, L., Yi, H., Huang, D., Zhou, C., Liu, X., Cheng, M., Xu, P., et al. (2018). Facile hydrothermal synthesis of z-scheme bi2fe4o9/bi2wo6 heterojunction photocatalyst with enhanced visible light photocatalytic activity. *ACS applied materials & interfaces*, 10(22):18824–18836.

Li, H., Jian, L., Chen, Y., Wang, G., Lyu, J., Dong, X., Liu, X., and Ma, H. (2022). Fabricating bi2moo6@ co3o4 core–shell heterogeneous architectures with z-scheme for superior photoelectrocatalytic water purification. *Chemical Engineering Journal*, 427:131716.

Li, J., Yu, Y., and Zhang, L. (2014). Bismuth oxyhalide nanomaterials: layered structures meet photocatalysis. *Nanoscale*, 6(15):8473–8488.

Li, J., Yuan, H., and Zhu, Z. (2015a). Fabrication of cu2o/au/bipo4 z-scheme photocatalyst to improve the photocatalytic activity under solar light. *Journal of Molecular Catalysis A: Chemical*, 410:133–139.

Li, W. T., Huang, W. Z., Zhou, H., Yin, H. Y., Zheng, Y. F., and Song, X. C. (2015b). Synthesis of zn2+ doped biocl hierarchical nanostructures and their exceptional visible light photocatalytic properties. *Journal of Alloys and Compounds*, 638:148–154.

Liang, M., Yang, Z., Yang, Y., Mei, Y., Zhou, H., and Yang, S. (2019). One-step introduction of metallic bi and non-metallic c in bi 2 wo 6 with enhanced photocatalytic activity. *Journal of Materials Science: Materials in Electronics*, 30:1310–1321.

Liao, L., Liu, J., Wang, T., Xu, F., Sun, L., Zhou, T., Wu, J., Guan, Y., Luo, Y., Zou, Y., et al. (2022). Improved hydrogen generation of al-h2o reaction by biox (x= halogen) and influence rule. *Materials*, 15(22):8199.

Liu, L., Zhong, S., Zhang, L., Liu, B., and Wang, W. (2022a). Ti doped biocl nanowires for piezoelectric photocatalytic degradation of organic pollutants. *Catalysis Communications*, 170:106493.

Liu, L., Zhong, S., Zhang, L., Liu, B., and Wang, W. (2022b). Ti doped biocl nanowires for piezoelectric photocatalytic degradation of organic pollutants. *Catalysis Communications*, 170:106493.

Liu, W.-W. and Peng, R.-F. (2020). Recent advances of bismuth oxychloride photocatalytic material: Property, preparation and performance enhancement. *Journal of Electronic Science and Technology*, 18(2):100020.

Long, Z., Wang, H., Huang, K., Zhang, G., and Xie, H. (2022). Di-functional cu2+-doped biocl photocatalyst for degradation of organic pollutant and inhibition of cyanobacterial growth. *Journal of Hazardous Materials*, 424:127554.

Meena, M., Sonigra, P., and Yadav, G. (2021). Biological-based methods for the removal of volatile organic compounds (vocs) and heavy metals. *Environmental Science and Pollution Research*, 28:2485–2508.

Meng, X. and Zhang, Z. (2016). Bismuth-based photocatalytic semiconductors: introduction, challenges and possible approaches. *Journal of Molecular Catalysis A: Chemical*, 423:533–549.

Mokhtari, F. and Tahmasebi, N. (2021). Hydrothermal synthesis of w-doped biocl nanoplates for photocatalytic degradation of rhodamine b under visible light. *Journal of Physics and Chemistry of Solids*, 149:109804.

Mora-Hernandez, J. M., Herrera, L. A. A., Garay-Rodriguez, L. F., Torres-Martínez, L. M., and Hernandez-Perez, I. (2023). An enhanced photo (electro) catalytic co2 reduction onto advanced biox (x= cl, br, i) semiconductors and the bioi–pdcu composite. *Heliyon*, 9(10).

Mubeen, K., Irshad, A., Safeen, A., Aziz, U., Safeen, K., Ghani, T., Khan, K., Ali, Z., ul Haq, I., and Shah, A. (2023). Band structure tuning of zno/cuo composites for enhanced photocatalytic activity. *Journal of Saudi Chemical Society*, 27(3):101639.

Mulliken, R. S. (1955). Electronic population analysis on lcao–mo molecular wave functions. i. *The Journal of chemical physics*, 23(10):1833–1840.

Ngambia, A., Ifthikar, J., Shahib, I. I., Jawad, A., Shahzad, A., Zhao, M., Wang, J., Chen, Z., and Chen, Z. (2019). Adsorptive purification of heavy metal contaminated wastewater with sewage sludge derived carbon-supported mg (ii) composite. *Science of the Total Environment*, 691:306–321.

Nussbaum, M., Shaham-Waldmann, N., and Paz, Y. (2014a). Synergistic photocatalytic effect in fe, nb-doped biocl. *Journal of Photochemistry and Photobiology A: Chemistry*, 290:11–21.

Nussbaum, M., Shaham-Waldmann, N., and Paz, Y. (2014b). Synergistic photocatalytic effect in fe, nb-doped biocl. *Journal of Photochemistry and Photobiology A: Chemistry*, 290:11–21.

Okoye, C. (2004). Structural, electronic, and optical properties of beryllium monochalcogenides. *The European Physical Journal B-Condensed Matter and Complex Systems*, 39(1):5–17.

Pembere, A. M., Yang, M., and Luo, Z. (2017). Small gold clusters catalyzing the conversion of glycerol to epichlorohydrin. *Physical Chemistry Chemical Physics*, 19(38):25840–25845.

Perdew, J. P. (1991). Generalized gradient approximations for exchange and correlation: A look backward and forward. *Physica B: Condensed Matter*, 172(1-2):1–6.

Puttaraju, T., Shashank, M., Naika, H. R., Nagaraju, G., and Manjunatha, M. (2022). Synthesis of bismuth oxychloride nanoparticles via co-precipitation method: Evaluation of photocatalytic activity. *Materials Today: Proceedings*, 62:5533–5539.

Qian, X., Yue, D., Tian, Z., Reng, M., Zhu, Y., Kan, M., Zhang, T., and Zhao, Y. (2016). Carbon quantum dots decorated bi2wo6 nanocomposite with enhanced photocatalytic oxidation activity for vocs. *Applied Catalysis B: Environmental*, 193:16–21.

Rauf, M. and Hisaindee, S. (2013). Studies on solvatochromic behavior of dyes using spectral techniques. *Journal of Molecular Structure*, 1042:45–56.

Ren, X., Gao, M., Zhang, Y., Zhang, Z., Cao, X., Wang, B., and Wang, X. (2020). Photocatalytic reduction of co2 on biox: Effect of halogen element type and surface oxygen vacancy mediated mechanism. *Applied Catalysis B: Environmental*, 274:119063.

Sajjad, M., Singh, N., and Larsson, J. A. (2020). Bulk and monolayer bismuth oxyiodide (bioi): Excellent high temperature p-type thermoelectric materials. *AIP Advances*, 10(7).

Salami, N. and Shokri, A. (2021). Electronic structure of solids and molecules. In *Interface science and technology*, volume 32, pages 325–373. Elsevier.

Sayed, M., Yu, J., Liu, G., and Jaroniec, M. (2022). Non-noble plasmonic metal-based photocatalysts. *Chemical Reviews*, 122(11):10484–10537.

Setyawan, W. and Curtarolo, S. (2010). High-throughput electronic band structure calculations: Challenges and tools. *Computational materials science*, 49(2):299–312.

Shi, H., Wei, X., Zhang, J., Long, Q., Liu, W., Zhou, Y., and Ding, Y. (2020). Green synthesis and direct z-scheme cdse/biocl heterojunctions for enhanced photocatalytic performance. *ChemistrySelect*, 5(20):6230–6235.

Song, S., Xing, Z., Zhao, H., Li, Z., and Zhou, W. (2022). Recent advances in bismuth-based photocatalysts: Environment and energy applications. *Green Energy & Environment*.

Stanjek, H. and Häusler, W. (2004). Basics of x-ray diffraction. *Hyperfine interactions*, 154:107–119.

Thakur, A. and Kumar, A. (2022). Recent advances on rapid detection and remediation of environmental pollutants utilizing nanomaterials-based (bio) sensors. *Science of The Total Environment*, 834:155219.

Tharuman, S., Balakumar, V., Vinodhini, J., Karthikeyani, R., Mayandi, J., Sasirekha, V., and Pearce, J. (2023). Visible light driven photocatalytic performance of 3d tio2/g-c3n5 nanocomposite via z-scheme charge transfer promotion for water purification. *Journal of Molecular Liquids*, 371:121101.

Wakjira, T. L., Gemta, A. B., Kassahun, G. B., Andoshe, D. M., and Tadele, K. (2024). Bismuth-based z-scheme heterojunction photocatalysts for remediation of contaminated water. *ACS omega*.

Wang, Q., Chen, K., Wang, S., Jiang, D., Ma, C., Zhu, L., and Xu, X. (2023). An in situ-fabricated p-co 3 o 4@ n-zno surface heterojunction photocatalyst for solar-to-fuel conversion of co 2. *Materials Chemistry Frontiers*.

Wang, R., Li, H., and Sun, H. (2019). Bismuth: environmental pollution and health effects. *Encyclopedia of environmental health*, page 415.

Wang, S., Wang, L., and Huang, W. (2020). Bismuth-based photocatalysts for solar energy conversion. *Journal of materials chemistry A*, 8(46):24307–24352.

Wang, Y., Shi, Z., Fan, C., Wang, X., Hao, X., and Chi, Y. (2013). Synthesis, characterization, and photocatalytic properties of biobr catalyst. *Journal of Solid State Chemistry*, 199:224–229.

Wei, J., Chen, Z., and Tong, Z. (2021). Engineering z-scheme silver oxide/bismuth tungstate heterostructure incorporated reduced graphene oxide with superior visible-light photocatalytic activity. *Journal of Colloid and Interface Science*, 596:22–33.

Wu, L., Yue, X., Chang, Y., Wang, K., Zhang, J., Sun, J., Wei, Z., and Kowalska, E. (2022). Photocatalytic degradation of tetracycline under visible light irradiation on bivo4 microballs modified with noble metals. *Catalysts*, 12(11):1293.

Wu, S. and Wu, D. (2016). First principle calculations of photocatalytic properties of bismuth oxyhalides considering van der waals correction. In *2016 IEEE International Conference on Electro Information Technology (EIT)*, pages 0452–0457. IEEE.

Xie, F., Mao, X., Fan, C., and Wang, Y. (2014). Facile preparation of sn-doped biocl photocatalyst with enhanced photocatalytic activity for benzoic acid and rhodamine b degradation. *Materials science in semiconductor processing*, 27:380–389.

Xie, T., Sun, S., Guo, Y., Luo, Y., Yang, M., Yang, B., and Cui, J. (2023a). Fabrication of in–s-co-doped two-dimensional biocl coupling with surface hydroxylation toward simultaneously efficient charge separation and redox capability for photocatalytic water remediation. *Chemosphere*, 315:137742.

Xie, Z., Wang, W., Ke, X., Cai, X., Chen, X., Wang, S., Lin, W., and Wang, X. (2023b). A heptazine-based polymer photocatalyst with donor-acceptor configuration to promote exciton dissociation and charge separation. *Applied Catalysis B: Environmental*, 325:122312.

Yang, B., He, L., Guo, Y., Zhao, T., Shi, Z., Liu, C., Yang, M., Yang, Q., Sun, S., and Cui, J. (2023a). Enhanced catalysis for degradation of antibiotic by hydroxyl-functionalized s-doped biocl with high capacity of local spatial charge separation. *Colloids and Surfaces A: Physicochemical and Engineering Aspects*, 669:131448.

Yang, Y., Zheng, X., Song, Y., Liu, Y., Wu, D., Li, J., Liu, W., Fu, L., Shen, Y., and Tian, X. (2023b). Cuins2-based photocatalysts for photocatalytic hydrogen evolution via water splitting. *International Journal of Hydrogen Energy*, 48(10):3791–3806.

Yao, L., Yang, H., Chen, Z., Qiu, M., Hu, B., and Wang, X. (2021). Bismuth oxychloride-based materials for the removal of organic pollutants in wastewater. *Chemosphere*, 273:128576.

Yi, J., Zeng, H., Lin, H., Li, M., Xie, R., Chen, B., Ding, R., Liu, Z., Li, D., and Li, N. (2023). Fabrication of direct z-scheme ag2o/bi2moo6 heterostructured microsphere with enhanced visible-light photocatalytic activity. *Journal of Alloys and Compounds*, 935:168151.

Yu, W., Jin, C., and Kohlmeyer, A. (2007). First principles calculation of phonon dispersion, thermodynamic properties and b 1-to-b 2 phase transition of lighter alkali hydrides. *Journal of Physics: Condensed Matter*, 19(8):086209.

Zahraei, M. S. N., Fazaeli, R., Aliyan, H., and Richeson, D. (2023). Photocatalytic degradation abilities of binary core-shell sio2@ mzro2/tio2 nanocomposites: Characterization, kinetic and thermodynamic study of metoclopramide (mcp) eradication for water purification. *Materials Research Bulletin*, 157:112029.

Zhang, K.-L., Liu, C.-M., Huang, F.-Q., Zheng, C., and Wang, W.-D. (2006). Study of the electronic structure and photocatalytic activity of the biocl photocatalyst. *Applied Catalysis B: Environmental*, 68(3-4):125–129.

Zhang, L., Tang, Z.-K., Lau, W.-M., Yin, W.-J., Hu, S.-X., and Liu, L.-M. (2017). Tuning band gaps and optical absorption of biocl through doping and strain: insight form dft calculations. *Physical Chemistry Chemical Physics*, 19(31):20968–20973.

Zhang, Q., Nie, W., Hou, T., Shen, H., Li, Q., Guan, C., Duan, L., and Zhao, X. (2022). Optical and photocatalytic properties of br-doped biocl nanosheets with rich oxygen vacancies and dominating {001} facets. *Nanomaterials*, 12(14):2423.

Zhang, W., Zhang, Q., and Dong, F. (2013). Visible-light photocatalytic removal of no in air over biox (x= cl, br, i) single-crystal nanoplates prepared at room temperature. *Industrial & Engineering Chemistry Research*, 52(20):6740–6746.

Zhang, Y.-J., Cheng, J.-Z., Xing, Y.-Q., Tan, Z.-R., Liao, G., and Liu, S.-Y. (2023). Solvent-exfoliated da π-polymer@ zns heterojunction for efficient photocatalytic hydrogen evolution. *Materials Science in Semiconductor Processing*, 161:107463.

Zhang, Z., Pan, Z., Guo, Y., Wong, P. K., Zhou, X., and Bai, R. (2020). In-situ growth of all-solid z-scheme heterojunction photocatalyst of bi7o9i3/g-c3n4 and high efficient degradation of antibiotic under visible light. *Applied Catalysis B: Environmental*, 261:118212.

Zhao, B., Shao, N., Chen, X., Ma, J., Gao, Y., and Chen, X. (2023). Construction of novel type ii heterojunction wo3/bi2wo6 and z-scheme heterojunction cds/bi2wo6 photocatalysts with significantly enhanced photocatalytic activity for the degradation of rhodamine b and reduction of cr (vi). *Colloids and Surfaces A: Physicochemical and Engineering Aspects*, 663:131072.

Zhao, L., Zhang, X., Fan, C., Liang, Z., and Han, P. (2012). First-principles study on the structural, electronic and optical properties of biox (x= cl, br, i) crystals. *Physica B: Condensed Matter*, 407(17):3364–3370.

Zheng, X., Song, Y., Liu, Y., Yang, Y., Wu, D., Yang, Y., Feng, S., Li, J., Liu, W., Shen, Y., et al. (2023). Znin2s4-based photocatalysts for photocatalytic hydrogen evolution via water splitting. *Coordination Chemistry Reviews*, 475:214898.

Zhou, S., Shi, T., Chen, Z., Kilin, D. S., Shui, L., Jin, M., Yi, Z., Yuan, M., Li, N., Yang, X., et al. (2019). First-principles study of optoelectronic properties of the noble metal (ag and pd) doped biox (x= f, cl, br, and i) photocatalytic system. *Catalysts*, 9(2):198.

Zhou, Y., Cheng, B., Huang, S., Huang, X., Jiang, R., Wang, X., Zhang, W., Jia, B., Lu, P., and Song, H.-Z. (2023). The tunable electronic and optical properties of two-dimensional bismuth oxyhalides. *Nanomaterials*, 13(20):2798.

Zulkiflee, A., Khan, M. M., and Harunsani, M. H. (2023a). Bismuth oxyhalides: recent progress and its applications in photocatalysis, hydrogen production, antibacterial studies, and sensors. *Materials Science in Semiconductor Processing*, 163:107547.

Zulkiflee, A., Khan, M. M., Khan, A., Khan, M. Y., Dafalla, H. D. M., and Harunsani, M. H. (2023b). Sn-doped biocl for photoelectrochemical activities and photocatalytic dye degradation under visible light. *Heliyon*.

Zulkiflee, A., Khan, M. M., Khan, M. Y., Khan, A., Ummer, A. C., and Harunsani, M. H. (2023c). Zirconium-doped biocl for enhanced visible light-induced photocatalytic degradation of rhb dye and photoelectrochemical studies. *New Journal of Chemistry*, 47(35):16577–16585.

Zuo, J. M. and Spence, J. C. (2017). *Advanced transmission electron microscopy*. Springer.